POLITECNICO DI MILANO
Corso di Laurea Specialistica in Ingegneria Biomedica

Fluid dynamics and structural computational analysis of the aortic arch in the precence of bicuspid aortic valve

Relatori:
Prof. Francesco Migliavacca
Prof. Felipe Gabaldon

Tesi di Laurea Specialistica di:
Andrea Cani
Matricola 725064

Anno Accademico 2009-2010

POLITECNICO DI MILANO
Corso di Laurea Specialistica in Ingegneria Biomedica

Fluid dynamics and structural computational analysis of the aortic arch in the precence of bicuspid aortic valve

Relatori:
Prof. Francesco Migliavacca
Prof. Felipe Gabaldon

Tesi di Laurea Specialistica di:
Andrea Cani
Matricola 725064

Anno Accademico 2009-2010

Forse oggi l'obiettivo principale
non è di scoprire che cosa siamo,
ma piuttosto di rifiutare quello che siamo.
Dobbiamo immaginare e costruire
ciò che potremmo diventare.

M. Foucault

Sommario

La bicuspidia dell'aorta (BAV) è l'anomalia congenita più frequente del sistema cardiocircolatorio. La valvola aortica bicuspide può portare allo sviluppo prematuro di rilevanti malattie della valvola, come stenosi o insufficienza e endocarditi. Anomalie dell'aorta, come dilatazione aortica, aneurisma e dissezione, sono state rilevate in presenza di BAV in molti pazienti. L'influenza di questa patologia sullo sviluppo di aneurisma dell'aorta ascendente può essere spiegata attraverso la teoria cosiddetta "genetica" o con la teoria "emodinamica". Allo scopo di investigare il ruolo della distribuzione dello sforzo di taglio in aorta ascendente e degli sforzi meccanici sulla parete aortica, sono stati utilizzati in questo lavoro di tesi strumenti computazionali di fluido dinamica e di meccanica delle strutture. Sono stati sviluppati e implementati un modello fisiologico e un modello BAV dell'arco aortico implementando l'interazione fluido struttura (FSI) (sangue - parete aortica), e prendendo in considerazione l'alterata distribuzione di velocità a valle della valvola bicuspide. Comparando i risultati durante il ciclo cardiaco, gli sforzi meccanici della parete aortica dei due modelli non hanno mostrato significative differenze, mentre gli sforzi di taglio alla parete aortica (WSS) per il modello BAV presentano valori sensibilmente superiori. In particolare, durante il picco sistolico la differenza puo raggiungere il 70% proprio dove l'aorta ascendente è clinicamente più soggetta allo sviluppo di aneurisma. Questo studio computazionale sembra quindi confermare l'ipotesi che il WSS possa giocare un ruolo fondamentale nell'attivazione dei meccanismi di meccano-trasduzione che portano all'insorgenza di aneurisma in presenza di BAV.

Abstract

Bicuspid aortic valve (BAV) disease is the most frequent congenital anomaly of the heart or great vessels. Congenital BAV may lead to premature development of significant aortic valve diseases, such as aortic valve stenosis or regurgitation and endocarditis. Abnormalities of the aorta, such as aortic dilatation, aneurysm and dissection, have also been described in association with BAV. The influence of the BAV's presence on the aneurysm development can be explained by means of either the "genetic" or the "hemodynamic" theory. In order to investigate the role of the shear stress distribution on the ascending aorta and the mechanical stresses on the aortic arch wall, fluid dynamics and structural computational tools are used. A physiological model and a BAV model of the aortic arch have been developed using a fluid-structure coupling and taking into account the velocity distribution conditions downstream of the different valve morphology. Comparing the results in a cardiac cycle, mechanical stresses on the ascending aortic wall don't show significant differences, while the wall shear stresses (WSS) computed for the BAV's model appears to be increased. Particularly during the systolic peak the difference is more than 70% where the ascending aorta is more subjected to the development of aneurysm. This computational study seems to confirm the hypothesis that the WSS may play the main role in the mechanotransduction pathways leading to aneurysm in presence of BAV.

Contents

List of Figures

List of Tables

Chapter 1

Introduction

Congenital bicuspid aortic valve, the most frequent cardiac malformation (1-2% of all live birth) is known to be a predisposing factor for development of ascending aortic dilative disease. An ascending dilatation or aneurysm has been found in as much as 50-70% of adult patients with a bicuspid aortic valve (BAV) [6]. Despite this relevant epidemiology, the pathogenesis of aortic dilatation associated to BAV has still to be elucidated.
Two opposite theories have been proposed: a "genetic" theory, attributing both valve malformation and aortic intrinsic weakness to a common inherited developmental defect, and a "hemodynamic" theory, attributing a central role to flow derangements caused by valve dysfunction (post-stenotic mechanism). A precise mechanisms of inheritability has not been discovered, nor an underlying genetic defect has been detected, and the genetic theory seems to be limited by the evidence of BAV subjects not developing aortic dilation. On the other side, the hemodynamic theory is contrasted by the evidence of aortic dilatations in BAV subjects without stenosis or with a mild degree stenosis. To clarify pathogenetic aspects of this matter could prelude to the development of preventive or therapeutic strategies.
In the chapter 2 the clinical aspect of the BAV disease and the possible correlation with the aneurysm of the ascending aorta is discussed.

During the last decade the use of numerical techniques, aimed at analysing and understanding the biomechanics of the aortic root, has been increasing. These techniques, in their various versions, allow to

simulate the structural behaviour of the aortic wall and of the valvular leaflets (computational structural dynamics - CSD), or the hemodynamics within the studied domain (computational fluid-dynamics-CFD).
A single study, by Robicsek and colleagues [45], has been so far published aiming to reconstruct in mathematical models the rheological and biomechanical anomalies occurring with BAV. Robicsek showed that, due to the eccentricity of valve opening, with excessive folding and wrinkling of the cusp margins, flow is highly irregular, even without clinically evident valve stenosis. In particular, the vortices (eddy currents) that normally form in the aortic root and maintain the leaflets suspended in the systolic flow minimizing their stresses, were observed beyond the sino-tubular junction in BAV (ascending aorta proper), instead of being confined within the sinuses of Valsalva like in the trileaflet valve. Turbulences were directed toward the right and anteriorly, and wall stress was also found to be abnormally increased in the right anterior-lateral aspect of the ascending aortic wall. Whether this pattern could be applied also in the real setting of BAV patients and could be related to the development of aortic dilative disease is an appealing hypothesis to test.

The aim of this work is to compare the physiological and the pathological condition in terms of flow patterns and stresses of the aortic wall using computational tools, in order to investigate the "hemodynamic" theory grounding.
Two models have been developed and analyzed including a fluid domain (representing the blood) and a solid domain (representing the aortic wall). Particularly, the wall shear stress distributions in the aortic arch during the cardiac cycle and the stresses of the arterial wall are investigate and compared.

In chapter 3, after a brief discussion of the main equations of the continuum mechanics, several constitutive models for the aortic wall are presented; among these the hyperelastic model of Demiray is selected and implemented in order to simulate the aortic behavior.

In chapter 4 the assumption for the blood's rheology and the main fluid dynamic equations are declared and discussed. The blood will be

modeled as an incompressible and newtonian fluid and the flow inside the aortic region as laminar.

An important issue of this work is the coupling between the fluid and the solid domain. In the chapter 5 the mathematical and computational aspects of the FSI (fluid-structure interaction) are discussed. The fluid-structure coupling using *ABAQUS* 6.8 and *Star CD* 4.1 has been done in order to achieve the proposed goals.

The methods used (including boundary conditions, initial conditions etc.) and the results of the simulations are showed in chapter 6 comparing the models developed.

In last chapter some conclusions are described and the critical aspects of the models and the possible improvements are discussed.

Chapter 2

Clinical background

In industrialized countries the most common cardiovascular disease after hypertension and atherosclerosis is degenerative aortic valve disease, and aortic valve procedures are at the second place among the most frequent cardiac surgery operations, following coronary bypass grafting. In a recent series, over half of the patients referred for surgery for isolated aortic valve stenosis were noted to have a congenital bicuspid aortic valve (BAV). It is well-known that BAV, the most frequent cardiac malformation (1-2% of live-births), is a predisposing factor to dilative disease of the ascending aorta [36] . An ascending dilatation or aneurysm has been encountered in as much as 50-70% of adult subject with a BAV. The risk of aortic dissection is 5 to 9-fold increased with BAV when compared to the general population. Therefore, in the clinical practice it is not uncommon to encounter, often in young patients, the association of a BAV, with or without severe valve dysfunction, with a varying degree of ascending aorta enlargement. This situation constitutes still today a surgical dilemma, with regard both to surgical timing and to the surgical technique to employ. Surgical concerns are strictly related to the lack of a pathogenetic explanation for this association.

2.1 The BAV and the aneurysm

Two are the main pathogenetic theories. The "genetic" theory is suggested by the similarity of the histological lesions (i.e. medial degeneration features) of BAV- and Marfan-associated aortic dilatations and by

their development in young age: it alleges that a genetically determined defect of embryonic development may affect those neural crest cells that concur in the formation of both the venrtriculo-arterial valves and the aorta and pulmonary artery. Errors in this embryogenetic mechanism could lead to both valve malformation and the tendency of the aortic wall to degenerate. A familial clustering of BAV has been demonstrated, although the inheritance mechanism has never been elucidated and the genetic defect implied has never been disclosed.

The "hemodynamic" theory attributes the tendency toward aortic enlargement to the increased mechanical stimulation on the aortic wall related to the abnormal flow downstream from the malformed valve. It is known that both in physiological conditions, such as during vascular system fetal maturation, and in diseases, flow conditions can influence the vascular wall function and microstructure. The hemodynamic theory would also explain the differences between Marfan's Syndrome and BAV in terms of age of aortic complication onset (relatively older in BAV) and in terms of systemic involvement (lacking in BAV). However, the controversy remains, above all for the evidence of aortic dilatations occurring also in patients with a normally functioning or only mildly stenotic BAV: in those cases the "post-stenotic" mechanism would seem less tenable. In particular Keane and colleagues [26] matching BAV and tricuspid aortic valve patients for degree of aortic valve dysfunction, found that aortic diameters were greater in BAV, beyond that predicted by the degree of hemodynamic disturbance. The Authors therefore supported the genetic theory. However, another recent echocardiography study showed that the phenomenon of post-stenotic dilation is frequent (about 1/4 of all aortic valve stenosis patients), but, since a direct correlation between degree of stenosis and aortic diameter could be found, it appeared to be an early adaptive reaction to stroke volume reduction, not progressing parallel to stenosis worsening.

Another unresolved question related to the pathogenetic debate is why not all BAV subjects experience aortic complications and therefore what could distinguish BAV patients with ascending dilation to those without it. Some factors are known to condition the progression towards

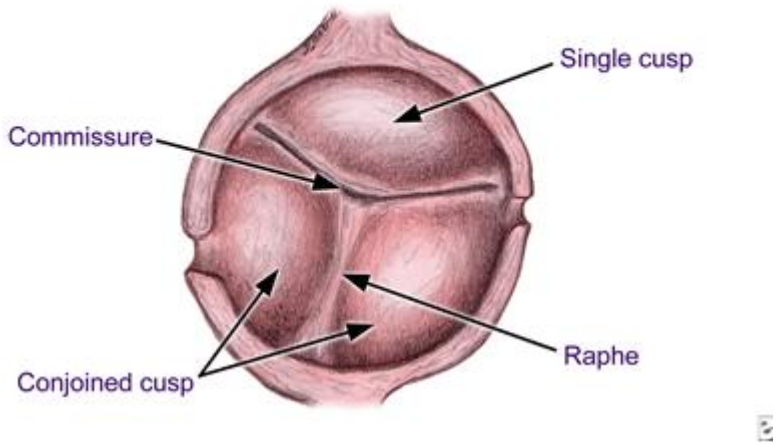

Figure 2.1: BAV anatomy

valve dysfunction: for example dislipidaemia, smoke and interestingly valve gross morphology can influence the rapidity of stenosis development. Stenosis progresses more rapidly if the cusps are asymmetrical in surface area and in antero-posterior position (raphe between non-coronary and right coronary cusps). However, the most common cusp fusion pattern is the left-right coronary one (figure 2.1). It is not possible today to predict the risk of aortic dilatation/aneurysm in the individual patient with BAV. This makes a strict echocardiography follow-up mandatory in BAV patients even without aortic stenosis.

New imaging techniques, such as three-dimensional phase-contrast cine-magnetic resonance, have been already demonstrated to have the potential for providing precise and quantifiable data on flow patterns in the ascending aorta of the individual patient. Nevertheless, they have not been applied to the study of BAV yet. Such techniques also allow for a brilliant alternative to mathematical simulations of flow (through CFD) in providing, by means of the lagrangian analysis of the trajectory of virtual particles, hemodynamic data to be used for quantification of biomechanical forces acting on the vascular wall in computer models, with remarkable cost and artifact reduction. Histology picture of ascending aorta dilation in BAV disease is represented by medial degeneration (formerly known as cystic medial necrosis). This is not a specific fea-

ture of this condition, since it underlies also senile dilation of ascending aorta (and it is in fact considered as the physiological substrate of medial ageing) and non-inflammatory aortic root disease, a term encompassing syndromic forms (Marfan's Syndrome, with fibrillin-1 congenital defect, Ehler-Danlos' Syndrome, with tenasscin-X defect and so on), idiopathic sporadic forms or those associated with aortic valve disease (post-stenotic dilation). In spite of the common histological picture, it is believed that the different forms could be characterized by different microstructural and molecular changes.

In particular extracellular matrix (ECM) proteins and proteases have a lead role in the processes of vessel wall remodeling that continuously occur also in the physiological setting, modulating the biomechanical properties of the wall and thereby allowing for its correct functioning. Alterations in those processes may cause the early "wearing out" of the arterial wall and consequent dilatation. The data raised by several Authors that have recently focused their attention on the morphological and microstructural facets of this disease have been often inconsistent and not comparable with one other. Bondermann and colleagues observed an increase in smooth muscle cells apoptotic index in fragments of aortic wall from patients with BAV without aortic dilatation, compared to the aortic wall from trileaflet aortic valve patients [35].
Among patients with aortic dilation there were no differences in apoptosis between BAV and non-BAV instead. This seemed to suggest that apoptosis could be an early event in the development of BAV associated dilation but non in the setting of a tricuspid valve. In a concurrent morphometry study from the Toronto research group, however, no differences were observed in terms of number of cells between BAV and non-BAV patients, but they differed only in terms of elastic fibres fragmentation [39].

An attempt to go deeper in this investigations have come from Fedak and colleagues, who evaluated through immunohistochemistry the content of fibrillin the aortic media of BAV and non-BAV patients and through zymography the amount and activity of matrix metalloprotease-2 (MMP-2, degrading elastin and other medial matrix proteins). Briefly,

their results suggested a reduction in fibrillin amount with BAV and a significant increase in MMP-2 active form, when compared to aortas with tricuspid aortic valve. Unfortunately, in that study the two groups in comparison were heterogeneous, being half of the aortas in the BAV groups dilated versus only 1 out of 11 aortas in the tricuspid group, and this could have heavily affected the observed results. Each published morphostructural study have so far left unresolved the question of the mechanisms of development of cell and ECM changes.

The phenomena of vascular tissue remodeling are currently considered to be involved in clinically important processes, such as atherogenesis, restenosis after balloon angioplasty and aneurysm development.
A key role seems to be played in all those situations by medial smooth muscle cell (SMC) change from the basal contractile phenotype to a synthetic one. Bunton et al., in a mouse model of Marfan's syndrome, found that the loss of SMC attachment to the elastic laminae, normally mediated by fibrillin-rich microfibrils, induces SMC conversion to synthetic phenotype and over-production of ECM components and of proteolytic enzymes, including matrix metallo-proteinases, responsible for subsequent massive elastolysis and collagenolysis.
However, vascular SMC activation and matrix degradation have been found to be triggered not only by congenital defects in cell-matrix attachment, but also by acquired conditions, and especially by mechanical stimuli, such as increased transmural pressure and cyclical strain (periodic deformation due to the pulsatile nature of flow) alterations. Some ECM proteins like fibronectin, tenascin, laminin and collagen IV, being constituents of the basal lamina, thin layer of matrix surrounding cells and connecting them to the elastic lamellae, play an important role in the continuous signal exchange between SMCs and ECM, affecting cell functional state.
Cell adhesion to the physiologic substrate maintains the differentiated state in the adult, preserves cell integrity and represses pro-apoptotic signals, while cell detachment from the matrix has opposed effects, among whom the anoikis, i.e. cell death mediated by cell-matrix interaction changes.

Chapter 3

Computational models of the arterial wall

The constitutive models presented in this chapter have been developed in order to describe the macroscopic behavior of different kind of biological materials. These models are extensively discuss in the theory of the Continuum mechanics [53]. One assumption of this thesis is the definition of deformation fields in the referential or material configuration, known with the name of Lagrangian description. When the mild tissues are loaded, they show large strains and a highly non linear behavior. If the material behaviour is considered as hyperelastic, when the acting loads disappear, it returns to its initial position. Nevertheless, when the biological tissues are subjected to cyclic loads, they show a considerable energy dissipation. The realistic constitutive models able to simulate the behavior of these kind of tissue have to take into account both aspects. The energy functions more common in the literature [51] [37] [20] will be discuss in the next sections; starting from these functions the corresponding constitutive models will be obtained. The focus of this work will be on the hyperelastic models that are the commonly used in the biomechanic fields.

3.1 Kinematic and strain-stress relation

For a body $\mathcal{B}$ that take a domain Ω_0 with boundary $\partial\Omega_0$ in the three dimensional space (undeformed configuration), it can be defined the de-

formation (fig. 3.1) through the function:

$$\mathcal{X} \ : \Omega_0 \rightarrow \Omega \tag{3.1}$$

that identify the deformed position $\mathbf{x}$ of the body $\mathcal{B}$ with the coordinate

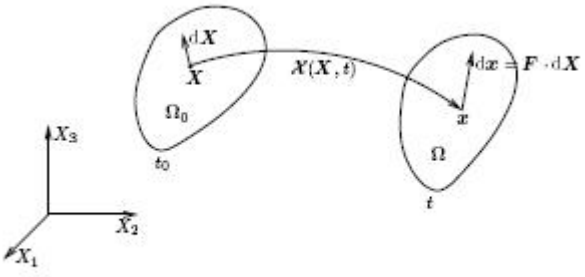

Figure 3.1: Kinematics of the continuum solid

$\mathbf{X}$ related to the undeformed configuration Ω_0, such that $\mathbf{x} = \mathcal{X}(\mathbf{X})$, where Ω is the current configuration of the body $\mathcal{B}$. The deformation gradient tensor $\mathbf{F}$ is defined as the derivative of this function respect to the vector of material coordinates [29] :

$$\mathbf{F} = \frac{\partial \mathbf{x}}{\partial \mathbf{X}} \tag{3.2}$$

The ratio between the volumes of the deformed and undeformed configuration will be indicate with $\mathbf{J} = det(\mathbf{F})$. It can be observed that $\mathbf{F^{-1}}$ is always defined because $\mathbf{X^{-1}}$ always exists. Applying the polar decomposition of the deformation gradient $\mathbf{F}$, it can be obtained:

$$\mathbf{F} = \mathbf{RU} = \mathbf{VR} \tag{3.3}$$

where the orthogonal tensor $\mathbf{R}$ is the rotational tensor and the positive symmetric tensors $\mathbf{U}$ and $\mathbf{V}$ are respectively the right and the left stretch tensors, which are related by the following expressions:

$$\mathbf{U} = \mathbf{R^T V R} \quad \text{and} \quad \mathbf{V} = \mathbf{R U R^T} \tag{3.4}$$

From the deformation gradient tensor it can be define the right and left *Cauchy-Green* tensor, respectively $\mathbf{C}$ and $\mathbf{b}$:

$$\mathbf{C} = \mathbf{F^T F} \quad \text{and} \quad \mathbf{b} = \mathbf{F F^T} \tag{3.5}$$

Using the equation (3.3) and considering that $\mathbf{R}$ is an orthogonal tensor ($\mathbf{RR^T} = \mathbf{R^TR} = \mathbf{I}$ where $\mathbf{I}$ is the identity tensor), these tensors can be expressed as:

$$\mathbf{C} = \mathbf{U^2} \quad and \quad \mathbf{b} = \mathbf{V^2} \tag{3.6}$$

The invariants of $\mathbf{C}$ are:

$$\mathbf{I_1} = tr(\mathbf{C}) \quad \mathbf{I_2} = \tfrac{1}{2}[(tr(\mathbf{C}))^2 - tr(\mathbf{C^2})] \quad \mathbf{I_3} = det\mathbf{C} \tag{3.7}$$

It's often used the *Green-Lagrange* deformation tensor, defined as

$$\mathbf{E} = \frac{1}{2}(\mathbf{C} - \mathbf{I}) \tag{3.8}$$

The stresses indicate the force divided by a unit surface of the material. Relating to the fig. 3.2, $d\mathbf{f} = \mathbf{t}ds$, where $d\mathbf{f}$ is a force applied on a surface ds. If $\mathbf{t}$ is the stress vector related to the surface $\mathbf{s}$ and $\mathbf{n}$ the normal

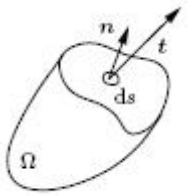

Figure 3.2: Stresses of the continuum solid

vector of the surface, the *Cauchy* theorem establishes.

$$\mathbf{t} = \boldsymbol{\sigma} \cdot \mathbf{n} \tag{3.9}$$

being $\boldsymbol{\sigma}$ the *Cauchy stress tensor*. From the angular momentum balance it can be obtained that σ is a symmetric tensor.

3.2 Time-independent models

A material can be defined as *hyperelastic* if its free energy density[1] $\boldsymbol{\Psi}$ in the reference state Ω_0 is function only of the deformation state [8], such that is possible to write $\boldsymbol{\Psi} = \boldsymbol{\Psi}(\mathbf{F})$ or $\boldsymbol{\Psi} = \boldsymbol{\Psi}(\mathbf{C})$. If the temperature

[1]The free energy is expressed by $\boldsymbol{\Psi} = e - T\eta$ where e is the intern energy density, T is the temperature and η is the entropy density

and the entropy can be considered constants, the work density of the internal forces must be equal to the free energy increment, $dW = d\mathbf{\Psi}$, and for this reason $W = W(\mathbf{F}) = W(\mathbf{C})$. The constitutive equations can be derived using the energy density functions W. For a general case (compressible material) this function can be expressed via an additive decomposition [52]:

$$W = W_{vol} + W_{iso} \tag{3.10}$$

being (W_{vol}) and (W_{iso}) the volumetric and isochoric parts, respectively. In this work the expression of the volumetric part will be considered equal to $W_{vol} = \frac{K}{2}\ln^2 J$, where K is the volumetric module [37] of the material. Starting from $\mathbf{F}$ is simple to obtain the tensor $\mathbf{E}$, so it is possible to express W as a function of the six independent components of the *Green-Lagrange* tensor $\boldsymbol{E}$. Then, the stress tensor $\boldsymbol{S}$ can be write in terms of the energy function:

$$\mathbf{S} = \frac{\partial W}{\partial \mathbf{E}} \tag{3.11}$$

$$\boldsymbol{\sigma} = \frac{1}{J}\mathbf{F}\mathbf{S}\mathbf{F}^{\mathbf{T}} = \frac{1}{J}\mathbf{F}\frac{\partial W}{\partial \mathbf{E}}\mathbf{F}^{\mathbf{T}} \tag{3.12}$$

In non linear materials, the elastic tensor $\mathcal{C}$ can be defined that for a hyperelastic material is:

$$\mathcal{C} = 4\frac{\partial^2 W}{\partial \mathbf{C}\partial \mathbf{C}} \tag{3.13}$$

From a numerical point of view this tensor is useful because it can be linearized.

3.2.1 Isotropic constitutive models

The first works in the development of models for the characterization of hyperelastic materials were presented by Mooney and Rivlin [33] [44]. Later, several deformation energy functions have been proposed by different authors [37] in order to represent the behavior of these materials. Here some of the most used energy functions will be discuss, although in this work only the Demiray model will be used in order to simulate the behaviour of the aortic wall.

- **Neo-Hookean**

  This is one of the simplest energy function and is defined as:

$$W = \frac{\mu}{2}(I_1 - 3) \tag{3.14}$$

  where μ is the constant of the model.

- **Generalized Mooney-Rivlin**

  In this model the energy function is expressed as:

$$W = \sum_{r=0}^{\infty}\sum_{s=0}^{\infty}\sum_{t=0}^{\infty} C_{rst}(I_1 - 3)^r(I_2 - 3)^s(I_3 - 1)^t \tag{3.15}$$

  where I_1, I_2 and I_3 are the invariants of the tensor $\mathbf{C}$; r, s, t are natural numbers that can vary between 0 and ∞, and C_{rst} are parameters that represent the model constants. This model has the advantage to be polynomial. Using experimental data it is possible to assign a value to these constants with the minimum square method with a reasonable range of values for r, s and t (usually between 0 and 3). When the material is totally incompressible $I_3 = 0$ and the function becomes:

$$W = \sum_{r=0}^{\infty}\sum_{s=0}^{\infty} C_{rs}(I_1 - 3)^r(I_2 - 3)^s \tag{3.16}$$

  and leads to the following formulations:

  - *One parameter Mooney-Rivlin*

    Is the simplest shape of the Mooney-Rivlin model and it considers only the first term of the equation (3.16); it coincides with the NeoHookean model and is expressed as:

$$W = C_{10}(I_1 - 3) \tag{3.17}$$

    Its capacity to simulate the soft tissue is very limited.

  - *Two parameters Mooney-Rivlin*

$$W = C_{10}(I_1 - 3) + C_{01}(I_2 - 3) \tag{3.18}$$

    Also in this case the approximation of the experimental data is limited; it can be obtained realistic results only until a 60% of stretching.

- *Three parameters Mooney-Rivlin*

$$W = C_{10}(I_1 - 3) + C_{01}(I_2 - 3) + C_{11}(I_1 - 3)(I_2 - 3) \quad (3.19)$$

The main feature of this model is that the elastic tangential module is not constant, but a good experimental approximation can be obtain for a large range of stretching.

- *Three parameters Yeoh*

$$W = C_{10}(I_1 - 3) + C_{20}(I_1 - 3)^2 + C_{30}(I_1 - 3)^3 \quad (3.20)$$

This is a high order model and have the advantage to depend only on I_1.

- **Demiray**

The energy function proposed by Demiray [10] and applied by Delfino [4] is:

$$W = \frac{a}{b}\left[\exp\left(\frac{b}{2}(I_1 - 3)\right) - 1\right] \quad (3.21)$$

This model depending only on the I_1 make easy the computational implementation. It presents good approximation also for large deformation. This model needs only two parameters, being a the sloop in the origin of the uniaxial stress-strain curve for the uniaxial tension test.

- **Odgen**

in this model the energy function is [37]:

$$W = \sum_{m=1}^{N} \frac{\mu_m}{\alpha_m}(\lambda_1^{\alpha_m} + \lambda_2^{\alpha_m} + \lambda_3^{\alpha_m} - 3) \quad (3.22)$$

where α_m and $\mu_m (m = 1, \ldots, N)$ are real number, and N is a positive natural number such that:

$$\sum_{m=1}^{N} \mu_m \alpha_m = 2G \quad (3.23)$$

where G is the transversal elastic module related to the material configuration (undeformed). Considering $N = 2$, the Ogden model is reduced to the two parameters Mooney-Rivlin model:

$$W = \frac{\mu_1}{2}(\lambda_1^2 + \lambda_2^2 + \lambda_3^2 - 3) - \frac{\mu_2}{2}(\lambda_1^{-2} + \lambda_2^{-2} + \lambda_3^{-2} - 3) \quad (3.24)$$

with $\alpha_1 = -\alpha_2 = 2$ and $\mu_1 = 2C_{10}$, $\mu_2 = -2C_{01}$, where μ_1, μ_2 and μ_3 are the own value of $\mathbf{C}$ also called principal extensions. In literature this is indicate as one of the best model for a soft tissue with very large deformation [20] [43]. The disadvantage is that setting the parameters of the model is difficult.

The stress tensor and the constitutive material model

For the computational implementation of the constitutive model described above, the expression of the stress tensor is necessary. In this work the hyperelastic model of Demiray will be extensively used; hence the expression of the second stress tensor of Piola-Kirchoff $\mathbf{S}$ and the constitutive elastic tensor $\mathbf{C}$ will be obtained. It can be observe in the equation (3.21) that the energy function depend only on the invariants of the tensor $\mathbf{C}$, and they can be expressed as:

$$I_1 = tr(\mathbf{C}) = C_{ii} = \lambda_1^2 + \lambda_2^2 + \lambda_3^2 \quad (3.25)$$

$$I_2 = \frac{1}{2}(I_1^2 - tr(\mathbf{C}^2)) = \lambda_2^2\lambda_3^2 + \lambda_3^2\lambda_1^2 + \lambda_1^2\lambda_2^2 \quad (3.26)$$

$$I_3 = (det\mathbf{F})^2 = \lambda_1^2\lambda_2^2\lambda_3^2 \quad (3.27)$$

If the incompressibility of the material can be assumed, the equation (3.27) become:

$$\lambda_1^2\lambda_2^2\lambda_3^2 = 1 \quad or \quad \lambda_1\lambda_2\lambda_3 = \det \mathbf{F} = 1 \quad (3.28)$$

From equation (3.8) and (3.11) the second stress tensor of Piola-Kirchoff can be expressed as :

$$\mathbf{S} = 2\frac{\partial W}{\partial \mathbf{C}} \quad (3.29)$$

where $\frac{\partial W}{\partial \mathbf{C}}$ have the following form:

$$\frac{\partial W}{\partial \mathbf{C}} = \frac{\partial W}{\partial I_1} \cdot \frac{\partial I_1}{\partial \mathbf{C}} + \frac{\partial W}{\partial I_2} \cdot \frac{\partial I_2}{\partial \mathbf{C}} + \frac{\partial W}{\partial I_3} \cdot \frac{\partial I_3}{\partial \mathbf{C}} \quad (3.30)$$

The derivatives of the invariants respect to the tensor $\mathbf{C}$ can be expressed as:

$$\frac{\partial I_1}{\partial \mathbf{C}} = \frac{\partial \mathbf{C}_{\mathrm{ii}}}{\partial \mathbf{C}_{\mathrm{kl}}} = \delta_{ik}\delta_{il} = \delta_{kl} \quad (3.31)$$

$$\begin{aligned}\frac{\partial I_2}{\partial \mathbf{C}} &= \frac{1}{2}\frac{\partial(\mathbf{C}_{\mathrm{ii}}\mathbf{C}_{\mathrm{jj}} - \mathbf{C}_{\mathrm{ij}}\mathbf{C}_{\mathrm{ji}})}{\partial \mathbf{C}_{\mathrm{kl}}} \\ &= \frac{1}{2}(\delta_{ik}\delta_{il}\mathbf{C}_{\mathrm{jj}} + \mathbf{C}_{\mathrm{ii}}\delta_{jk}\delta_{jl} + \mathbf{C}_{\mathrm{ji}}\delta_{ik}\delta_{jl}) - \mathbf{C}_{\mathrm{ij}}\delta_{jk}\delta_{il} \\ &= \frac{1}{2}(\delta_{kl}I_1 + I_1\delta_{kl} - 2\mathbf{C}_{\mathrm{kl}}) \\ &= I_1\delta_{kl} - \mathbf{C}_{\mathrm{kl}}\end{aligned} \tag{3.32}$$

$$\frac{\partial I_3}{\partial \mathbf{C}} = I_3\mathbf{C}^{-1} = \mathrm{cofactor}(\mathbf{C}_{\mathrm{ij}}) = \begin{pmatrix} A_{11} & A_{12} & A_{13} \\ & A_{22} & A_{23} \\ sim & & A_{33} \end{pmatrix} \tag{3.33}$$

where the coefficients of this matrix are:

$$\begin{aligned} A_{11} &= \mathbf{C}_{22}\mathbf{C}_{23} - \mathbf{C}_{23}^2 \\ A_{22} &= \mathbf{C}_{11}\mathbf{C}_{33} - \mathbf{C}_{13}^2 \\ A_{12} &= \mathbf{C}_{13}\mathbf{C}_{23} - \mathbf{C}_{12}\mathbf{C}_{33} \\ A_{33} &= \mathbf{C}_{11}\mathbf{C}_{22} - \mathbf{C}_{12}^2 \\ A_{13} &= \mathbf{C}_{12}\mathbf{C}_{23} - \mathbf{C}_{13}\mathbf{C}_{22} \\ A_{33} &= \mathbf{C}_{12}\mathbf{C}_{13} - \mathbf{C}_{23}\mathbf{C}_{11} \end{aligned} \tag{3.34}$$

Here the material is assumed as incompressible, so $I_3 = J^2 = 1$ and $\frac{\partial W}{\partial I_3} = 0$. With this hypothesis and using the equations (3.29), (3.30), (3.31) and (3.32), the second tensor of Piola-Kirchoff can be expressed as:

$$\mathbf{S}_{ij} = 2\left(\frac{\partial W}{\partial I_1}\delta_{ij} + \frac{\partial W}{\partial I_2}(I_1\delta_{ij} - \mathbf{C}_{ij})\right) \tag{3.35}$$

where $\frac{\partial W}{\partial I_i}$ depends on the energy function of the material model.
The constitutive elastic tensor is then:

$$\mathcal{C} = 2\frac{\partial \mathbf{S}}{\partial \mathbf{C}} \tag{3.36}$$

and it can be set for every specific material model. For the particular case of Demiray model, the results of interest are:

$$\frac{\partial W}{\partial I_1} = \frac{a}{2}\exp\left(\frac{b}{2}(I_1 - 3)\right) \tag{3.37}$$

The tensor $\mathbf{S}$ is expressed as:

$$\mathbf{S}_{ij} = a \cdot \exp\left(\frac{b}{2}(I_1 - 3)\right)\delta_{ij} \tag{3.38}$$

Using the equations (3.36) and (3.38), it is possible to write the elastic constitutive tensor for a Demiray material as:

$$\mathcal{C}_{ijkl} = a \cdot b \cdot \exp\left(\frac{b}{2}(I_1 - 3)\right) \delta_{kl}\delta_{ij} \tag{3.39}$$

3.2.2 Anisotropic constitutive models

According to the literature [38] [50] [25] the mechanical behaviour of the arterial tissue is anisotropic; this behaviour is related to the distribution of the collagen fiber. There are many energy function able to simulate this behavior. Among this, two of the most used in biomechanic field are discussed.

- **Holzapfel model**

  This model tries to characterize the anisotropy consistently with the arterial structure; it is based on the hypothesis that the fibers of collagen are oriented like a helix with a constant angle along the axial direction of the arteria (fig. 3.3). The general method used is based on the pseudo-invariants of Spencer [48]. This model consideres the orientation of two symmetric families of fibers defined in their reference state through the unit vectors $\mathbf{a}$ and $\mathbf{a}'$, which form symmetric angles equal to $\pm\varphi$ with the axis of the vessel. From this, it is possible to define the invariants $I_4 = \mathbf{a} \cdot \mathbf{C} \cdot \mathbf{a}$ and $I_6 = \mathbf{a}' \cdot \mathbf{C} \cdot \mathbf{a}'$.

  The incompressible model proposed by Holzapfel and Gasser [21] is defined by the energy function:

$$W = \frac{c}{2}(I_1 - 3) + \frac{k_1}{2k_2} \sum_{\alpha=4,6} \left[exp\left(k_2(I_\alpha - 1)^2\right) - 1\right] \tag{3.40}$$

  where c, k_1, k_2, φ are four positive parameter of the material. It can be seen that the expression (3.40) is additively decomposed in two parts: $W = W_{iso} + W_{aniso}$. The first one is the isotropic contribution as a Neo-hookean material, related to the elastin response; the second one is anisotropic contribution and orientate the stress along the fiber direction that define the invariants I_4 and I_6.

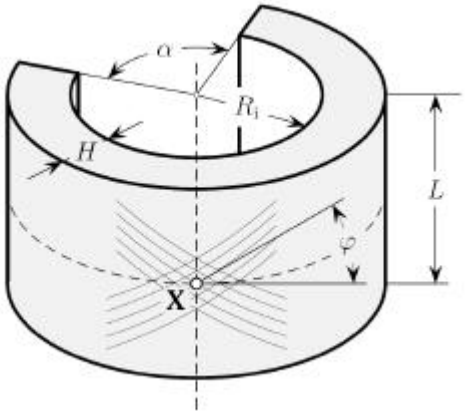

Figure 3.3: Distribution of the fibers of collagen supposed in the arterial wall for the Holzapfel model

- **Holzapfel/Demiray mixed model**

  A model based on a generalization of the previous one has been proposed by Gasser [50] , doing a combination with the Demiray model. This model set out the existence of two family of fiber but in this case they are oriented in sparse way according with the statistic distribution of Von Mises around an average angle φ. The energy function for this model is:

$$W = \frac{c}{2}(I_1 - 3) + \frac{k_1}{2k_2} \sum_{\alpha=4,6} \left[exp\left(k_2 \left[\kappa I_1 + (1 - 3\kappa) I_\alpha - 1\right]^2\right) - 1\right] \tag{3.41}$$

  The variables have the same meaning that in equations (3.40) and (3.21) but here the constant κ represents the dispersion of the fibers and it has a value that can vary between 0 and 1/3. For $\kappa = 0$ the equation (3.41) is reduced to the model of Holzapfel (3.40), while if $\kappa = 1/3$ the model is reduced to an isotropic model similar to the Demiray's one (3.21).

3.3 Time-dependent model

Although in this thesis the dissipative feature of the arterial wall has been neglected, it is a better approximation of the behaviour of arteries and

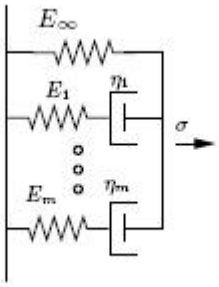

Figure 3.4: Scheme of the Maxwell model

a lot of authors proposed viscoelasticity models applied to the arterial vessels or the aorta. In the work of Rodriguez [46], Taylor [42] and of Holzapfel [20] is possible to find an elaboration of the subject starting from the generalized viscoelastic model of Maxwell (fig. 3.5).

3.4 Computational validation of the constitutive model

In the model of the arterial wall that will be shown in the chapter 6, the Demiray material model has been chosen and used; this because it allow to simulate the mechanical behaviour of the aorta wall in a very realistic way as shown in other experimental works [19].The parameters that can be used in order to fit the experimental data are easily found; besides, it is simple to implement in the commercial code as ABAQUS [1].
The implementation is done on ABAQUS through a subroutine written in Fortran programming language which name is UHYPER (appendix A). In the programmed code the user have to specify the number of the parameters used (in this case a and b), the density energy function (W) and the first and second derivative of this function respect to the invariants of the right tensor of Cauchy-Green $\mathbf{C}$; in this way is possible to define the second tensor of Piola-Kirchoff $\mathbf{S}$ and the tangent constitutive tensor $\mathcal{C}$.

In the next subsection a brief validation of the Demiray constitutive model implementation will be presented, comparing the obtained FEM results with the analytical solution. The tests that have been used in

order to validate the FEM implementation are the simple uniaxial tension test and a cylinder under internal pressure.

3.4.1 Uniaxial traction

A piece of dimensions 1 mm width, 1 mm thickness and 5 mm length has been analyzed. It has been modeled using an hexaedral element with eight nodes. It has been imposed a displacement in the X direction and with free movements in the Y and Z directions, as shown in figure 3.5. The final displacement has been imposed increasing them with steps of 0.1 mm until the final displacements, equal to 2.3 time the original length ($\lambda = 2.3$), have been reached.

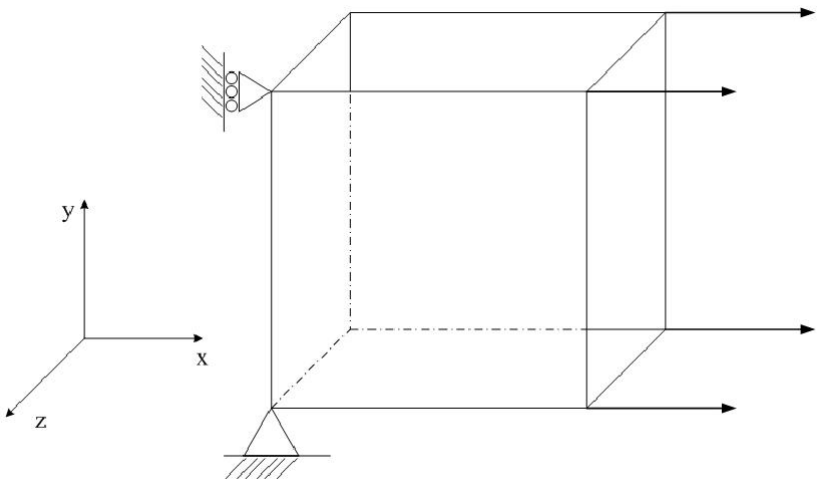

Figure 3.5: Scheme of the element used in the simulation of the simple tension test

The constitutive parameters used in this simulation are: $a = 30$ kPa and $b = 1.1$. Figure 3.6 shows three different steps of the simulation corresponding to $\lambda = 1$ (original configuration), $\lambda = 1.7$, and $\lambda = 2.3$ (being $\lambda = l_f/l_0$).

In this particular case, only the X component of the Cauchy stress is computed because the other components are zero. This aspect, combined with the incompressibility condition leads to a relation that allows to write the stress only in terms of the parameters a and b and in terms of the elongation in the X direction (λ). From the incompressibility condition we have :

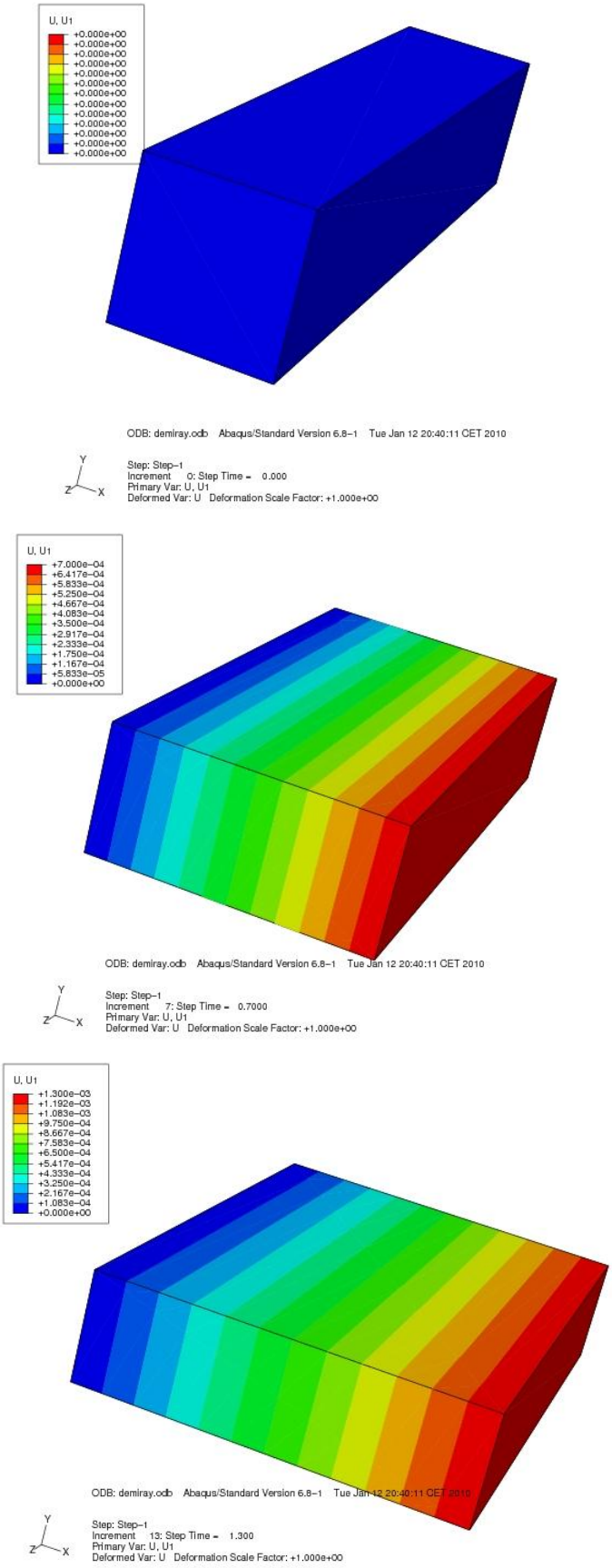

Figure 3.6: Model with $\lambda = 1$, $\lambda = 1.7$, and $\lambda = 2.3$

$$\lambda_2 = \lambda_3 = \frac{1}{\sqrt{\lambda}} \tag{3.42}$$

Solving (3.35), and (3.36) we obtain the Cauchy stress in the direction of elongation:

$$\sigma_1 = 2\left(\lambda^2 - \frac{1}{\lambda}\right)\left(\frac{\partial W}{\partial I_1} + \frac{1}{\lambda}\frac{\partial W}{\partial I_2}\right) \tag{3.43}$$

From equation (3.43), and taking into account the equation (3.21), the Cauchy stress can be written as

$$\sigma_1 = 2\left(\lambda^2 - \frac{1}{\lambda}\right) exp\left[\frac{b}{2}\left(\lambda^2 + \frac{2}{\lambda} - 3\right)\right] \tag{3.44}$$

The numerical results of the ABAQUS analysis have been extracted in a Excel sheet and compared with the analytical solution for the Demiray model (equation (3.44)). In figure 3.7 can be seen the perfect correlation between the numerical and analytical values of the stress.

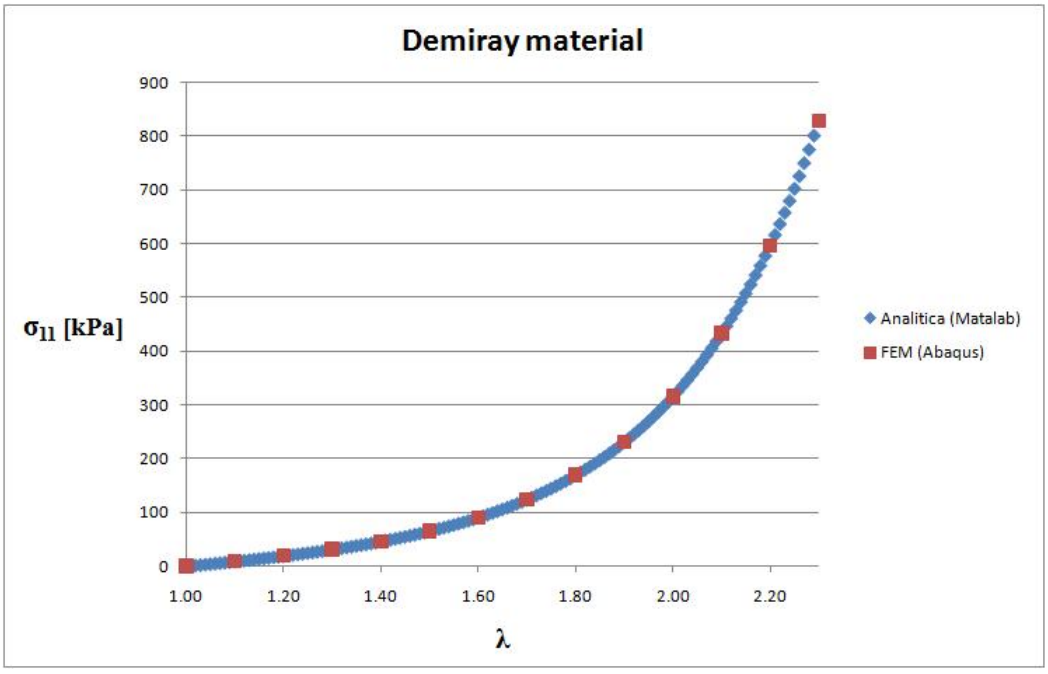

Figure 3.7: Analytical and FEM stress solution for the Demiray model in a simple uniaxial traction test

3.4.2 Cylinder under internal pressure

This test analyzes the mechanical behavior of a cylindrical vessel subjected to internal pressure and with the double end fixed in the axial

direction (figure 3.8).

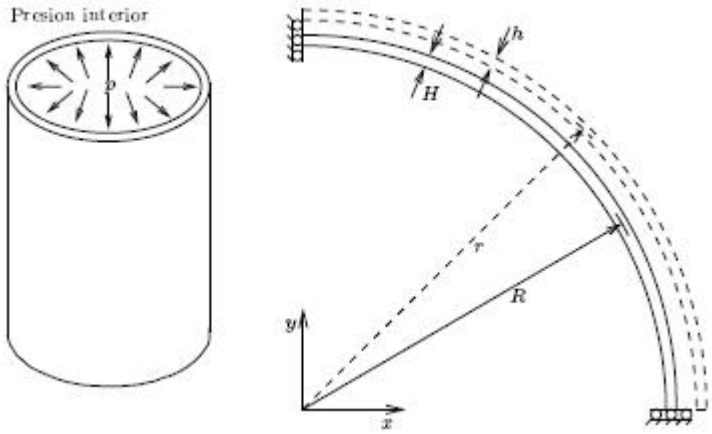

Figure 3.8: Scheme of the cylindrical model with axial symmetry

The radius of the cylinder is $R = 9mm$ and the thickness of the wall is $H = 0.04mm$. The properties of the material are: $a = 10$ kPa and $b = 1.1$.

In order to obtain the analytical solution the thin wall theory ($H << R$) will be considered, then the circumferential stress is constant along the wall thickness.

The analytical results are obtained considering a isotropic and incompressible material such that:

$$W(\lambda_1, \lambda_2, \lambda_3) = W(\lambda, \frac{1}{\lambda}, 1) = W(\lambda) \tag{3.45}$$

where λ_1 is the elongation in the circumferential direction, λ_2 in the radial direction and λ_3 in the longitudinal direction. In this conditions the cylinder have zero radial stress and :

$$\sigma = \lambda \frac{\partial W}{\partial \lambda} \tag{3.46}$$

From the equilibrium of the forces, the internal pressure p and the circumferential stress are related through the equation:

$$p = \frac{\sigma h}{r} \tag{3.47}$$

with $h = H/\lambda$ and $r = \lambda R$.

In this way the analytic solution for the implemented material is obtained for this case:

$$p = \frac{aH}{R}\left(1 - \frac{1}{\lambda^4}\right) \cdot exp\left(\frac{b}{2}\left[\lambda^2 + \frac{1}{\lambda^2} - 2\right]\right) \tag{3.48}$$

In this test, computed in ABAQUS, the pressure increase linearly from zero to 180 Pa with step of 15 Pa and the computed displacements are extracted. This methodology allows to plot the results in the λ - p plane of figure 3.9 where can be seen the correlation between the numerical and analytical values of pressure.

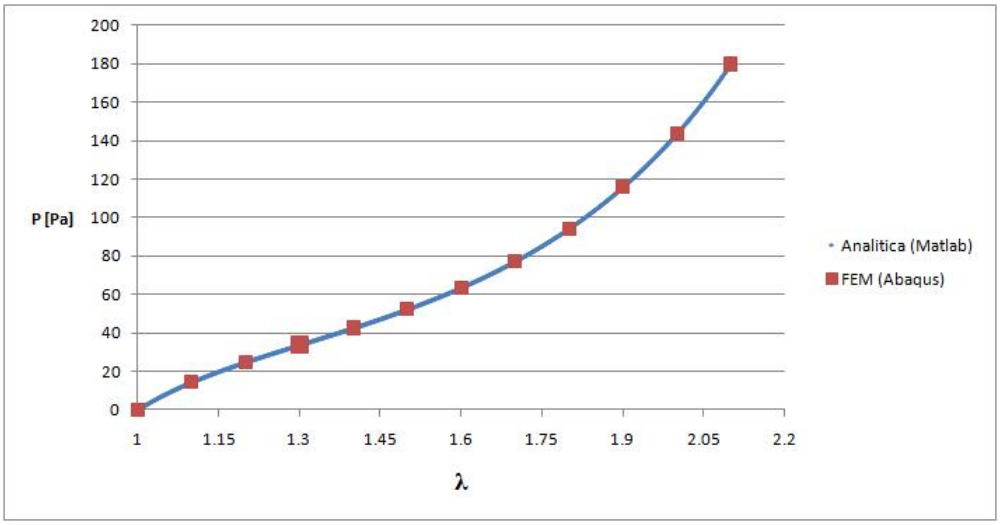

Figure 3.9: Cylinder under pressure: analytical and FEM solution for the demiray constitutive model

Chapter 4

Computational model of blood flow

In this chapter the assumptions on the behavior of blood flow in large arteries are discussed and the Navier-Stokes formulation for the Newtonian and incompressible fluid is described. Furthermore a validation of the finite volume methods (FVM) for some simple flow case is done using the commercial code Star CD.

4.1 Description of blood properties

The blood is a liquid tissue composed of one part of cells, like red cells, white cells and platelets (45% of total volume), and a liquid part called plasma which consists primarily of water (45% of the total volume). Its physiological temperature is about 36.5°C and its viscosity is five times greater than the water [5]. Two things derive from these considerations [13]:

- Cellular solid particles suspended in the blood offer a certain resistance to the flow, with energy dissipation. This phenomenon is associated with the blood viscosity properties.
- The large amount of water present in the blood gives the property of incompressibility.

Therefore, any constitutive model that aims at the macroscopic level must at least consider these two characteristics of blood: viscosity and

incompressibility. The red blood cells are able to deform and accumulate elastic energy although, when they are not aggregated, the elastic forces are much lower than the viscose. When the shear rate is low, there is a phenomenon that affects red blood cells: the formation of aggregates which are called *rouleaux*. It consists in the union of several red blood cells to form a single body (figure 4.1), increasing the viscosity of blood. In this situation, even for low values of hematocrit[1], the viscosity increases with decreasing gradient (shear rate) by a certain value as can be seen in figure 4.2. On the other hand, the forces that are created to break down these aggregates also produce an important elastic deformation in red blood cell, as well as a change of orientation, resulting in a storage of elastic energy in the microstructure of blood [41].

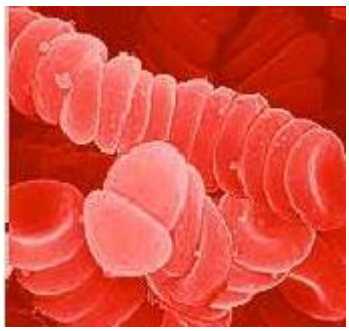

Figure 4.1: Erythrocytes united in aggregates called *rouleaux*

Consider now, for greater clarity and simplicity, a one-dimensional flow and that the variables are scalars rather than vectors as they are. The deformation gradient will be denoted by γ and its time derivative, which is the rate of the deformation gradient or shear rate with $\dot{\gamma}$. When this value is high enough ($\dot{\gamma} > 100s^{-1}$), red blood cells are aligned with the flow and do not have the formation of *rouleaux* and in this case the viscosity does not depend on $\dot{\gamma}$, it is constant and therefore the blood can be considered as Newtonian fluid (Figure 4.3).This is the situation for the large arteries and therefore also for the aorta. This is an important consideration useful to justify the constitutive model adopted in this work for modeling the fluid dynamics in the aorta and described later in this chapter.

There are several models in the state of the art that reflect this non-Newtonian properties of blood. This is done imposing an asymptotic

[1]Volume ratio between erythrocytes and blood (Ht)

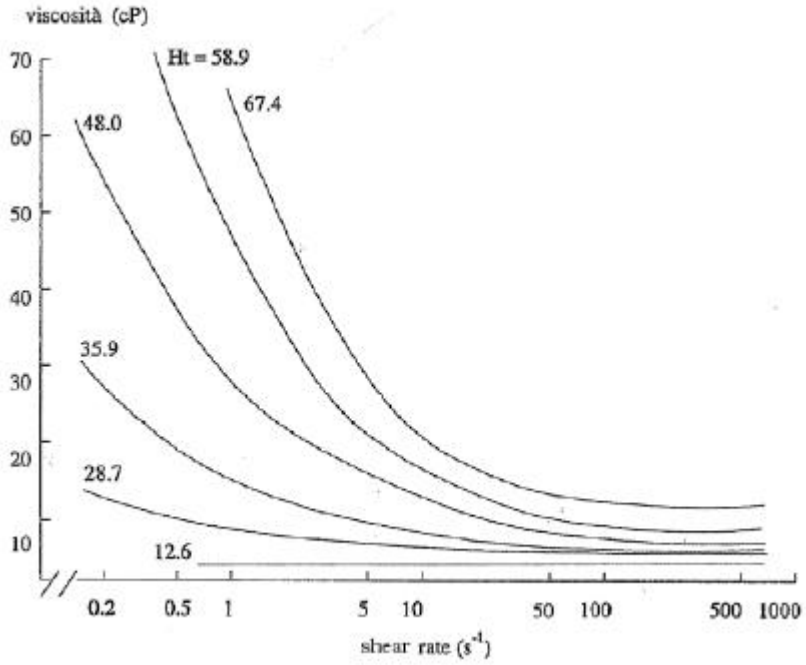

Figure 4.2: Evolution of blood viscosity as a function of shear strain rate and hematocrit.

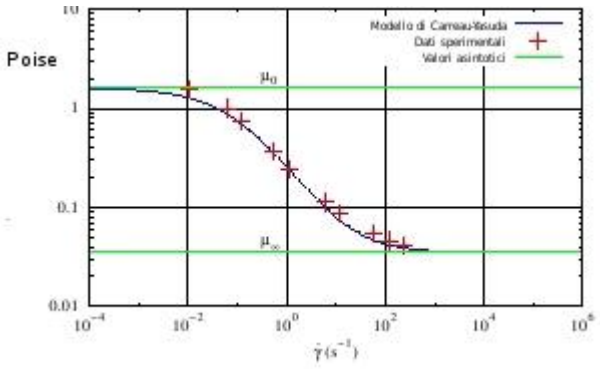

Figure 4.3: Experimental data and value of the Carreau-Yasuda model

model with the following conditions:

$$\lim_{\dot{\gamma}\to 0} \mu(\dot{\gamma}) = \mu_0 \tag{4.1}$$

$$\lim_{\dot{\gamma}\to \infty} \mu(\dot{\gamma}) = \mu_\infty \tag{4.2}$$

On this line, one of the most used models is that of *Carreau-Yasuda* [47] that has the following expression:

$$\mu(\dot{\gamma}) = \mu_\infty + (\mu_0 - \mu_\infty)(1 + (\lambda\dot{\gamma})^a)^{\frac{n-1}{a}} \tag{4.3}$$

with λ, n and a constants of the fluid.Then, using experimental data on the viscosity of blood, it is possible to calibrate the model obtaining the value of the three constants; in the example of figure 4.3, the three constants have the following values $\lambda = 8.2$ s, $a = 0.64$ and $n = 0.213$.

4.2 Formulation of the flow model

4.2.1 Constitutive law

The expression of the stress tensor of a fluid is written as

$$\boldsymbol{\sigma} = -p\mathbf{I} + \boldsymbol{\sigma}_\mu \tag{4.4}$$

where p is a scalar field, $\mathbf{I}$ is the identity tensor and $\boldsymbol{\sigma}_\mu$ is the stress tensor due to the viscous properties of the fluid. To determine $\boldsymbol{\sigma}_\mu$ the first point to assess in hemodynamics to characterize the behavior of the blood is whether the characteristics of memory, the viscoelastic behavior, have to be considered or not. The memory of a fluid determines the number of tensors necessary to approximate the tension. Anyway the memory comes from the elastic properties of the particles when they are deformed. Following this criterion we can distinguish [40]:

- Fluids of first order.
  Fluids that contain small particles and have no memory (elastic but not viscoelastic behavior). The local stresses are determined only by local deformations, excluding strains that incorporate effects due to time derivatives of the deformation, contradicting the principle

of strain rate localization [16]. In these type of fluids the tensor $\boldsymbol{\sigma}_\mu$ is only related with the velocity gradient tensor:

$$\boldsymbol{\sigma}_\mu = \mu(\nabla \mathbf{u} + \nabla^T \mathbf{u}) = 2\mu \frac{1}{2}(\nabla \mathbf{u} + \nabla^T \mathbf{u}) = 2\mu \mathbf{D} \qquad (4.5)$$

where $\mathbf{D} = \frac{1}{2}(\nabla \mathbf{u} + \nabla^T \mathbf{u})$ is the symmetric part of the velocity gradient tensor.

If the fluid must be modeled as a first-order fluid, the second point of the discussion is whether it can be considered Newtonian or not, that is, if the viscosity can be held constant or dependent on shear rate.

- Newtonian fluids
  Fluids that have a linear relation between $\boldsymbol{\sigma}$ and $\mathbf{D}$. Physically it means that the viscosity does not depend on the shear rate.

- Non Newtonian fluids
  Fluids that have a non linear relation between $\boldsymbol{\sigma}$ and $\mathbf{D}$. In this case the viscosity depends on the deformation rate: $\mu = \mu(\dot{\gamma})$. The significance of $\dot{\gamma}$ is intuitive in a one-dimensional case; for a general case is defined as $\dot{\gamma} = \sqrt{2\mathbf{D} : \mathbf{D}}$.

- Second order fluids[2]
  They are viscoelastic fluids that include higher order derivative tensor. $\boldsymbol{\sigma}_\mu$ can be expressed as:

$$\boldsymbol{\sigma}_\mu = \alpha_1 \mathbf{D} + \alpha_2 \mathbf{A_2} + \alpha_3 \mathbf{D^2} \qquad (4.6)$$

  where α_i are constitutive parameters (constants or functions of the tensor $\mathbf{D}$) and $\mathbf{A}_2$ is the second strain tensor of *Rivlin-Ericksen* [9].

[2]This classification does not include all fluid types but is valid for the most suitable models of the blood

As pointed out above, when the strain rate $\dot{\gamma}$ is low, the formation of *rouleaux* can be presumable; this fact changes the viscosity, and a storage of elastic energy is observed. As a first hypothesis we ignore the effects of elasticity and we consider the blood as a first order fluid. The justification for this hypothesis is that the *rouleaux* appear only in special cases [17]. On the other hand, the variation in blood viscosity suggests that the blood can not be taken as a Newtonian fluid *a priori* . In order to decide the model to be used, table 4.1 shows the values of $\dot{\gamma}$ and the Reynolds number in several vessels of the circulation system [27].

Vessel	$\dot{\gamma}$	Reynolds
Aorta	155	3400
Arteries	900	500
Arterioles	8000	0.7
Capillaries	1000	0.002
Venules	800	0.01
Veins	160	140
Vena cava	100	3300

Table 4.1: Estimation of $\dot{\gamma}$ assuming parabolic flow

Entering in the curve of figure 4.2 in the case of the aorta we get a constant value of viscosity (μ_∞) therefore the model presented in this work considers the blood as a Newtonian fluid.

Another characteristic of fluids and continuum medium in general, are the ability to change volume when subjected to a certain stress state, that are the compressibility properties. The physical quantity capable of expressing this property is the variation of density with pressure. If this does not change significantly the fluid is considered incompressible. The main component within the blood, present in the plasma directly and indirectly in the red and white blood cells and platelets, is water. The modulus of compression or volumetric modulus of the water is:

$$E_v = \frac{\Delta P}{\frac{\Delta \rho_f}{\rho_f}} = 2.15 \cdot 10^9 Pa \tag{4.7}$$

where P is the pressure and ρ_f is the density.

Then the water can be considered incompressible and this feature can be translate directly to the macroscopic features of the blood. This translates into the equation of mass conservation as

$$\nabla \cdot \mathbf{u} = 0 \tag{4.8}$$

being $\nabla\cdot$ the divergence operator and $\mathbf{u}$ the velocity vector.

In every line of the circulatory tree, phenomena also exist for the exchange of gases and substances with the cells, but they are not considered, for the purpose of this work. Also the contribution of the gravitational forces to the equation of momentum conservation will not be considered because these forces are negligible when compared with other acting forces.

4.2.2 Navier-Stokes equations. Strong formulation

The equation of momentum balance

$$\nabla \cdot \boldsymbol{\sigma} = \rho_f \dot{\mathbf{u}} \tag{4.9}$$

where $\dot{\mathbf{u}}$ is the material derivative of velocity, and it can be expressed in eulerian coordinates as

$$\nabla \cdot \boldsymbol{\sigma} = \rho_f \left(\frac{\partial \mathbf{u}}{\partial t} + \mathbf{u} \cdot \nabla \mathbf{u} \right) \tag{4.10}$$

On the other hand, we assume the Newtonian fluid constitutive behaviour:

$$\boldsymbol{\sigma} = -p\mathbf{I} + 2\mu\mathbf{D} \tag{4.11}$$

Substituting (4.11) in the dynamic equation (4.10), it is obtained:

$$\rho_f \left(\frac{\partial \mathbf{u}}{\partial t} + \mathbf{u} \cdot \nabla \mathbf{u} \right) + \nabla p - 2\mu \nabla \cdot \mathbf{D} = 0 \tag{4.12}$$

This equation together with the incompressibility condition (4.8) give the Navier-Stokes equation.

Boundary conditions can be assessed as velocities imposed, tension imposed, or a combination of these:

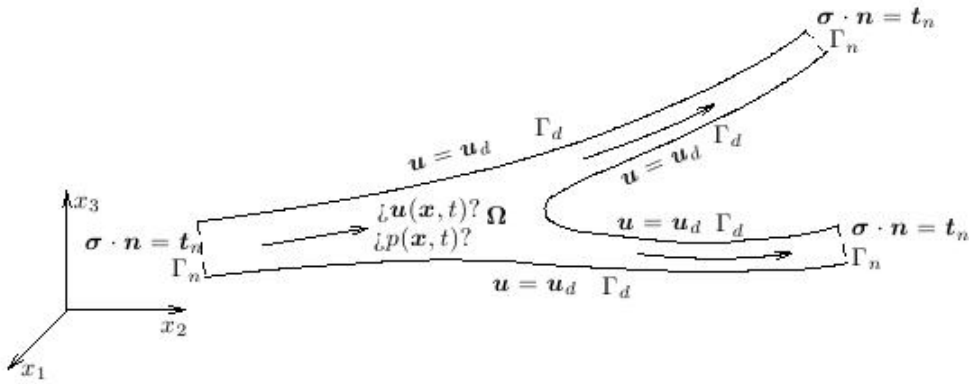

Figure 4.4: Schematic representation of the strong formulation of the fluid dynamic problem.

$$\begin{aligned} \mathbf{u} = \mathbf{u}_d \quad in\Gamma_d \quad (Dirichlet \quad boundary \quad conditions) \\ \boldsymbol{\sigma} \cdot \mathbf{n} = \mathbf{t}_n \quad in\Gamma_n \quad (Neumann \quad bounday \quad conditions) \end{aligned} \tag{4.13}$$

where $\Gamma_d \cup \Gamma_n = \Gamma, \Gamma_d \cap \Gamma_n = \oslash$ and $\mathbf{n}$ is the normal vector to the surface Γ_n. The strong formulation of the problem is set in the following way: If $\Omega \in \mathbb{R}^3$ is the fluid domain; $\mathbf{u}_d(t) and \mathbf{t}_n(t)$ given boundary conditions and $\mathbf{u_0}(\mathbf{x})$ given initial conditions; the problem is to find a vectorial field $\mathbf{u}(\mathbf{x},t) : \Omega \times [0,T] \to \mathbb{R}^3$ and a scalar field $p(\mathbf{x},t) : \Omega \times [0,T] \to \mathbb{R}^3$ such that:

$$\begin{aligned} \rho_f \left(\frac{\partial \mathbf{u}}{\partial t} + \mathbf{u} \cdot \nabla \mathbf{u} \right) + \nabla p - 2\mu \nabla \cdot \mathbf{D} = 0 \quad & \Omega \times (0,T) \\ \nabla \cdot \mathbf{u} = 0 \quad & \Omega \times (0,T) \\ \mathbf{u} = \mathbf{u}_d(t) \quad & \Gamma_d \times (0,T) \\ \boldsymbol{\sigma} \cdot \mathbf{n} = \mathbf{t}_n(t) \quad & \Gamma_n \times (0,T) \\ \mathbf{u}(\mathbf{x},0) = \mathbf{u}_0(\mathbf{x}) \quad & \Omega, t = 0 \end{aligned} \tag{4.14}$$

4.3 Validation: flow inside a cylinder

In the previous section the features of the blood properties has been already discussed. Particularly in the case of the aorta, the blood can

be assumed as an incompressible fluid ; then the density of the fluid (ρ_f) can be considered as a constant. Also the viscosity of the fluid can be considered as a constant value in our case (μ_f) . Besides the blood has been considered as a newtonian fluid.
This values (see table 4.2) and this features will be used for this validation and also for the computational model aorta showed in the next chapter.

Property	Value
ρ_f	1064 Kg/m^3
μ_f	0.0035 Pa$\cdot s$

Table 4.2: Properties of the blood used in the simulations

All the simulations showed in this work that concern to the blood flow have been performed using the commercial code Star CD [3].
This is a code that use the FVM (Finite Volume Method) technology and gives the opportunity to uptake a novel mesh technology based on the use of polyhedral elements. The methodology used for the generation of the meshes of the models will be explained in chapter 6.
In next sections the geometry and the mesh (figure 4.5) used will be the same for all the simulations. It is a cylinder of radius $R = 10.195$ mm and length $L = 20$ cm.

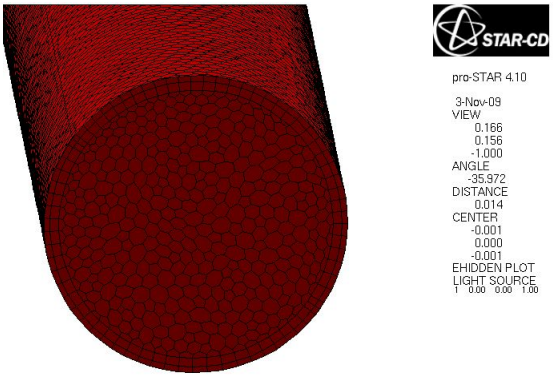

Figure 4.5: Mesh of the cylinder

The boundary conditions used are the following (see also figure 4.6):

- velocity boundary condition at the inlet
- constant zero pressure condition at the outlet
- no slip condition at the wall of the cylinder

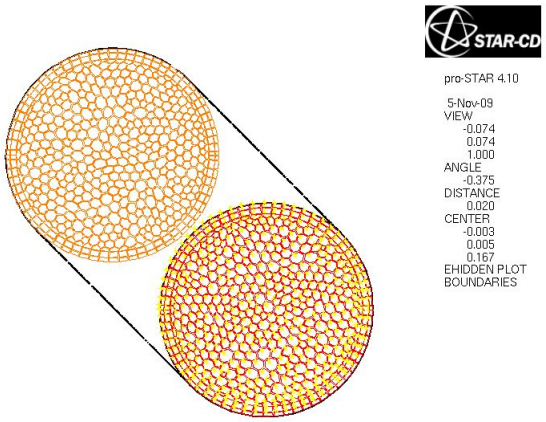

Figure 4.6: Schematic representation of the boundary regions

4.3.1 Steady state analysis: Pouiseille flow

This first simulation is a steady state analysis of the laminar flow inside the cylinder described with a low Reynolds number, in order to analyze the development of the Pouiseille flow.
The velocity have a uniform distribution at the inlet region, with the axial velocity (W_i=0.005 m/s) and the other components equal to zero. The Reybolds number in this case will be:

$$Re = \frac{\rho \bar{v} D}{\mu_s} \backsimeq 30.1 \tag{4.15}$$

where $\bar{v}$ is the average velocity in the section and in this case equal to the inlet velocity W_i. From the theory [12] the developing length of the Pouiseille flow is equal to:

$$x = 0.056 \cdot D \cdot Re \backsimeq 0.035m \tag{4.16}$$

In the figure 4.7 is possible to appreciate the developing length of the flow, while in the figure 4.8 is possible to see the velocity distribution

along the diameter of the cylinder at different distances from the inlet. The values showed in the graph are obtained smoothing the values at the cells, that is converting the cells data to vertex data. The boundary conditions are not conserved in this process, particularly the non slip wall condition; for this reason the values showed on the extreme of the diameter are not exactly zero.

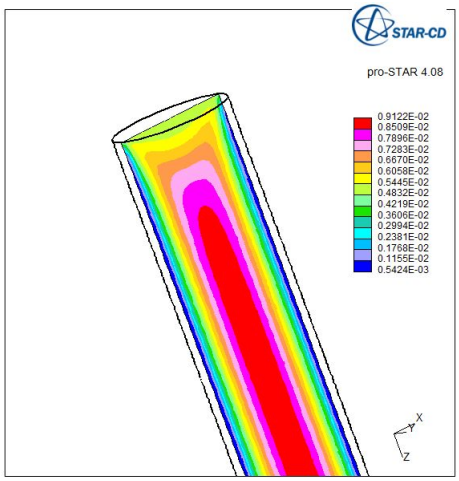

Figure 4.7: Colored scalar map of the velocity component along the axial direction. A longitudinal section

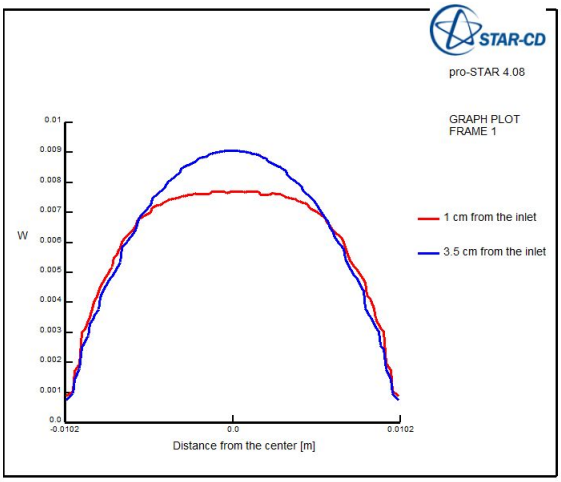

Figure 4.8: Magnitude of the W component of velocity (m/s) along the diameter (the unit is the meter) of the cylinder at different distance from the inlet

It is possible to see the parabolic distribution of velocity only at 3.5 centimeter from the inlet, where the flow is completely developed. The

velocity distribution from the Poiseuille law and the mass conservation law is:

$$W(r) = \frac{\Delta P \cdot R^2}{4\mu L}\left[1 - \left(\frac{r}{R}\right)^2\right] = 2W_i\left[1 - \left(\frac{r}{R}\right)^2\right] \tag{4.17}$$

4.3.2 Transient analysis: constant and uniform inlet velocity

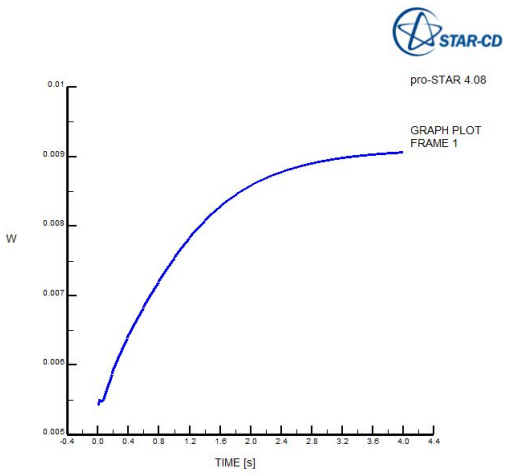

Figure 4.9: W component of velocity (m/s) at the central cell of the outlet section during the simulation

In this simulation a transient analysis has been done; also in this case the velocity have a constant distribution at the inlet but the flow needs time before to be completely developed.
The time step used for the simulation was of 0.01 seconds and the simulation run for 4 seconds, starting from an initial condition of zero velocity and pressure everywhere in the domain.

In the figure 4.10 is reported the magnitude of the W velocity component at different step of the simulation at the longitudinal section of the cylinder.
In the figure 4.9 is shown the velocity component W at the central cell at the outlet section in every time step.
Through these charts it is possible to appreciate the dynamic of the fluid motion.

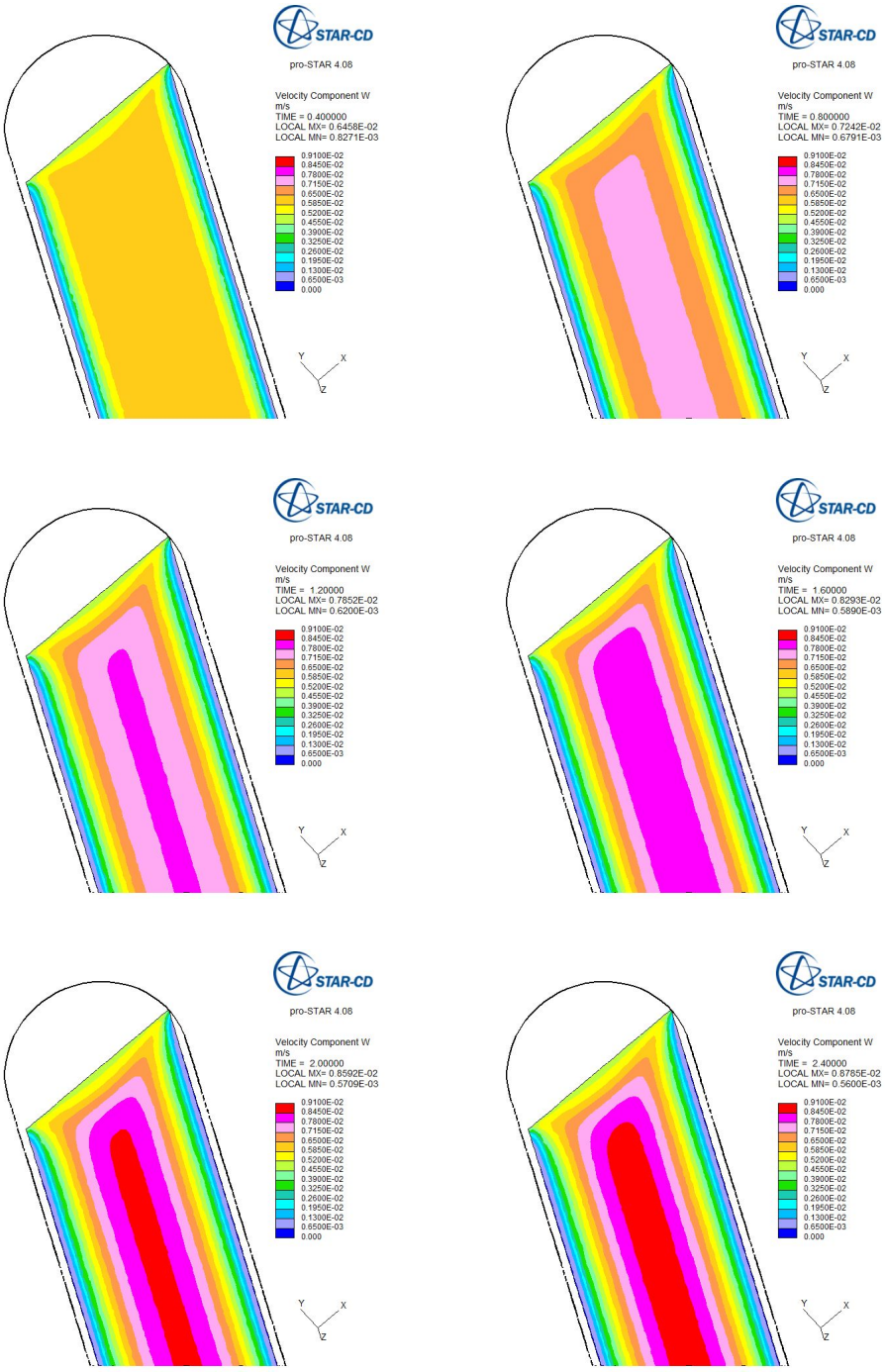

Figure 4.10: W velocity component at the time=0.4 s, 0.8 s, 1.2 s, 1.6 s, 2 s and 2.4 s

Chapter 5

Overview on the Fluid-Structure Interaction

In previous chapters it has been described the mathematical models for the arterial wall and the blood flow. The main objectives of these chapters were to show adjusted constitutive equations considering the physiological features of the cardiovascular system, and to provide some simple validation test through the finite element method FEM (for the structural part) and the finite volume method FVM (for the fluid part), taking into account of the incompressibility condition. The subject of this chapter is to give a general overview on the different ways to coupling these two systems. The fluid and the structural part have common boundaries in ours models and it is necessary to couple the two systems imposing the suitable compatibility conditions in the common boundaries.
The general equation governing the coupling and the difference between different computational methods for the fluid structure interaction (FSI) will be presented. Some of these methods will be applied in our models and the description of other methods will be useful in order to understand the limitations of the proposed models and to improve the study for further works.

In the next sections the mathematical models for the so called *Two way coupling* will be presented. The main feature of these algorithms for FSI analysis is based on the fact that the fluid domain is not fixed and it adapts itself to the solid movement. For this reason the lagrangian formulation of the solid can be keep, but the eulerian formulation for

the fluid must be modified for a changing domain. In the first section it will be show the most general formulation for a fluid domain adapting to moving boundaries. It will be pointed out the mathematical formulation of the problem of interaction introducing some mathematical operators that allow to write the formulation of the equations in a concise form in order to classify the various methods.

5.1 ALE formulation of the fluid

The ALE formulation (*Arbitrary Lagrangian-Eulerian*) is the right method to set out the fluid equations with no-fixed boundaries. Essentially this method makes flexible the mesh allowing to take up a arbitrary domain. In this way it is not necessary that the mesh follow the material movement (like in the lagrangian formulation of the solid) or that the mesh is fixed in the space (like in the eulerian formulation of the fluid), but this mesh is allowed to take up any arbitrary spatial domain (from this the word arbitrary).
Ones of the firsts articles in which this method appear in the context of the finite elements methods is theta of Donea [23] and Hughes [24]. Later this method has been used both for fluids with a mobile boundaries and for solid with large displacements.

5.1.1 Theoretical basis of ALE formulation

The basic idea of this method is showed in figure 5.1. A water drop enters in the reference domain but any node of the mesh is joined with a particular material of the drop and the nodes of the mesh move regardless of the movement of the drop.
The ALE formulation is based on three functions [11] that link the material and spatial domains, as showed in figure 5.2. The function Φ[1] is the characteristic application of the ALE formulation, and it relate the referential domain points $\mathcal{X}$ with the spatial point $\mathbf{x}$:

$$\Phi : \Omega_{\mathcal{X}} \times [t_0, t_{final}] \rightarrow \Omega_x \times [t_0, t_{final}] \tag{5.1}$$

[1]In the contest of the finite element method the Φ function define the mesh moviment (see fig. 5.1)

$$(\mathcal{X}, t) \rightarrow \Phi(\mathcal{X}, t) = (\mathbf{x}, t) \tag{5.2}$$

The mesh velocity $\hat{\mathbf{u}}$ is the derivative of the function Φ with respect to the time[2]:

$$\hat{\mathbf{u}} = \frac{\partial \Phi(\mathcal{X}, t)}{\partial t} = \frac{\partial \mathbf{x}}{\partial t}\Big|_{\mathcal{X}} \tag{5.3}$$

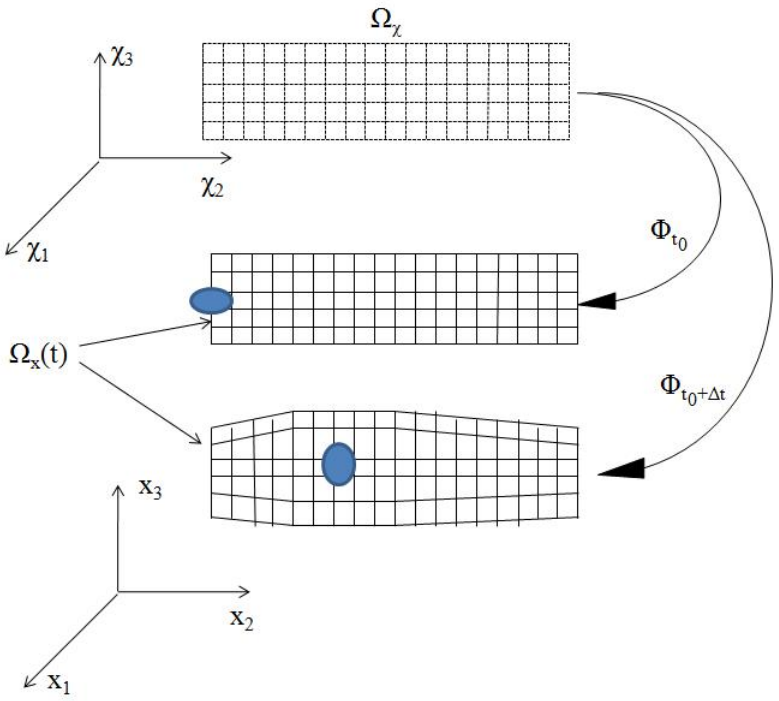

Figure 5.1: Key idea of ALE formulation for a fluid with a non-fixed boundaries

In this coordinate system any magnitude f can be expressed as:

$$\mathbf{f} = \mathbf{f}(\mathcal{X}, t) \qquad \mathcal{X} \in \Omega_{\mathcal{X}} \tag{5.4}$$

where the difference respect to the eulerian or lagrangian formulation is that $\Omega_{\mathcal{X}}$ is not referred neither to the spatial coordinate or the material coordinate. The temporal material derivative of $\mathbf{f}$ is calculated as[3]:

[2]Setting out the ALE formulation, the domain will be considered always fixed when deriving with respect to the time. For example, in the equation (5.3) the derivative is made considering the domain $\Omega_{\mathcal{X}}$ fixed

[3]The material derivative is calculated because it have a physical meaning and it is useful in the dynamic equations

$$\dot{\mathbf{f}} \equiv \frac{\partial \mathbf{f}}{\partial t}\Big|_{\mathbf{x}} = \frac{\partial \mathbf{f}}{\partial t}\Big|_{\mathcal{X}} + \frac{\partial \mathbf{f}}{\partial \mathcal{X}} \frac{\partial \mathcal{X}}{\partial t}\Big|_{\mathbf{x}} \tag{5.5}$$

If $\mathbf{w}$ is defined as the velocity of a material particle with respect to the reference domain $\Omega_{\mathcal{X}}$:

$$\mathbf{w} = \frac{\partial \mathcal{X}}{\partial t}\Big|_{\mathbf{x}} \tag{5.6}$$

then substituting the equation (5.6) in the equation (5.5) :

$$\frac{\partial \mathbf{f}}{\partial t}\Big|_{\mathbf{x}} = \frac{\partial \mathbf{f}}{\partial t} + \frac{\partial \mathbf{f}}{\partial \mathcal{X}} \mathbf{w} \tag{5.7}$$

However is useful to write the material derivative as a function of the spatial gradient, that have a physical meaning in the Navier-Stokes equation. The equation (5.7) can be written as:

$$\frac{\partial \mathbf{f}}{\partial t}\Big|_{\mathbf{x}} = \frac{\partial \mathbf{f}}{\partial t}\Big|_{\mathcal{X}} + \frac{\partial \mathbf{f}}{\partial \mathbf{x}} \frac{\partial \mathbf{x}}{\partial \mathcal{X}} \mathbf{w} \tag{5.8}$$

being necessary to calculate $\frac{\partial \mathbf{x}}{\partial \mathcal{X}} \mathbf{w}$. For this reason the material velocity of the fluid particles must be calculated :

$$\mathbf{u} \equiv \frac{\partial \mathbf{x}}{\partial t}\Big|_{\mathbf{x}} = \frac{\partial \mathbf{x}}{\partial t}\Big|_{\mathcal{X}} + \frac{\partial \mathbf{x}}{\partial \mathcal{X}} \frac{\partial \mathcal{X}}{\partial t}\Big|_{\mathbf{x}} \tag{5.9}$$

Substituting equations (5.3) and (5.6) in the equation (5.9) :

$$\mathbf{u} = \hat{\mathbf{u}} + \frac{\partial \mathbf{x}}{\partial \mathcal{X}} \mathbf{w} \tag{5.10}$$

It is possible to define the convective velocity as the difference between the material velocity and the mesh velocity $\hat{\mathbf{u}}$:

$$\mathbf{c} = \mathbf{u} - \hat{\mathbf{u}} \tag{5.11}$$

and taking into account equation (5.10):

$$\mathbf{c} = \frac{\partial \mathbf{x}}{\partial \mathcal{X}} \mathbf{w} \tag{5.12}$$

Using this result the material derivative (5.8) can be expressed as:

$$\frac{\partial \mathbf{f}}{\partial t}\Big|_{\mathbf{x}} = \frac{\partial \mathbf{f}}{\partial t}\Big|_{\mathcal{X}} + \mathbf{c} \cdot \nabla \mathbf{f} \tag{5.13}$$

where ∇ is the spatial gradient[4].

[4]The lagrangian and eurelian formulation are particular cases of the ALE formulation. With $\mathbf{c} = 0$ the lagrangian formulation is recovered; with $\mathbf{c} = \mathbf{u}$ the eulerian one is recovered

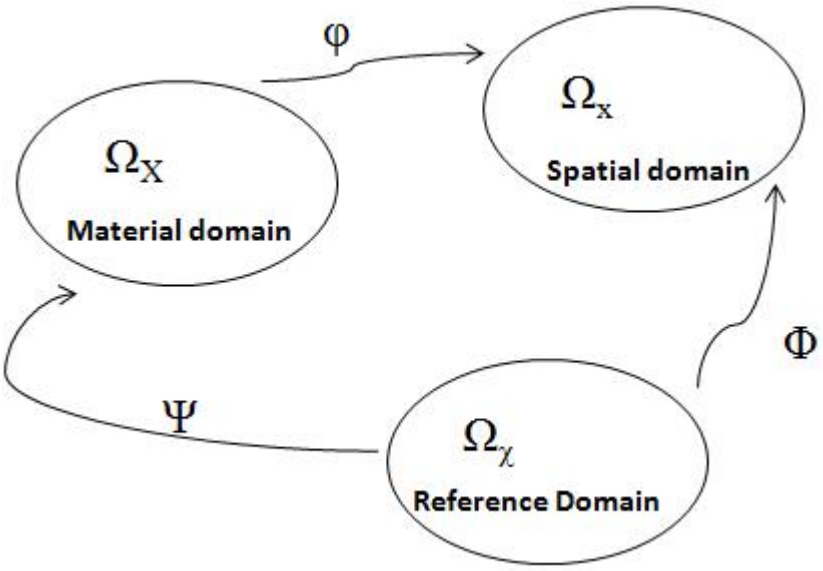

Figure 5.2: The lagrangian, eulerian and ALE domains

5.1.2 Equations of a fluid with non-fixed boundaries

Using the equations above it is possible to rewrite the eulerian formulation of fluid dynamics. Applying the equation (5.13), the material acceleration is:

$$\dot{\mathbf{u}} \equiv \frac{\partial \mathbf{u}}{\partial t}\Big|_{\mathbf{x}} = \frac{\partial \mathbf{u}}{\partial t}\Big|_{x} + \mathbf{c} \cdot \nabla \mathbf{u} \tag{5.14}$$

Using the ALE formulation it is also possible to rewrite the strong formulation of the fluid movement ((4.14)) in the following way: *A fluid domain* $\Omega(t) \in \mathbb{R}^3$ *is given. Find a vectorial field of velocity* $\mathbf{u}(\mathbf{x}, t) \to \mathbb{R}^3$ *and a scalar field of pressure* $p(\mathbf{x}, t) \to \mathbb{R}$ *such that*:

$$\begin{aligned} \rho_f(\frac{\partial \mathbf{u}}{\partial t} + \mathbf{c} \cdot \nabla \mathbf{u}) + \nabla p - 2\mu \nabla \cdot \mathbf{D} = 0 \qquad & in \quad \Omega(t) \\ \nabla \cdot \mathbf{u} = 0 \qquad & in \quad \Omega(t) \\ \mathbf{u} = \mathbf{u}_d(t) \qquad & in \quad \Gamma_d(t) \\ \boldsymbol{\sigma} \cdot \mathbf{n} = \mathbf{t}_n(t) \qquad & in \quad \Gamma_d(t) \end{aligned} \tag{5.15}$$

where $\mathbf{c}$ must satisfy:

$$\mathbf{c}(t) = \mathbf{u}_d(t) - \dot{\Gamma}_d(t) \qquad in \quad \Gamma_d(t) \tag{5.16}$$

where $\dot{\Gamma}_d(t)$ is the velocity of the boundary when a Dirichlet boundary condition is used.

5.1.3 Computational implementation

The implementation of the ALE formulation it's done on the equations already discussed in the chapter 4. The convective term changes and it becomes:

$$\rho_f \mathbf{c} \cdot \nabla \mathbf{u} = \rho_f (\mathbf{u} - \hat{\mathbf{u}}) \cdot \nabla \mathbf{u} \tag{5.17}$$

If we define $\hat{\mathbf{u}}_\mathbf{A}$ as the velocity of the mesh nodes, the following step is to calculate these velocities. Usually, if the displacements of the fluid boundary $\mathbf{d}_\Gamma$ are known:

- The displacements of the internal nodes are computed as the displacements of the nodes of a fictitious stationary solid with imposed displacements in its boundaries. The goal is to have an internal displacement as smooth as possible without a high computational cost. For this reason the constitutive equation of a linear elastic isotropic solid is used, which is similar to the Stokes flow, and the same fluid element can be used with zero density. If $\hat{\mathbf{d}}$ is the mesh displacement, starting from the boundary displacement $\mathbf{d}_\Gamma$ is possible to define a operator $\mathcal{M}$ such that

  $$\hat{\mathbf{d}} = \mathcal{M}(\mathbf{d}_\Gamma) \tag{5.18}$$

  In Souli et al. [28] other definitions of this operator are established always in order to smooth displacements of the internal mesh nodes.

- The velocity of the mesh is computed as:

  $$\hat{\mathbf{u}}^{n+1} = \frac{\hat{\mathbf{d}}^{n+1} - \hat{\mathbf{d}}^n}{\Delta t} \tag{5.19}$$

5.2 Formulation of the FSI problem

In a FSI problem boundary movement are *a priori* unknowns. Starting from the assessment of the movement of this boundary at time t, the next steps of the calculations are the following:

- With the operator $\mathcal{M}$ the new mesh is obtained, and using the equation (5.19) the velocity of the mesh is calculated
- Solve the fluid equation with the ALE formulation.
- From the fluid velocities calculated in the previous point, the stress and the nodal forces at the interface are obtained.
- Solve the solid equations using as boundary condition the calculated forces at the interface.
- Solving the solid equation, the displacement at the interface[5] can be evaluated.

Some operator can help to write the formulation of the problem in a more compact way. These operator can be used to make simpler the numerical solution of the required steps [14].

If the time is discretized, the solution at the time t^n is supposed to be known; the operator $\mathcal{M}$ will be used in order to calculate the solution at the time t^{n+1}. It is necessary to define formally the operator $\mathcal{M}$:

$$(\mathbf{d}_\Gamma^{n+1}) \rightarrow \mathcal{M}(\mathbf{d}_\Gamma^{n+1}) = \hat{\mathbf{d}}^{n+1} \tag{5.20}$$

where $\mathbf{d}_\Gamma^{n+1}$ is the current displacement of the interface $\Gamma_{n+1} \in \mathbb{R}^2$ and $\hat{\mathbf{d}}^{n+1}$ is the current displacement of the complete mesh of the domain $\Omega_f^{n+1} \in \mathbb{R}^3$. Now, calling $\hat{\mathbf{u}}^{n+1}$ the current velocity of the mesh $\Omega_f^{n+1} \in \mathbb{R}$ and $\mathbf{u}^n$ the velocity of the fluid in Ω_f^n at the previous instant, $\mathcal{F}$ can be defined as the operator that, starting from $\hat{\mathbf{d}}^{n+1}$, $\hat{\mathbf{u}}^{n+1}$ and $\mathbf{u}^n$, calculate the current velocity $\mathbf{u}^{n+1}$ of the fluid domain $\Omega_f^{n+1} \in \mathbb{R}^3$ and the current forces $\mathbf{f}_\Gamma^{n+1}$ on the interface $\Gamma^{n+1} \in \mathbb{R}^2$:

$$(\hat{\mathbf{d}}^{n+1}, \hat{\mathbf{u}}^{n+1}, \mathbf{u}^n) \rightarrow \mathcal{F}(\hat{\mathbf{d}}^{n+1}, \hat{\mathbf{u}}^{n+1}, \mathbf{u}^n) = (\mathbf{u}^{n+1}, \mathbf{f}_\Gamma^{n+1}) \tag{5.21}$$

where $\mathcal{F}$ solve the fluid dynamics equations (5.15). In order to write all in a shorter form, using the equation (5.19) it is possible to write :

[5]The interface will be indicated with Γ, although it can change with time as $\Gamma(t)$; this dependence will be omitted. Ω_f and Ω_s will be indicate the fluid and the solid domain respectively

$$\mathbf{f}_\Gamma^{n+1} = \mathcal{F}(\hat{\mathbf{d}}^{n+1}) \tag{5.22}$$

so that the operator $\mathcal{F}$ can be considered like an application that couple the vector of the displacement $\hat{\mathbf{d}}^{n+1}$ defined in the fluid domain and the vector of the forces $\mathbf{f}_\Gamma^{n+1}$ defined at the interface.

In order to define the operator $\mathcal{S}$, vectors $\mathbf{d}^n$ and $\dot{\mathbf{d}}^n$ are the displacement and the velocity in the solid domain $\Omega_s^n \in \mathbb{R}^3$, $\mathcal{S}$ is defined as an operator that give the current displacement $\mathbf{d}^{n+1}$ and the current displacement velocity $\dot{\mathbf{d}}^{n+1}$ in $\Omega_s^{n+1} \in \mathbb{R}^3$ starting from $\mathbf{f}_\Gamma^{n+1}$, $\mathbf{d}^n$ and $\dot{\mathbf{d}}^n$, and solving the solid equations described in the chapter 3 :

$$(\mathbf{f}_\Gamma^{n+1}, \mathbf{d}^n, \dot{\mathbf{d}}^{\mathbf{n}}) \rightarrow \mathcal{S}(\mathbf{f}_\Gamma^{n+1}, \mathbf{d}^n, \dot{\mathbf{d}}^n) = (\mathbf{d}^{n+1}, \dot{\mathbf{d}}^{n+1}) \tag{5.23}$$

As it has done previously it can be written:

$$(\mathbf{d}_\Gamma^{n+1}) = \mathcal{S}(\mathbf{f}_\Gamma^{n+1}) \tag{5.24}$$

so that the operator $\mathcal{S}$ can be considered like an application that couple the vector of the forces $\mathbf{f}_\Gamma^{n+1}$ and the vector of the displacement $\mathbf{d}_\Gamma^{n+1}$, both defined at the interface.

The three operator described above are used sequentially[6] in order to solve the FSI problem, and the output of one of them is the input of the next one (see figure 5.3).

If the solution at t^n is known, then the displacement $\mathbf{d}_\Gamma^{n+1}$ of the interface $\Gamma^{n+1} \in \mathbb{R}^2$ at the instant t^{n+1} is the solution of the function:

$$\mathcal{S} \circ \mathcal{F} \circ \mathcal{M}(\mathbf{d}_\Gamma^{n+1}) = \mathbf{d}_\Gamma^{n+1} \tag{5.25}$$

The equation (5.25) is the so called *fundamental equation of the interaction problem*. This is an implicit equation and it is not possible to have a closed form of the solution $\mathbf{d}_\Gamma^{n+1}$ especially because of the non-linearity of $\mathcal{F}$. For this reason is necessary to apply numerical methods like that of the fixed point.

[6]It is important to underline that the operator $\mathcal{M}$ is linear (look the definition), the operator $\mathcal{F}$ is clearly non-linear because it include the convective term of the fluid equations, and the operator $\mathcal{S}$ can be linear or non-linear because depend on which kind of material and kinematics are used in the model; for example, if the material is an hyperelastic material the operator $\mathcal{S}$ is non-linear

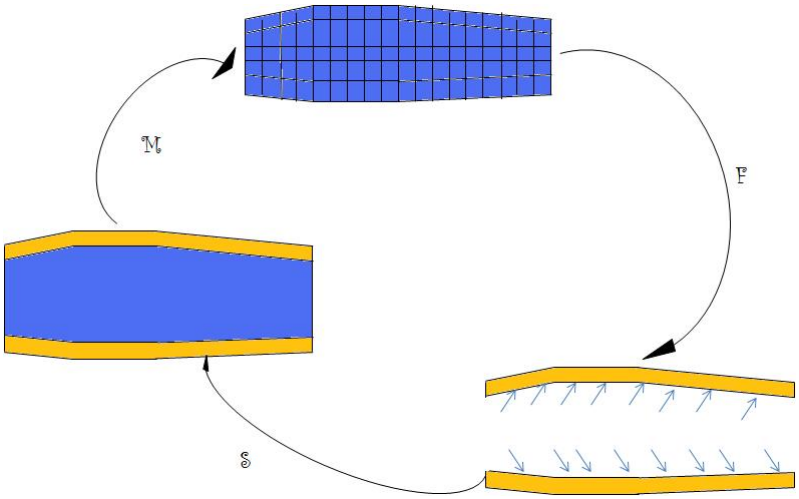

Figure 5.3: Operator used to solve the interation problem

5.3 Classification of the FSI methods

For clarity we can write the equation (5.25) as:

$$\mathcal{S} \circ \mathcal{F} \circ \mathcal{M}(\mathbf{d}_\Gamma^{n+1}) - \mathbf{d}_\Gamma^{n+1} = 0 \tag{5.26}$$

Using the idendity operator $\mathcal{I}$ it is possible to write:

$$\mathcal{R}(\mathbf{d}_\Gamma^{n+1}) = 0 \qquad where \qquad \mathcal{R} = \mathcal{S} \circ \mathcal{F} \circ \mathcal{M} - \mathcal{I} \tag{5.27}$$

$\mathcal{R}$ is the so called residual operator. We said that this is a non-linear equation that can be solved with different methods: middle point method, Newton-Raphson method and the fixed point method.

In order to solve this equation is possible to use a specific program for the fluid and another for the solid, or it is possible the use of specialized programs that solve together the equations of the solid and the fluid. When two different programs are used the method is called partitioned otherwise is called monolithic.

5.3.1 Monolithic methods

The idea of the monolithic methods is to solve the equation(5.27) with a tangent method so that a superlinear order of convergence is obtained. For this reason the tangent matrix have to be calculated; this is calculated by deriving the equation 5.27 with respect to $\mathbf{d}_\Gamma^{n+1}$. If the derivative of the operators is indicated with an apostrophe on the operator:

$$\mathcal{R}'(\mathbf{d}_\Gamma^{n+1}) = [\mathcal{S}' \circ \mathcal{F} \circ \mathcal{M}(\mathbf{d}_\Gamma^{n+1})] \cdot [\mathcal{F}' \circ \mathcal{M}(\mathbf{d}_\Gamma^{n+1})] \cdot \mathcal{M}'(\mathbf{d}_\Gamma^{n+1}) - \mathcal{I} \quad (5.28)$$

where

$$\begin{aligned} \mathcal{M}'(\mathbf{d}_\Gamma^{n+1}) &= \frac{\partial \hat{\mathbf{d}}^{n+1}}{\partial \mathbf{d}_\Gamma^{n+1}} \\ \mathcal{F}'(\hat{\mathbf{d}}^{n+1}) &= \frac{\partial \mathbf{f}_\Gamma^{n+1}}{\partial \hat{\mathbf{d}}^{n+1}} \\ \mathcal{S}'(\mathbf{f}_\Gamma^{n+1}) &= \frac{\partial \mathbf{d}_\Gamma^{n+1}}{\partial \mathbf{f}_\Gamma^{n+1}} \end{aligned} \quad (5.29)$$

$\mathcal{M}'$ is simple to calculate because $\mathcal{M}$ is a linear operator. $\mathcal{S}'$ can be obtained from the standar form of the non-linear solid mechanics. $\mathcal{F}'$ is more complicate to calculate because of the variation of the fluid domain Ω_f. A deeper analysis of these issues can be found in Mattehies [30] [31] and Gerbeau [15] [14].

5.3.2 Partitionated methods

The goal of partitioned methods is to use independent codes for the fluid and the solid, solving the corresponding models and then solving the problem of interaction. Here we analyze the methods of weak coupling and strong coupling. For the schematic representation of these two models, they will be referred to a three-dimensional grid in which the axis x will be the time step and the axis y the k iterations within each time step. In z the system of the solid is represented with a square and with a circle that of the fluid. In this scheme the resolution of the mesh with the operator $\mathcal{M}$ is incorporated into the fluid system to improve the clarity of the graph so that the resolution of the fluid system assumes the meaning to solve the operation $\mathcal{F} \circ \mathcal{M}$.

Weak coupling

This method advances in each time step without internal interactions between the fluid-solid system, such that the method does not totally couple the two systems. With this technique you fast forward in time with

the inconvenience of not doing a complete coupling, so the method can easily be unstable. Hence the name of the method of explicit coupling, as a method only conditionally stable.

In figures 5.4 and 5.5 the patterns of resolution can be observed, for the parallel and serial weak coupling respectively. Both systems (fluid and solid) exchange information at the end of each time step and this information is used to proceed with the solution in the next time step. For the parallel scheme we have:

$$\begin{aligned} \mathbf{f}_\Gamma^{n+1} &= \mathcal{F} \circ \mathcal{M}(\mathbf{d}_\Gamma^n) \\ \mathbf{d}_\Gamma^{n+1} &= \mathcal{S}(\mathbf{f}_\Gamma^n) \end{aligned} \tag{5.30}$$

And for the serial scheme:

$$\begin{aligned} \mathbf{f}_\Gamma^{n+1} &= \mathcal{F} \circ \mathcal{M}(\mathbf{d}_\Gamma^n) \\ \mathbf{d}_\Gamma^{n+1} &= \mathcal{S}(\mathbf{f}_\Gamma^{n+1}) \end{aligned} \tag{5.31}$$

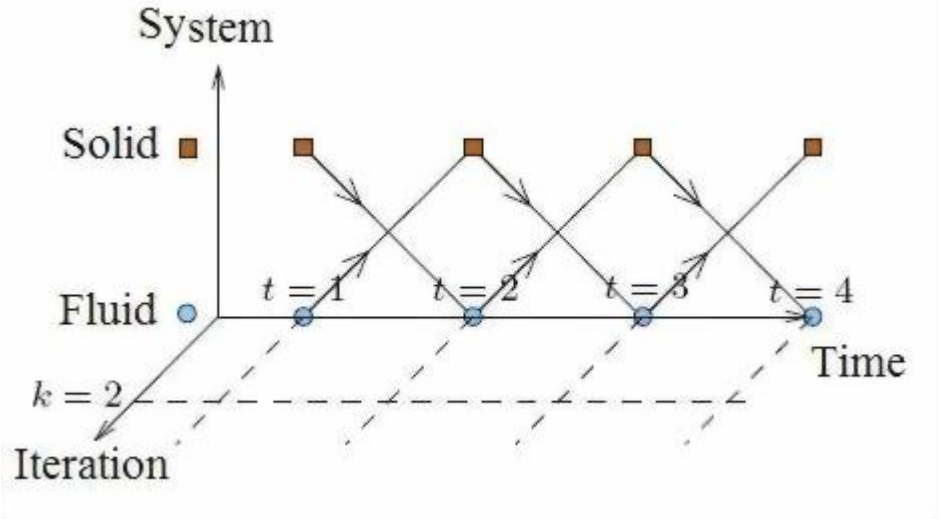

Figure 5.4: Parallel solution scheme for the weak coupling

It has been studied experimental cases in which these schemes are unstable due to the effect of the so-called *additional mass effect* [34]. Developing the equations of the solid, the normal force (pressure) at the

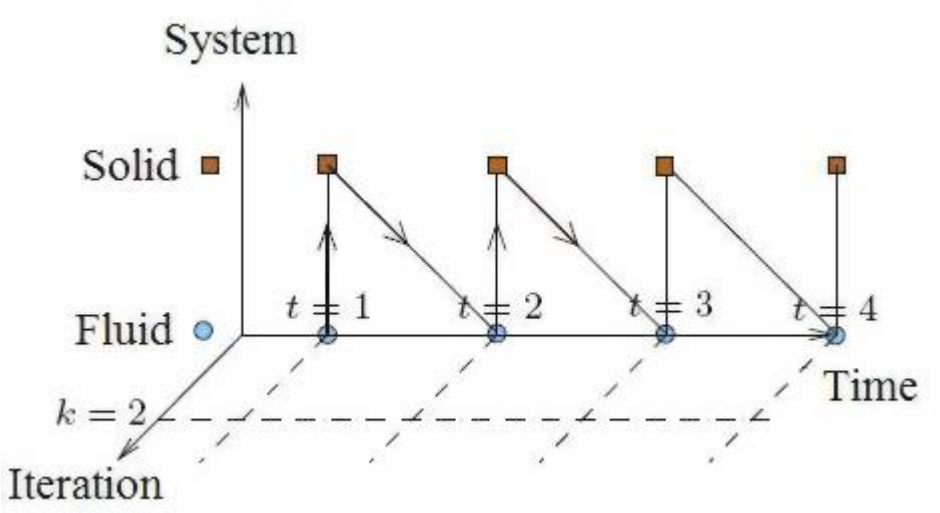

Figure 5.5: Serial solution scheme for the weak coupling

interface Γ fluid-solid depends on the acceleration and the density of the fluid. Consequently in the equation of the solid a term of inertia appear:

$$(\rho_s \mathbf{M}_s + \rho_f \mathbf{M}_f)\frac{\partial^2 \mathbf{d}}{\partial t^2} \tag{5.32}$$

where the matrix $\mathbf{M}_s$ is the mass matrix of the solid and $\mathbf{M}_f$ come from the fluid equations.The additional mass is precisely the term $\rho_f \mathbf{M}_f$. In the equation (5.32) is observed that if the density of the solid is much greater than that of the fluid ($\rho_s \mathbf{M}_s \gg \rho_f \mathbf{M}_f$) the effect of the additional mass is negligible such as in cases of aerodynamic structures subject to wind strength, where the air density is several orders of magnitude smaller than the density of the solid. In this case, a scheme partitioned with weak coupling can work well. If the density of the fluid is similar to that of the solid as in hemodynamics, the effect of additional mass assumes importance and is a source of numerical instability of the described problem [34].

Strong coupling

The methods of the strong coupling are based on equation (5.33) which has an appropriate structure to be solved by the method of the fixed point. In the equation:

$$\mathcal{S} \circ \mathcal{F} \circ \mathcal{M}(\mathbf{d}_\Gamma^{n+1}) = \mathbf{d}_\Gamma^{n+1} \tag{5.33}$$

it is supposed that the solution at the instant t^n is known and we want to get the solution at t^{n+1}. To solve the equation (5.33) we can use patterns similar to those of iterative methods of Jacobi and Gauss-Seidel in systems of linear equations. In the context of fluid-structure interaction these methods are called Block-Jacobi and Block-Gauss-Seidel.

The degree of coupling achieved with these methods is the same as that obtained by the monolithic methods but usually require more interactions for each time step[7]. These iterations require an extraordinary increase in the computational cost, so that, for an acceptable degree of tolerance for the coupling, tens of iterations are needed.

Block-Jacobi method

This method is based on the parallel solution of the fluid-solid system, exchanging information of both systems after each iteration. The scheme is shown in the figure 5.6.

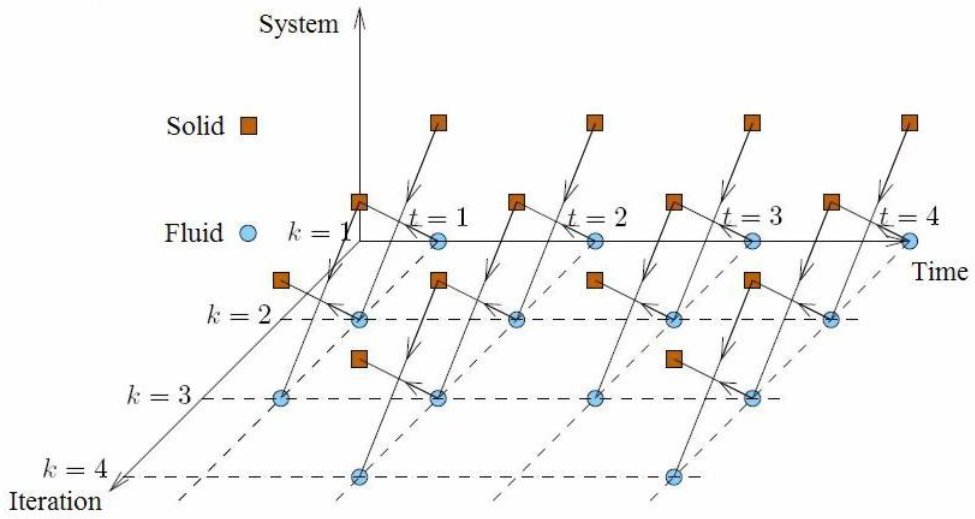

Figure 5.6: Block-Jacobi method: parallel solution scheme for the strong coupling

In this example, for the first time step three iterations to achieve the convergence (in accordance with a predetermined tolerance) are needed. In the second time step four iterations are needed, etc. . In each iteration new forces and a new interface position is obtained in accordance with the equations:

[7]So called subiteractions

$$\begin{aligned} \mathbf{f}_{\Gamma,k+1}^{n+1} &= \mathcal{F} \circ \mathcal{M}(\mathbf{d}_{\Gamma,k}^{n+1}) \\ \mathbf{d}_{\Gamma,k+1}^{n+1} &= \mathcal{S}(\mathbf{f}_{\Gamma,k}^{n+1}) \end{aligned} \tag{5.34}$$

where the index k has been used to denote the iterations. In the equation (5.34) is more clear that both systems can be solved in parallel and that in order to obtain the solutions in the $k+1$ iteration only the solutions in the k iteration are required.

Block-Gauss-Seidel method

This method solves a system and transfers the result to the other before to finish the step. Consequently, the systems are solved sequentially. The figure 5.7 shows the scheme of this method.

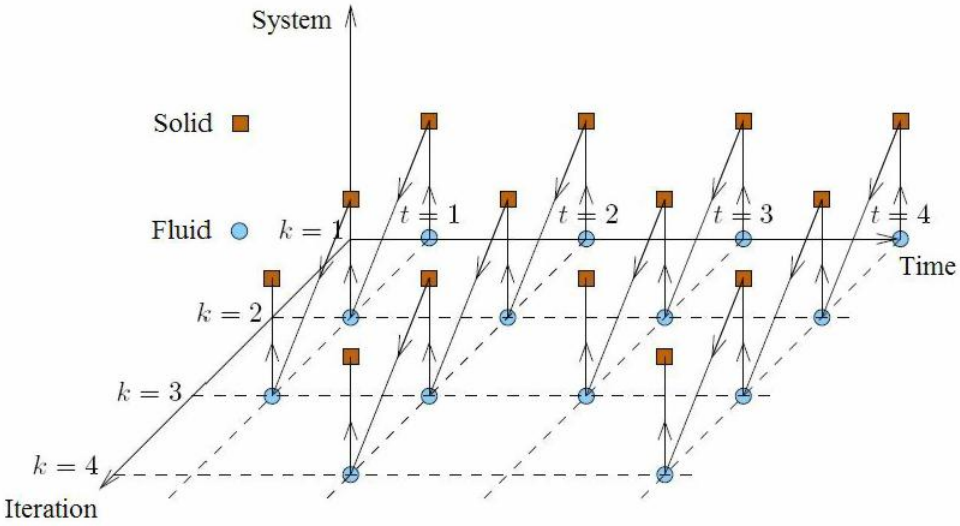

Figure 5.7: Block-Gauss-Seidel method: series solution scheme for the strong coupling

In this case the information of the fluid system is transfered to the solid system in the same iteration.
The force and displacement in each iteration in this case are:

$$\begin{aligned} \mathbf{f}_{\Gamma,k+1}^{n+1} &= \mathcal{F} \circ \mathcal{M}(\mathbf{d}_{\Gamma,k}^{n+1}) \\ \mathbf{d}_{\Gamma,k+1}^{n+1} &= \mathcal{S}(\mathbf{f}_{\Gamma,k+1}^{n+1}) \end{aligned} \tag{5.35}$$

In this method another operator $\mathcal{A}$ is introduced.

$$\mathcal{A} \equiv \mathcal{S} \circ \mathcal{F} \circ \mathcal{M} \tag{5.36}$$

so equation (5.33) become:

$$\mathcal{A}(\mathbf{d}_\Gamma^{n+1}) = \mathbf{d}_\Gamma^{n+1} \tag{5.37}$$

where we express the unknown $\mathbf{d}_\Gamma^{n+1}$ as a fixed point of the operator $\mathcal{A}$ (table (5.1)).

Initial step	$\mathbf{d}_{\Gamma,0}^{n+1}$
Iteration 1	$\mathbf{d}_{\Gamma,1}^{n+1} = \mathcal{A}(\mathbf{d}_{\Gamma,0}^{n+1})$
Iteration 2	$\mathbf{d}_{\Gamma,2}^{n+1} = \mathcal{A}(\mathbf{d}_{\Gamma,1}^{n+1})$
$\vdots$	$\vdots$
Iteration k	$\mathbf{d}_{\Gamma,k}^{n+1} = \mathcal{A}(\mathbf{d}_{\Gamma,k-1}^{n+1})$

Table 5.1: Scheme of the fixed point iterative method

5.4 Validation test: the flow through an elastic pipe

In this test a linear elastic tube with Young's modulus E will be considered. Consequently, the radius of such a tube is variable. Imagine such a pipe filled with fluid at rest and surrounded by fluid (see figure 5.8). Let the wall thickness of the tube be h, the radius of the tube r, the exterior pressure p_0, and the interior pressure be p.
The change in p, namely $(p - p_0)$, is called the *trasmural pressure difference*. The thickness of the wall h will be considered small compared with the resting radius of the pipe. Consequently, as a good approximation we can treat the wall as a thin elastic membrane.

Let T denote the tension per unit length of the tube and per unit thickness. Let us consider the equilibrium of a half of such a long cylinder pipe together with the fluid contained in it. The net downward force per

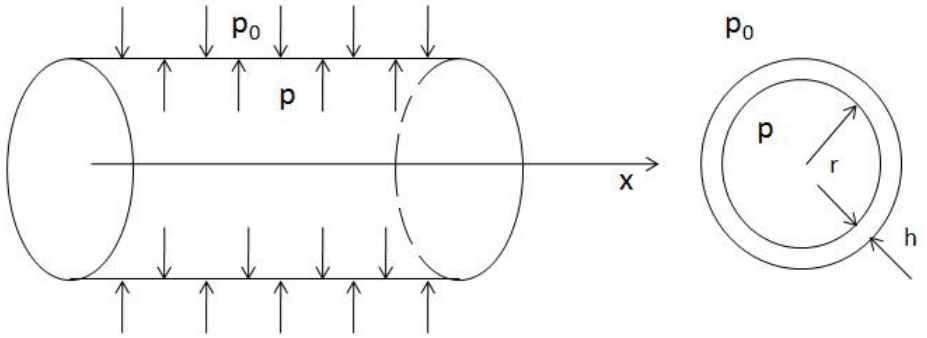

Figure 5.8: An elastic tube filled with fluid at rest and surrounded by fluid

unit length on this half cylinder is $2Th$ and it is balanced by the net upward force per unit length which is given by

$$\int_0^{\pi} (p - p_0) r sin\theta d\theta \tag{5.38}$$

which equals

$$2r(p - p_0) \tag{5.39}$$

Thus we have

$$Th = r(p - p_0) \tag{5.40}$$

The tension T that develops is a property of the elastic wall as a reaction to stretch.
The force per unit area acting on the surface of the volume element is the stress (see figure 5.9):

$$\mathbf{F} = \mathbf{N} + \mathbf{H} \tag{5.41}$$

where **N** is the normal component such as a tension or a pressure, and **H** is the tangential component called the shearing stress.

In response to this stress the volume element undergoes a deformation called strain; so we have :

$$T = E\frac{r - r_0}{r_0} \tag{5.42}$$

being $r = r_0$ in the equilibrium position when the tension T is zero.

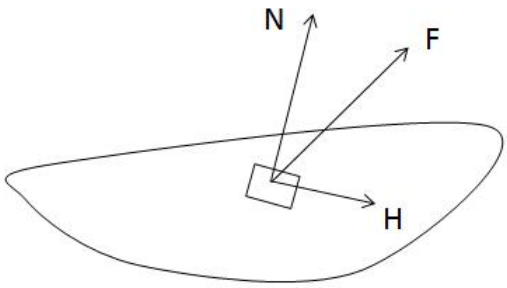

Figure 5.9: Stress component in an elastic membrane

Let us now consider the steady flow through an elastic pipe. A diagram of the structure is given in figure 5.10.

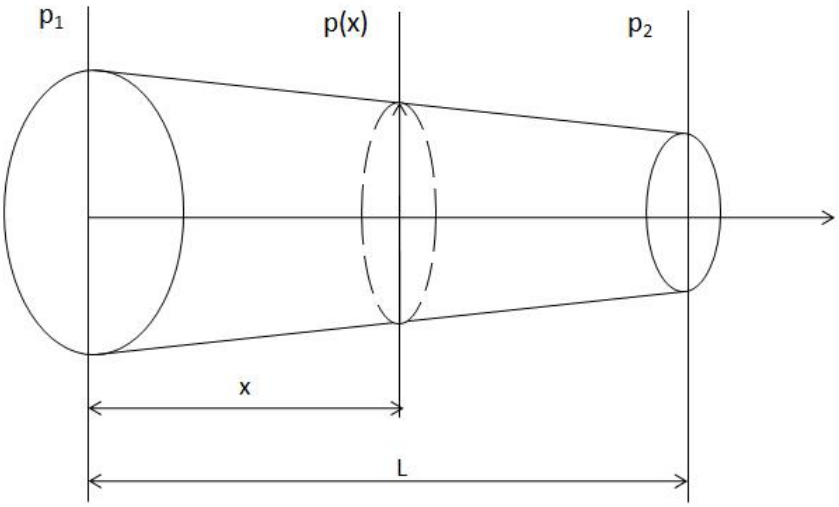

Figure 5.10: Flow through an elastic tube

It has been assumed that the tube has a length equal to L and the pressure is a function only of x and that

$$p(x)|_{x=0} = p_1 \quad and \quad p(x)|_{x=L} = p_2 \tag{5.43}$$

being p_1 and p_2 the inlet and outlet pressures, respectively.
The external pressure of the fluid surrounding the tube is assumed to have a constant value of p_0. We have from equation(5.40) that

$$p(x) - p_0 = \frac{Th}{r} \tag{5.44}$$

where r is the cross-sectional radius at location x. The pressure-radius relation is obtained from equations (5.42) and (5.44) giving:

$$p(x) - p_0 = \frac{Eh}{r}\frac{(r - r_0)}{r_0} = \frac{Eh}{r_0}\left(1 - \frac{r}{r_0}\right) \tag{5.45}$$

Calling the transmural pressure $p' = p - p_0$ and rearranging the equation (5.45), it is possible to obtain :

$$r = \frac{r_0}{(1 - \frac{r_o}{Eh}p'(x))} \tag{5.46}$$

Then the displacement U along the axis of the pipe is:

$$U(x) = r_0\left(\frac{r_0}{(1 - \frac{r_o}{Eh}p'(x))} - 1\right) \tag{5.47}$$

while the radial strain is:

$$\epsilon_r(x) = \frac{U}{r_0} = \left(\frac{r_0}{(1 - \frac{r_o}{Eh}p'(x))} - 1\right) \tag{5.48}$$

In this simulation it has been coupled a steady state flow simulation, made with Star CD, with an elastic pipe simulated in ABAQUS. The property of the fluid are the same described for the blood; a constant and uniform velocity inlet boundary condition was used ($v = 0.02$m/s); the outlet is placed to zero pressure that has been also considered as the reference pressure (p_0).

The finite volume mesh and the geometry is the same used in the validation showed in the previous chapter ($r_0 = 0.01025$ m and $L = 0.2$ m).

In ABAQUS we modeled a pipe of internal radius equal to r_0 and a thickness $h = 0.00195$ m, with a Young modulus $E = 3$ MPa. The mesh has linear hexahedral elements. The axis of the cylinder is the Z axis; the only degrees of freedom at the inlet and outlet bounds are the displacements in the X-Y plane.

In the chapter dedicate to the aorta model we'll go in deep in the definition of the method used in order to do the coupling. Briefly, the pressure resulting from the fluid simulation is mapped on the internal

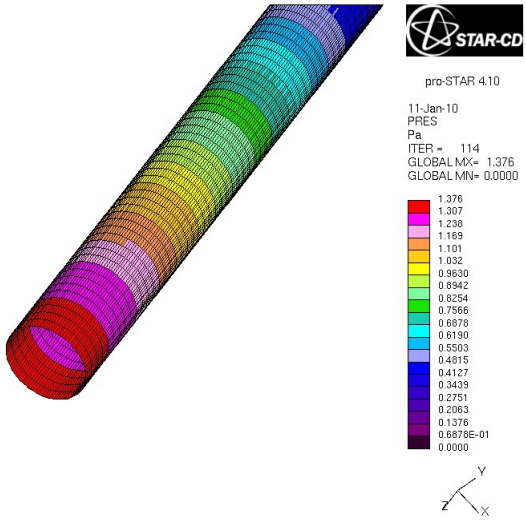

Figure 5.11: Pressure mapped on the internal surface of the pipe. Note that the mesh is the ABAQUS hexahedral element based mesh

surface of the solid pipe. In figure 5.11 is possible to appreciate the pressure computed with the CFD code mapped on the mesh used in ABAQUS for solving the solid mechanics problem (note the difference with the results showed in 5.12).

Even when the flow is not completely developed, the pressure profile along the axis of the pipe (see figure 5.13) is quite linear. Also the profile of the strain ϵ_r along the same axis is linear (see figure (5.14)) and is equivalent to the theoretical results (equation (5.48)); particularly:

$$p(L) = 1.37Pa \Rightarrow \epsilon_r(x) = \frac{U}{r_0} = \left(\frac{r_0}{(1 - \frac{r_o}{Eh} p'(L))} - 1 \right) = 2.4 \cdot 10^{-6} \tag{5.49}$$

In figure 5.15 the displacement magnitude on the deformed shape of the pipe is mapped.

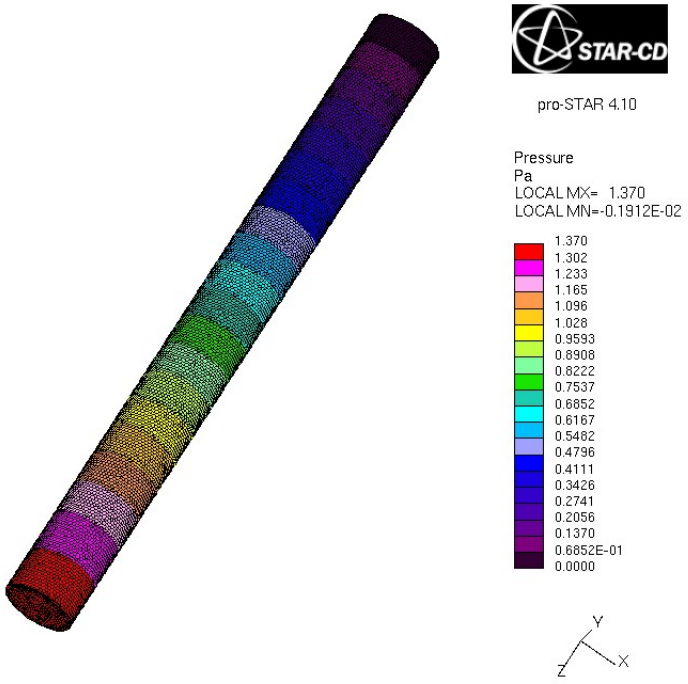

Figure 5.12: Pressure in the fluid domain inside the pipe. Note the polyhedral mesh of Star CD

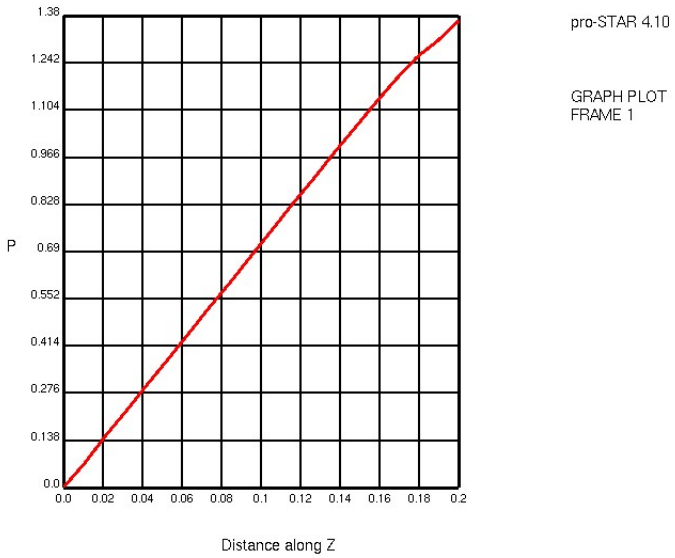

Figure 5.13: Pressure [Pa] along the pipe axis. The inlet is the section Z=0.2 m

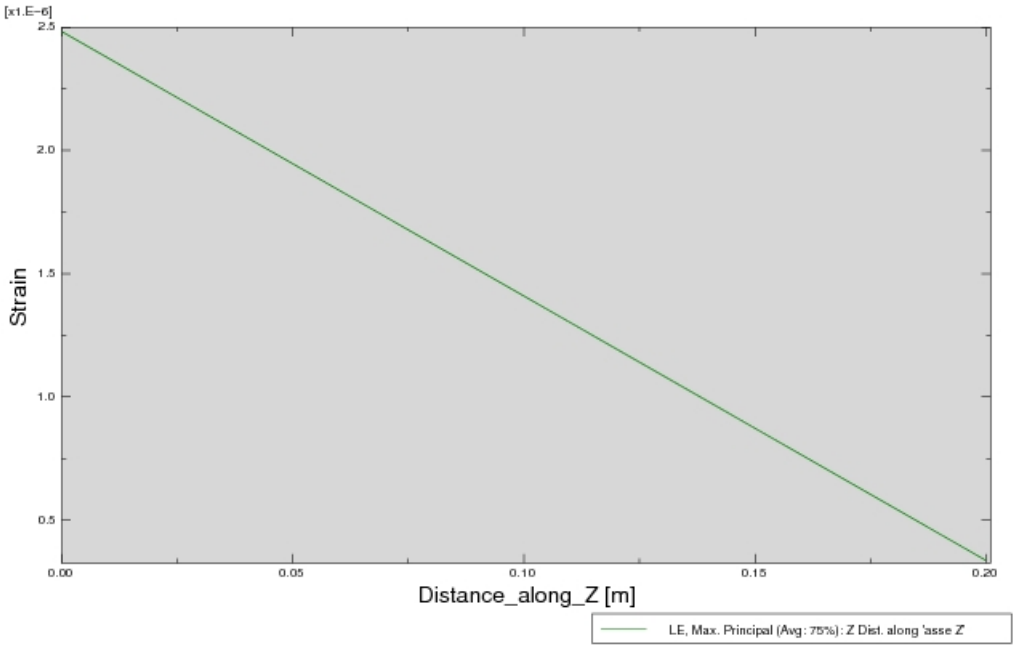

Figure 5.14: The radial strain ϵ_r along the Z axis.

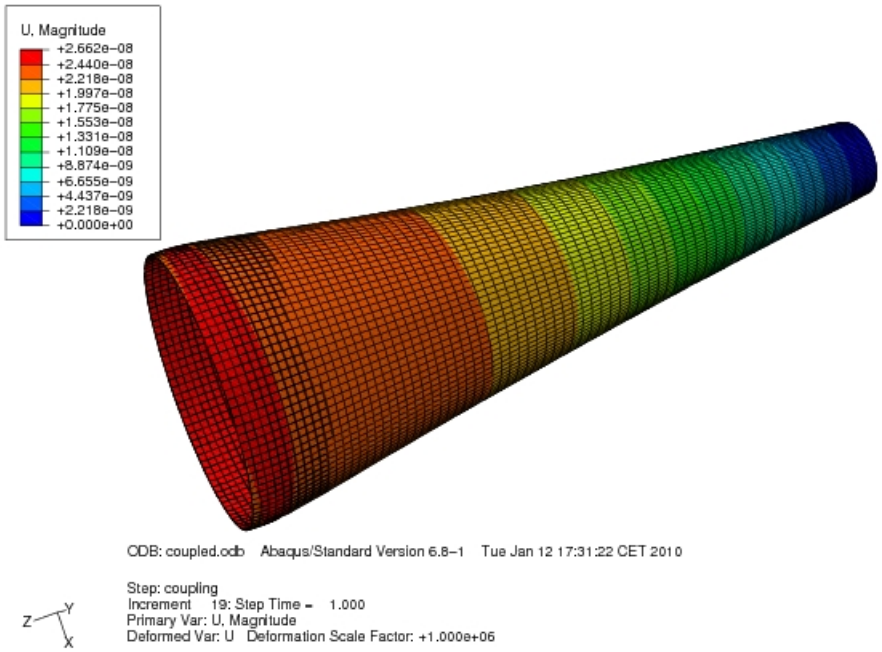

Figure 5.15: The displacement U mapped on the deformed pipe (The scale factor of the deformation is 10^6).

Chapter 6

The aortic model

In this chapter the main fluid dynamics and biomechanical features of two different models of ascending aorta will be compared. The aim is to understand the influence of the bicuspid aortic valve pathology (BAV), that is present in a patient since birth, on the further occurrence of aneurysm in this stretch of the aorta.

For this reason the geometry of the two models are the same in both cases and the dimensions are referred to an idealized aortic arch of an adolescent patient, in which the upstream conditions (the physiological or pathological morphology of the valve) determine the downstream condition (that are the boundary conditions of the models).

6.1 The aortic blood flow model

As it was previously declared, the geometry used in the simulations is the same for both models. In figure 6.1 the geometry used in ABAQUS in order to simulate the mechanical behavior of the ascending aorta during a cardiac cycle is shown.
In figure 6.1 it is possible to appreciate the dimensions of the model [19]. The fluid part correspond to the inner of this model.
The internal radius of the aortic arch is constant along the model from the inlet to the outlet, and is equal to $r = 10.195$ mm; the radius of revolution of the toroid that represents the aortic arch is equal to $R = 36.995$ mm. The radius of the brachial-cephalic artery, the left common artery and the left subclavian artery are equal to 4 mm, 3 mm and 3.5 mm, respectively.

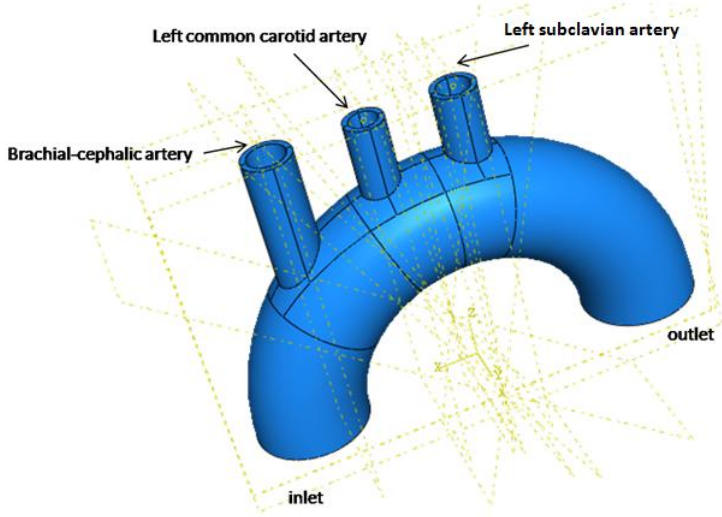

Figure 6.1: Geometry of the ascending aorta model

6.1.1 Fluid geometry and mesh

The geometry of the model has been made in ABAQUS; it is a simplified geometry of the ascending aorta formed by a toroid and three cylinders. The geometry has been imported in pro-surf Star CD as a `.igs` file; here a triangular surface mesh has been created and exported as a `.dbs` file.

Starting from this surface mesh, the volume mesh (`.ccmg` file) has been created in pro-amm Star CD. The polyhedral cells were chosen to discretize the domain.
CD-adapco's polyhedral meshes typically consist of cells of 12 and 14 faces (although the number of faces is unrestricted). This means that they fill space in close to the most efficient way possible. For a given resolution level, a mesh consisting of CD-adapco's polyhedral cells has fewer faces than a mesh of any other cell type.

Apart from the obvious benefits of economy, polyhedral meshes provide other advantages too. Because each polyhedral cell has more faces, it also has more neighbors than traditional cell types. A tetrahedral cell communicates with only four neighbor cells, and a hexahedral just six. In both cases this limits the influence of each cell to just a few neighbors. By contrast each polyhedral cell has an average of 12 or 14 neighbors.

The net result of this is that information propagates much more quickly through a polyhedral mesh, ultimately leading to an increased rate of convergence.

In the same way that a polyhedral cell "speaks" to more of its neighbors than other cell types, it also "listens" to the information from more of them. Because each polyhedral cell receives information from more of its surroundings, the cell centered values calculated for the cell are more accurate than for other types.

The average size of the polyhedral cells used was 1 mm; considering that a time step of 0.01 s has been used for all the simulations, this mesh resolution ensures that the Courant number satisfies the cell-wise and the globally criterion[1]. Also if a laminar flow has been simulated, the mesh has been made considering the possibility to simulate a turbulent flow too; two layers of polyhedral cells parallel to the wall of the model [12] have been created; the thickness chosen is 0.5 mm for each layer (see figure 6.2). In this way the domain is composed by 65539 cells and a total of 304067 vertex.

[1]The Courant number is defined as $Co = \frac{|\vec{v}|\cdot\Delta t}{l}$
Cell-wise : setting $|\vec{v}|$ to an estimated local velocity and l to the corresponding local mesh dimension (e.g. cell diagonal). The Courant number does not exceed 100. Globally: setting $|\vec{v}|$ to the estimated average velocity in the flow field and l to a characteristic overall dimension of the model. The time step should be chosen so that it is commensurate with the time scale of the physical process being modeled. Courant number derived from this criterion is typically in the range 100 to 500.

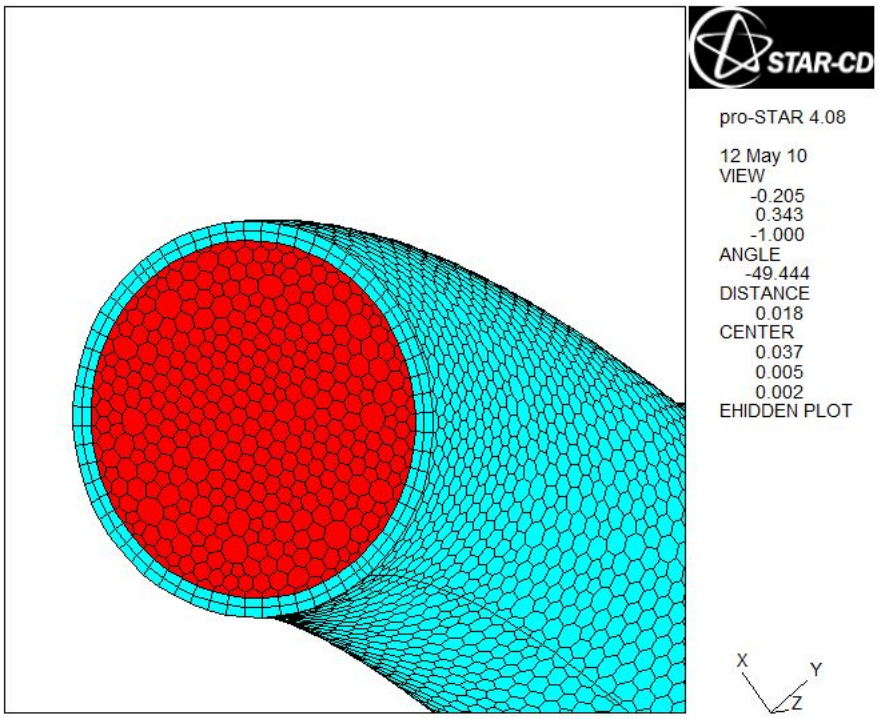

Figure 6.2: Fluid mesh at the inlet of the aortic arch. Note the layers parallel to the wall boundary

6.1.2 Boundary conditions

Three cardiac cycles have been simulated but only the last one has been analyzed; this was made in order to take on the transient effects. Each cardiac cycle takes 0.96 s ($\simeq$ 60 beats for minute). For the physiologic and the BAV models a pressure condition has been chosen for the brachial-cephalic artery, the left common carotid artery, the left subclavian artery and the outlet section (fig 6.1) that represents the beginning of the descending aorta.

The value of the pressure during the cardiac cycle is shown in figure 6.3. Here it can be noted that the minimum pressure is zero; indeed from the physiological pressure, derived from the literature [22], the diastolic pressure was subtracted, so that the resulting pressure is relative to the diastolic one.
This is because the geometry of the model was created considering the

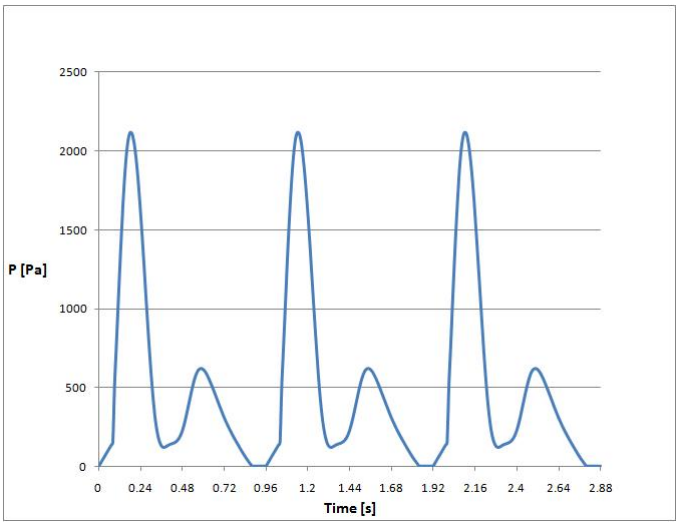

Figure 6.3: Pressure versus time during the three cardiac cycle used as boundary condition

dimensions in the diastolic part of the cardiac cycle, that is when the internal pressure is 80 mmHg and the mass inlet is zero (aortic valve closed).
This boundary condition has been implemented in Star CD through the subroutine $BCDEFP$ (see appendix B) allowing the pressure value to change every time step and assuming a uniform distribution on the reference sections.

Now let us discuss the inlet condition. The velocity inlet condition is chosen for the section that represent the region located 3-4 cm downstream of the aortic valve. The influence of the BAV condition on the flux profile downstream the aorta valve was already discussed in the chapter 2.

The purpose of going to investigate the differences of the flow field and mainly of the wall shear stress (WSS) between the physiological case (normal valve) and the pathological one (BAV) is achieved by placing appropriate inlet velocity boundary conditions.
For the physiological inlet condition we take as a reference the work of Suo [49]. In figure 6.4 the blood flow at various section of the ascending aorta during a cardiac cycle is shown.

Rearranging the information provided by the curve of the inlet flow (the violet curve), using our geometrical dimension, we obtain the time

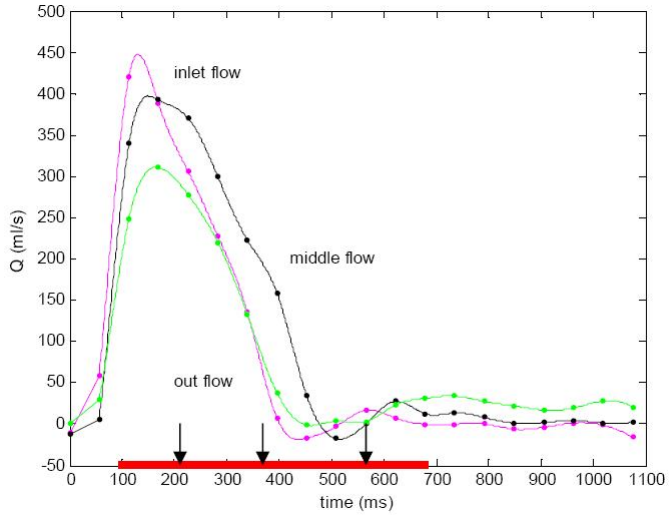

Figure 6.4: Flow inside the ascending aorta at different section during a cardiac cycle (Suo et all.)

trend of the average velocity inlet ($\bar{v}$) on the inlet section, that is shown in figure 6.5 for three cardiac cycles.

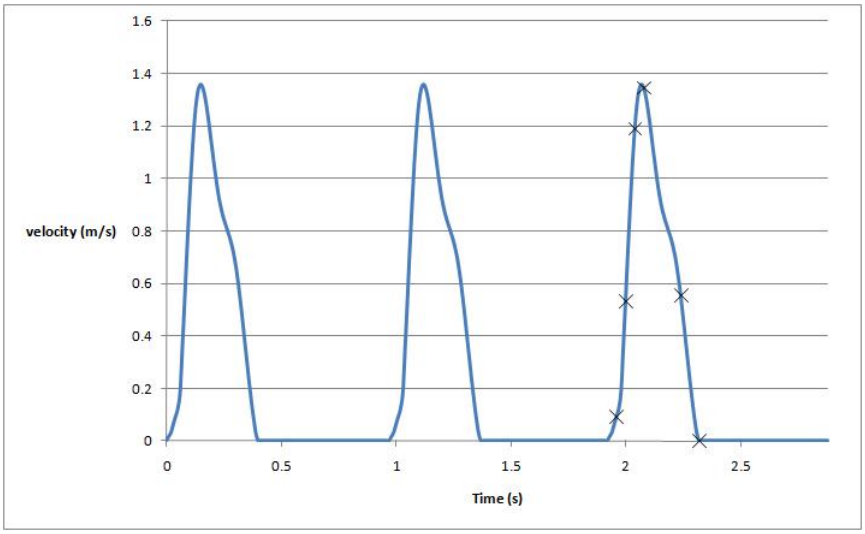

Figure 6.5: Average velocity at the inlet section $\bar{v}$ during three cardiac cycles of the simulation

The boundary condition used in the simulation of the physiological case is then a velocity that have a parabolic profile on the inlet section and is zero on the inlet border line. In each time step the value of average velocity is given by the curve of the figure 6.5. This spacial profile and time trend is implemented in the subroutine $BCDEFI$ (see appendix C).

Keeping the same volume flow rate, for the BAV model an eccentric and asymmetric profile of the velocity inlet has been assumed according with Robicsek [45]. We refer to the BAV morphology of the figure 2.1 with a maximum of the velocity profile changing its position along the left-right axis during the cardiac cycle. The implementation of this profile is discussed in appendix D.
In figure 6.6 it is shown the velocity profiles at several values of time (1.92 s, 1.96 s, 2 s, 2.04 s, 2.08 s, 2.16 s, 2.24 s, 2.32 s). On the left column the normal parabolic profiles is reported while on the right one the BAV velocity inlet profiles during the systole are shown.

Time=1.92 s

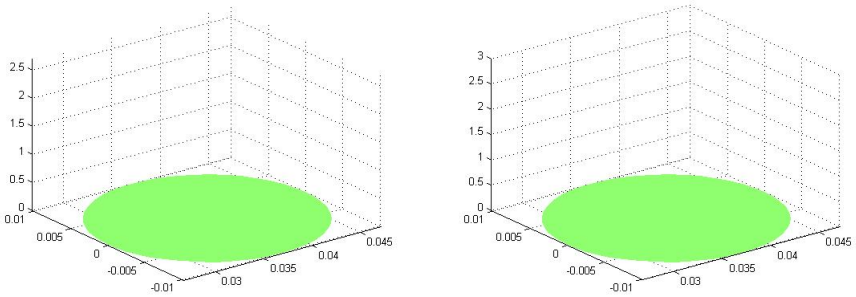

Time=1.96 s

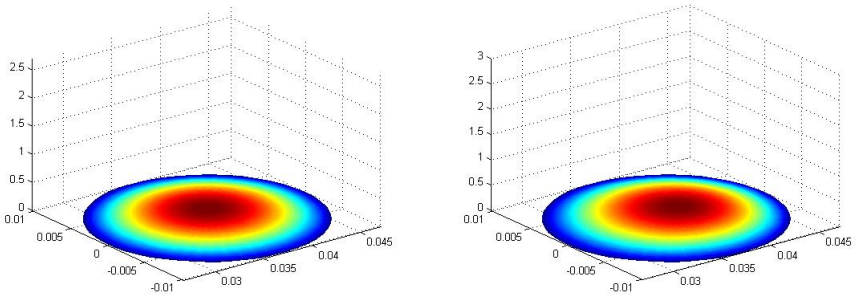

Time=2.04 s

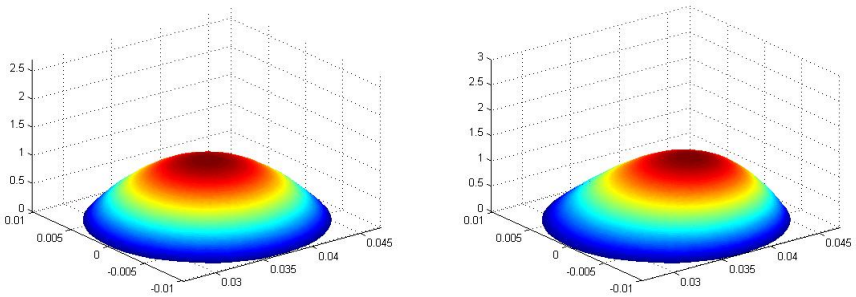

Time=2.08 s

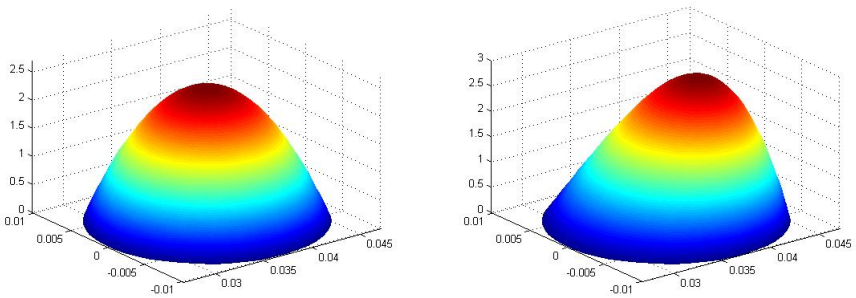

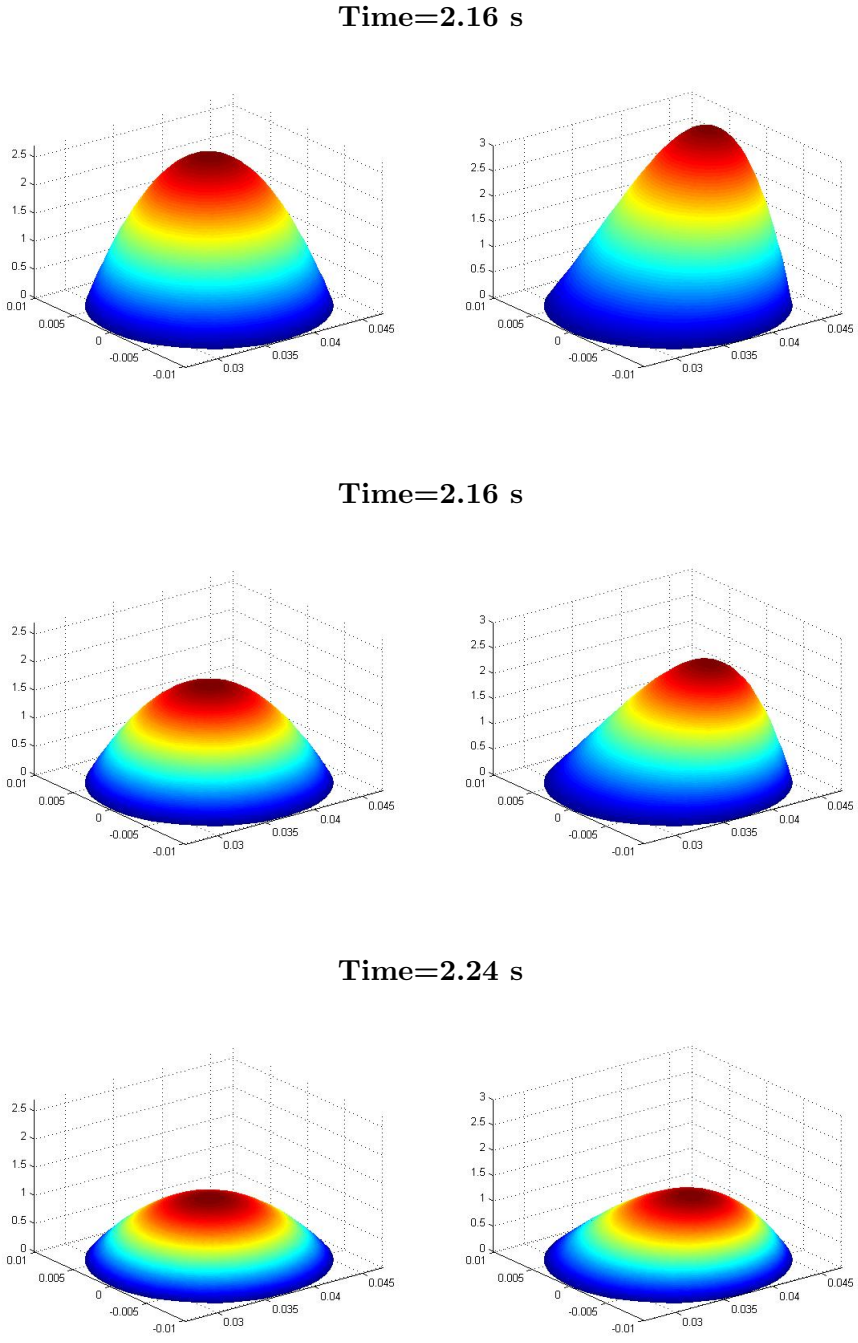

Figure 6.6: Parabolic (left column) and BAV (right column) velocity inlet profile at the time istant 1.92 **s,** 1.96 **s,** 2 **s,** 2.04 **s,** 2.08 **s,** 2.16 **s,** 2.24 **s,** 2.32 **s**

6.1.3 Results

The results showed from here to the end of the chapter are selected at the instants of time corresponding to the black cross marked in figure 6.5: early systole (t = 1.96 s and t=2 s), peak systole (t=2.04 s and t=2.08 s), late systole-early diastole (t=2.24 s and t=2.32 s);
All the following results are referred to these six instants unless otherwise stated.

Time=1.96 s

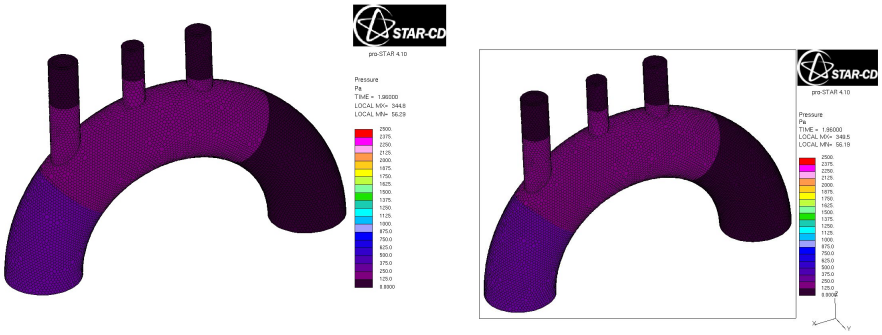

Time=2 s

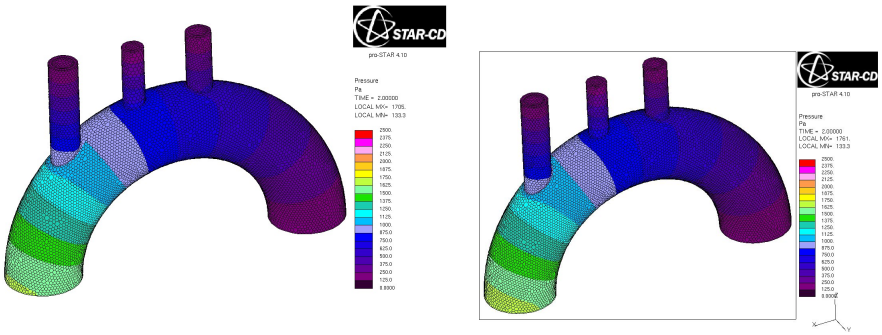

Time=2.04 s

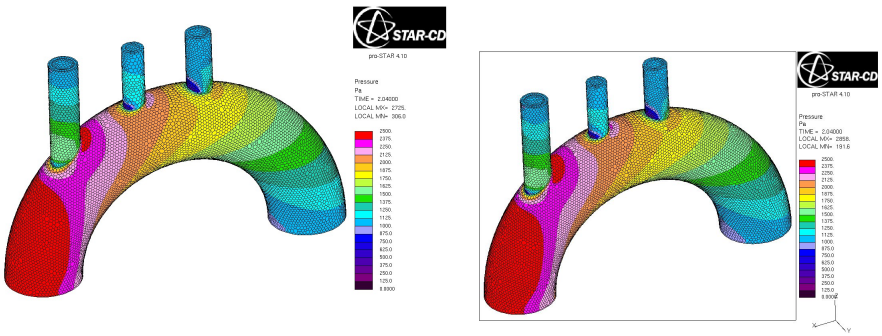

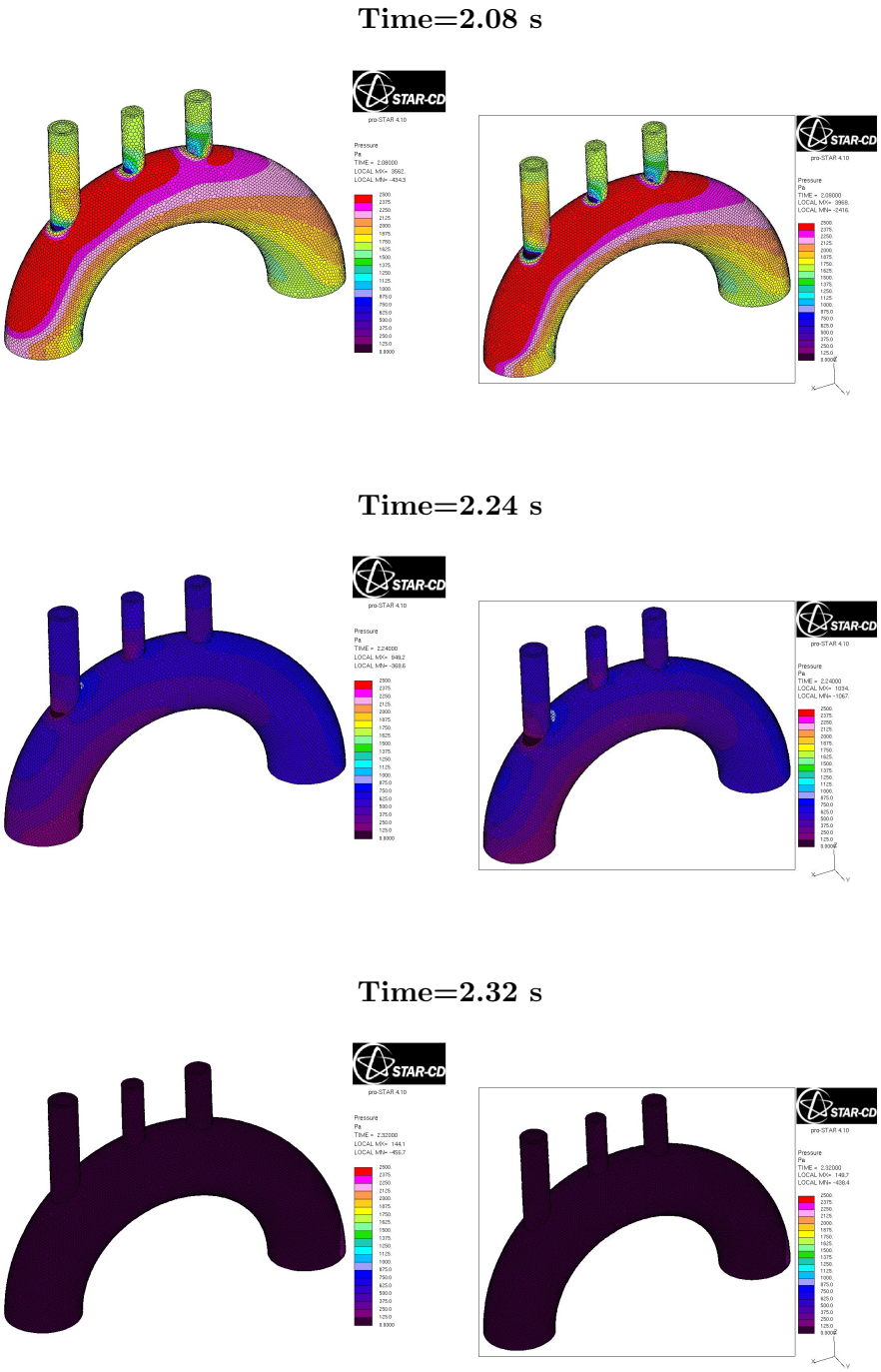

Figure 6.7: Wall pressure for the physiologic (left column) and BAV (right column) models

Pressure and velocity profiles

In figure 6.7 the pressure at the wall of the aortic arch is showed for the the physiological model (left column) and the BAV model (right column); the profiles are very similar, proving the low influence of the velocity profile at the inlet section on the pressure distribution.

Time=1.96 s

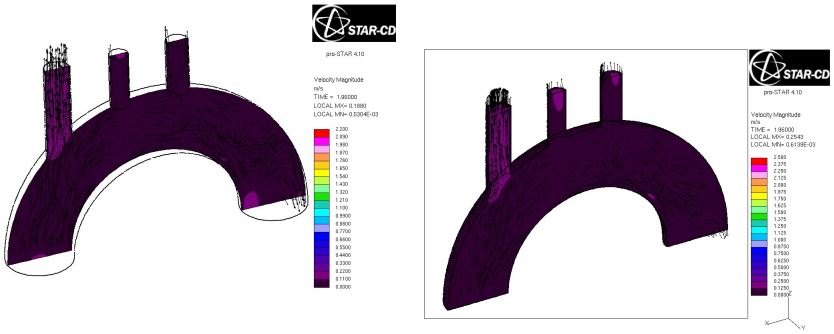

Time=2 s

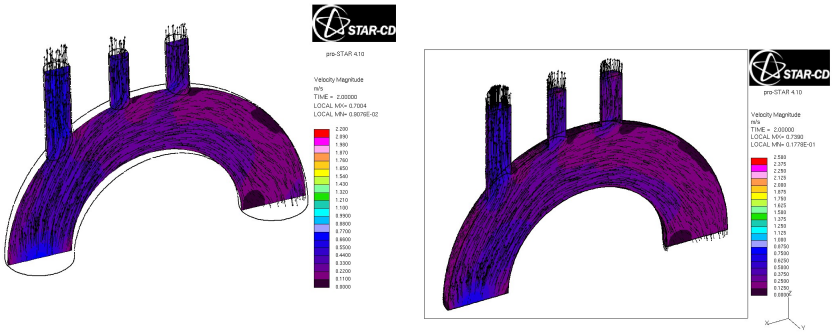

Time=2.04 s

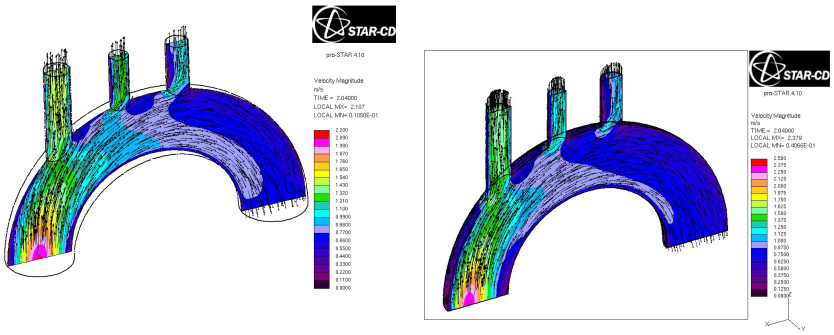

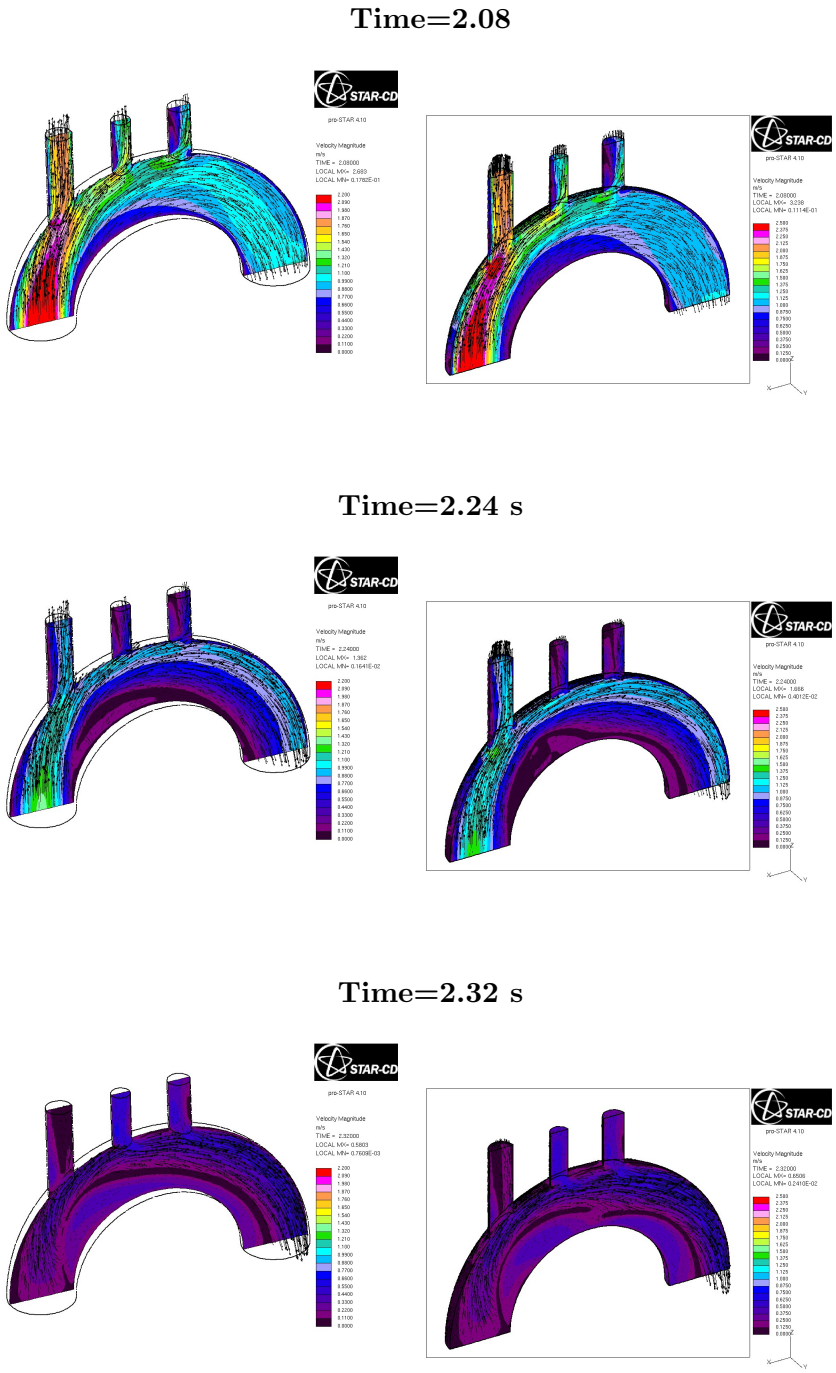

Figure 6.8: Velocity magnitude and vector on the plane X-Z for the physiologic (left column) and BAV (right column) models

During the cardiac cycle simulation the pressure rise from a quite zero pressure to a maximum of about 5350 Pa (approximately equal to 40 mmHg) . This values have to be considered as a relative pressure;

80 mmHg must be added to compare the value with the classical aortic pressure trend. Almost the same can be said with regard to the velocity profile showed in the figure 6.8. All the figures have been captured in Star CD using the macro described in the appendix E.

In the figure 6.10 the secondary flow of the physiological model is showed; the section used is the one created by the intersection of the aortic arch with X-Y plane roted by 15 degree respect to the Y axis (figure 6.9).

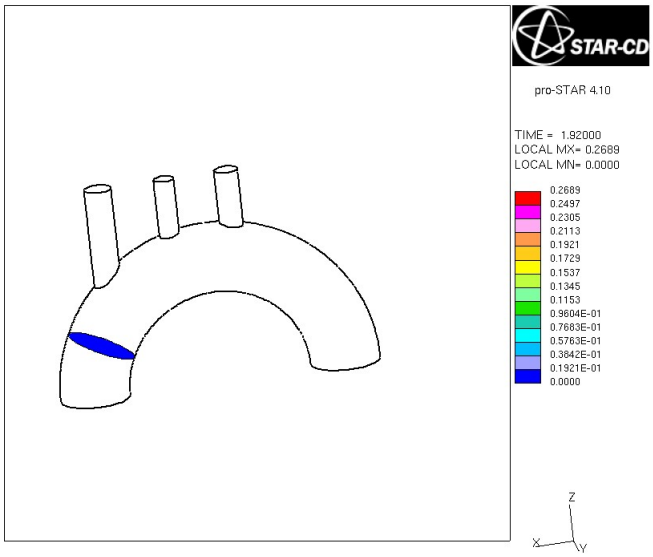

Figure 6.9: Section of the model

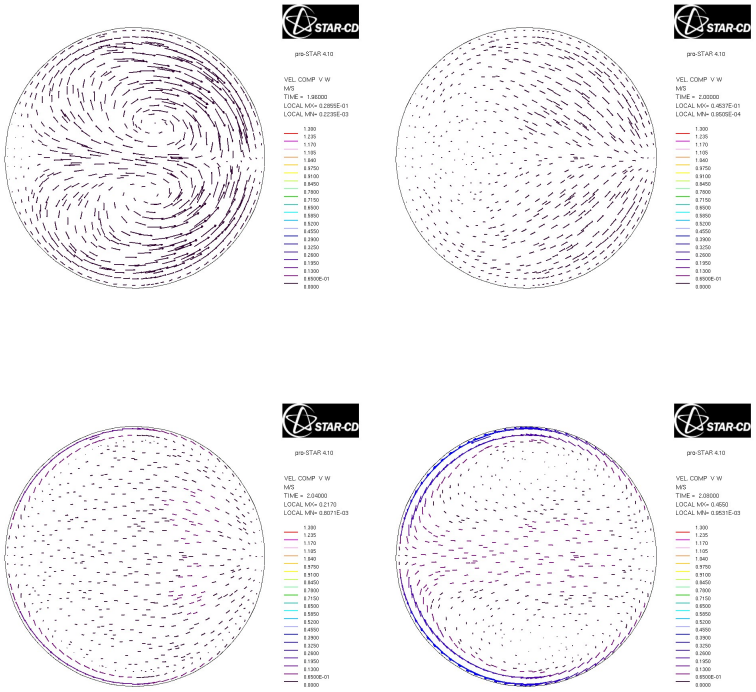

Figure 6.10: Secondary flow in the section of figure 6.9 for the physiologic model at the time (from left to the right and from top to the bottom) 1.96 **s,** 2 **s,** 2.04 **s,** 2.08 **s**

The wall shear stress

In figures 6.11 and 6.12 the module and the vectorial representation of the shear stress at the wall of the models are shown, respectively .

Time=1.96 s

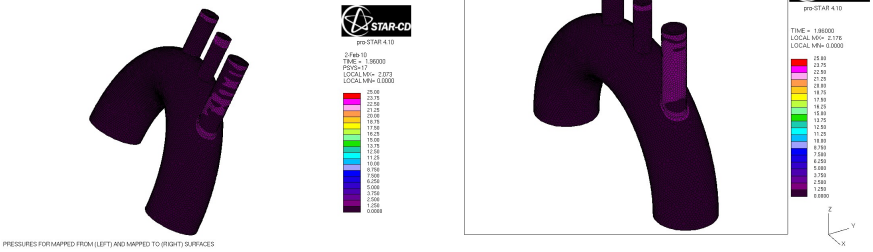

Time=2 s

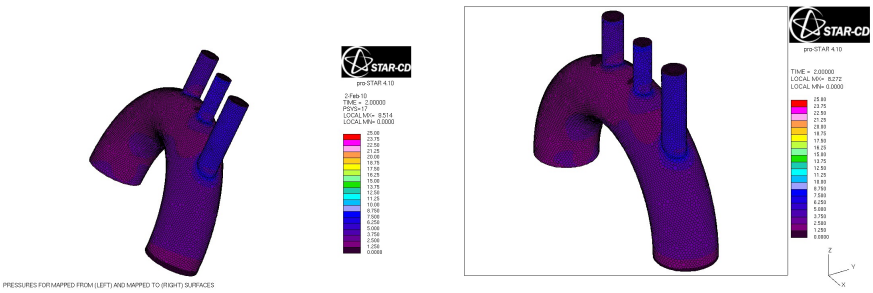

Time=2.04 s

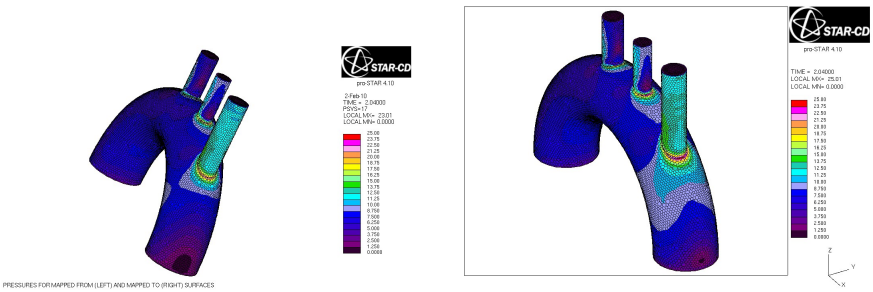

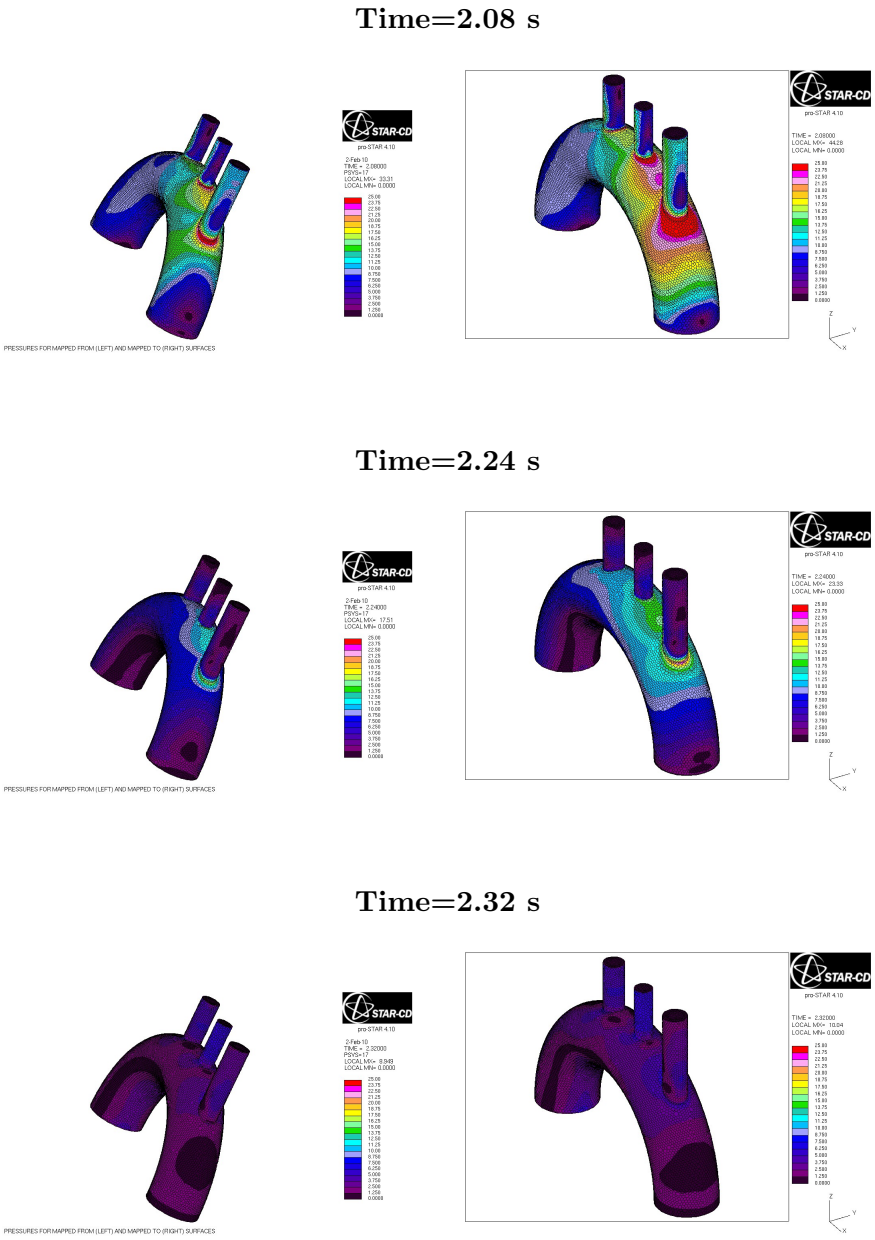

Figure 6.11: Wall shear stress magnitude for the physiologic (left column) and BAV (right column) models

Star CD have the capability to calculate the component of wall shear force. The definition given in the user's guide [2] is used to calculate the WSS :

$$F_s = \tau_w A_b \frac{v_{pa} r}{|v_{par}|}$$

where A_b is the wall cell face area, v_{par} is the velocity vector component

parallel to the wall at the center of a near-wall cell.

Time=1.96 s

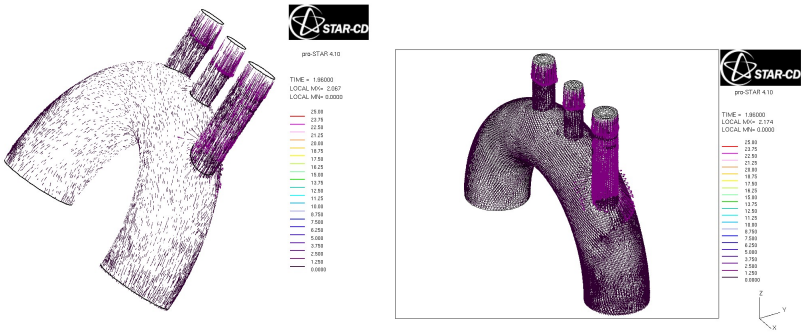

Time=2 s

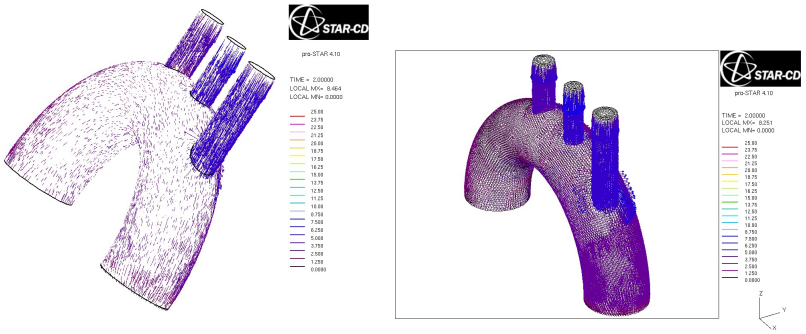

Time=2.04 s

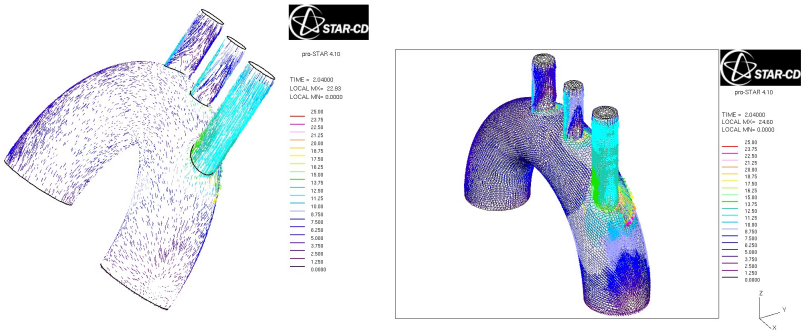

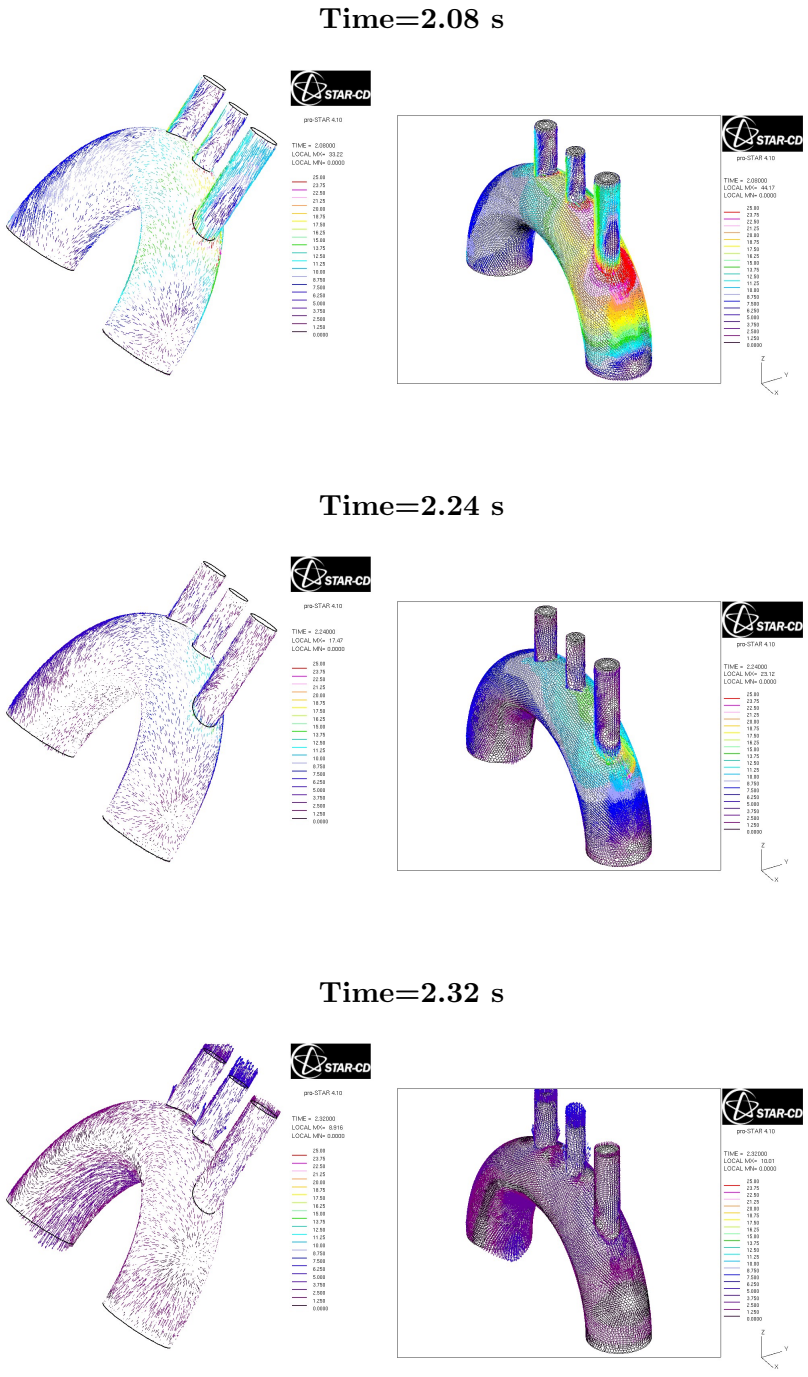

Figure 6.12: Vectorial representation of the wall shear stress components for the physiologic (left column) and BAV (right column) models

In order to compare in a more quantitative way the results of WSS for the physiological and BAV models, the figures and graphs in 6.13 were created (see appendix E).

In the left column the percent difference between the wss of the BAV and the physiological model is shown at different instant of the cardiac cycle. In the right column we have the wss values for the two different models along the perimeter of the section of figure 6.9.

Time=1.96 s

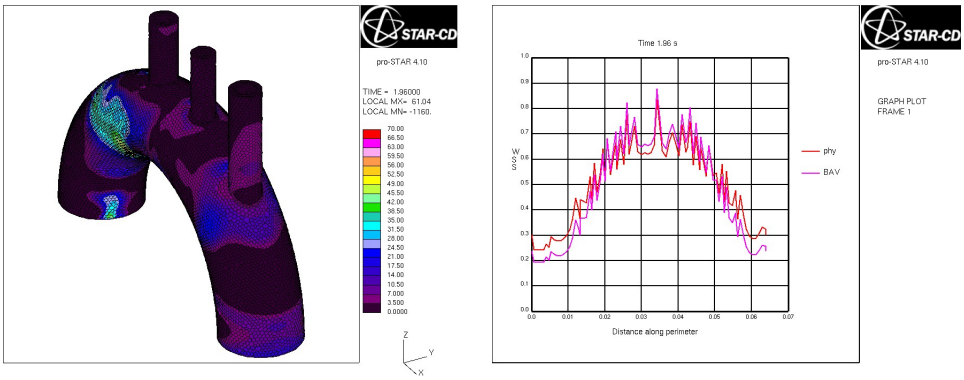

Time=2 s

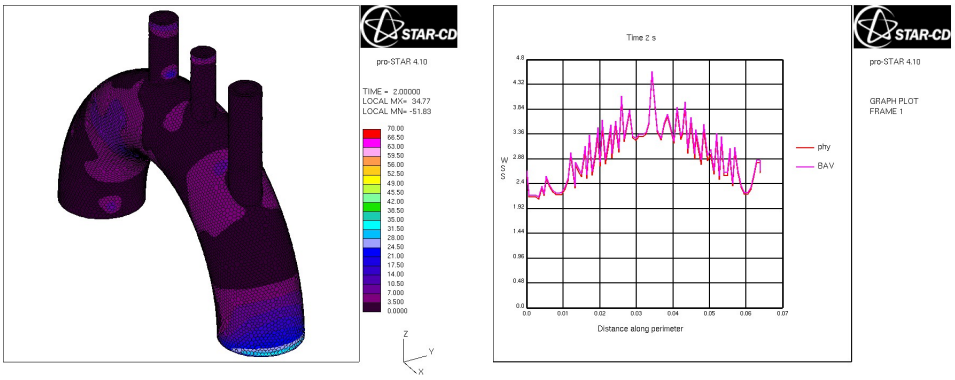

Time=2.04 s

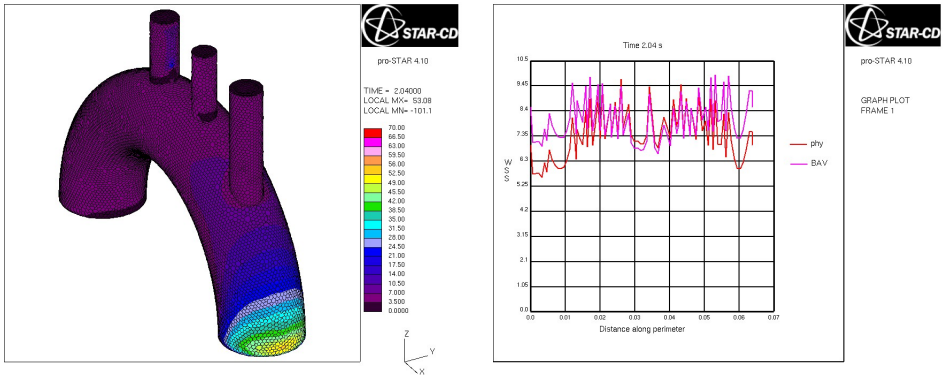

Time=2.08 s

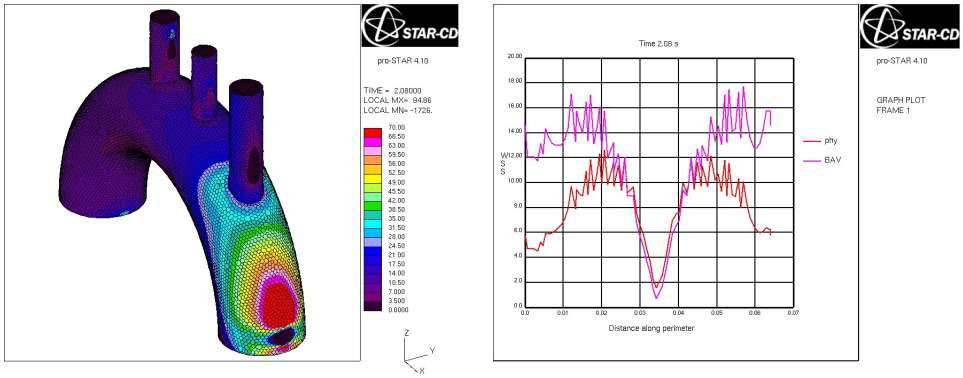

Time=2.24 s

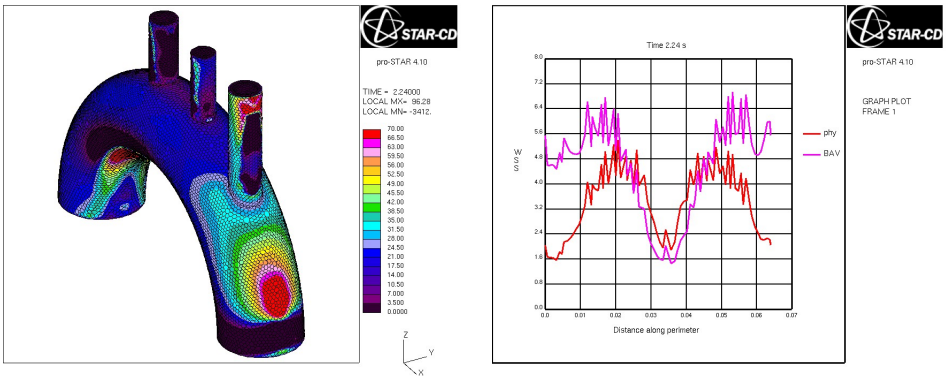

Time=2.32 s

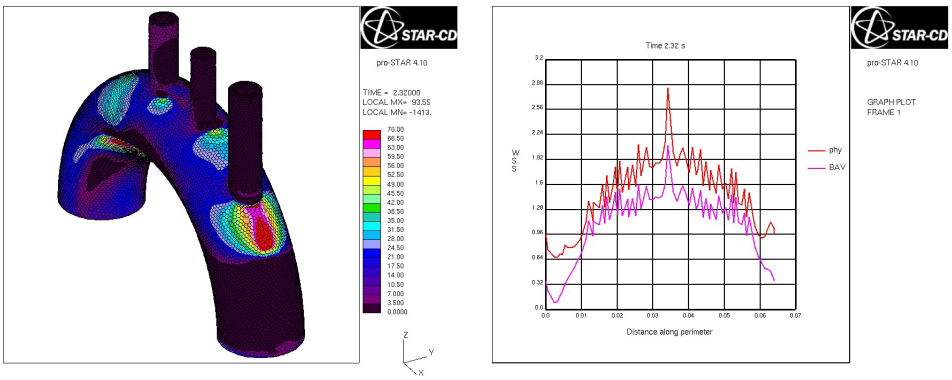

Figure 6.13: On the left the percent difference of wss magnitude between the BAV and the physiological model. On the right BAV wss (violet curve) and physiological wss (red curve) along the perimeter of the section 6.9

These graphs confirm that the major difference regard the extrados area.
During the first part of the systole the wall shear stress present higher values in the intrados area (central part of the right graphs); this distribution changes during the late systole when the wss magnitude becomes generally to lower values.
It is possible to appreciate that the wss in the BAV model is generally higher than the wss of the physiological model.

This is valid especially in the extrados area of the ascending aortic arch (extremes of the right graphs) where in normal condition (physiological red curve) the magnitude of the wss oscillates between 0.3 Pa·s and 5.5 Pa·s and the differences between the two models can be also higher then the 70%; furthermore this area during the cardiac cycle moves from the inlet to the brachial-cephalic artery in a cyclic way.
This is a very interesting result because this area is one of the most common parts for the development of aneurysm.

6.2 Coupling with the aortic wall

In order to have a complete view of the differences between the physiologic and pathologic case, the results of the fluid domain has been coupled with the solid domain representing the wall of the aortic artery.
Before to explain the method used to couple the fluid and the structure domain, the mesh and geometry make in ABAQUS will be discussed.

The geometry of the model was extruded from the surface of the fluid domain; the thickness of the wall's arteries is constant and equal to 1.95 mm.

The mesh is composed by 32121 linear hexahedral hybrid elements (figure 6.16); meshing the model, the geometry has been partitioned by using several planes (see figure 6.14), allowing to mesh some regions of the model with a structured technique and some other with a sweep (mapped) one (figure 6.15); the thickness of the model was seeded creating three parallel layers of elements.

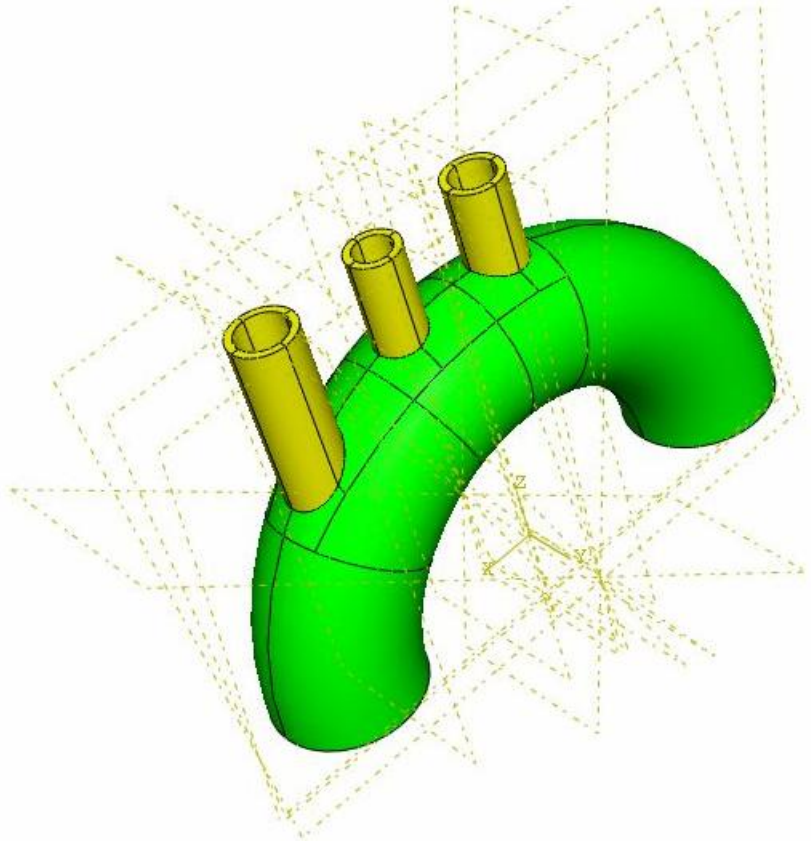

Figure 6.14: The wall model partitioned by using several planes

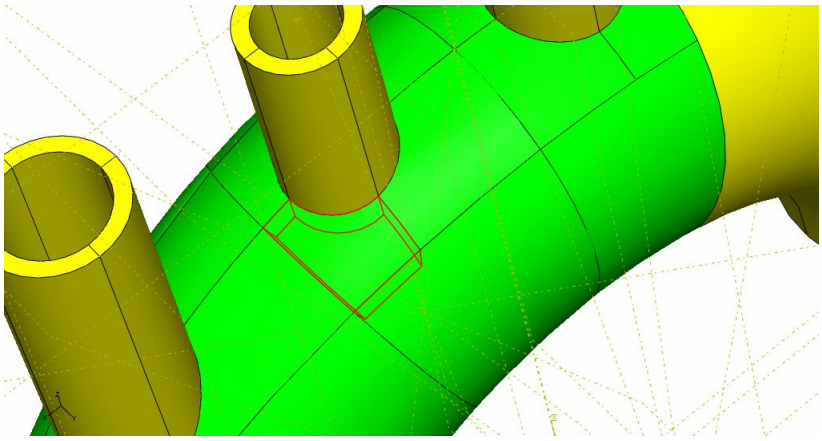

Figure 6.15: Different kinds of region meshes; the green regions are meshed by using a structured technique while the yellow regions are meshed by using a sweep technique

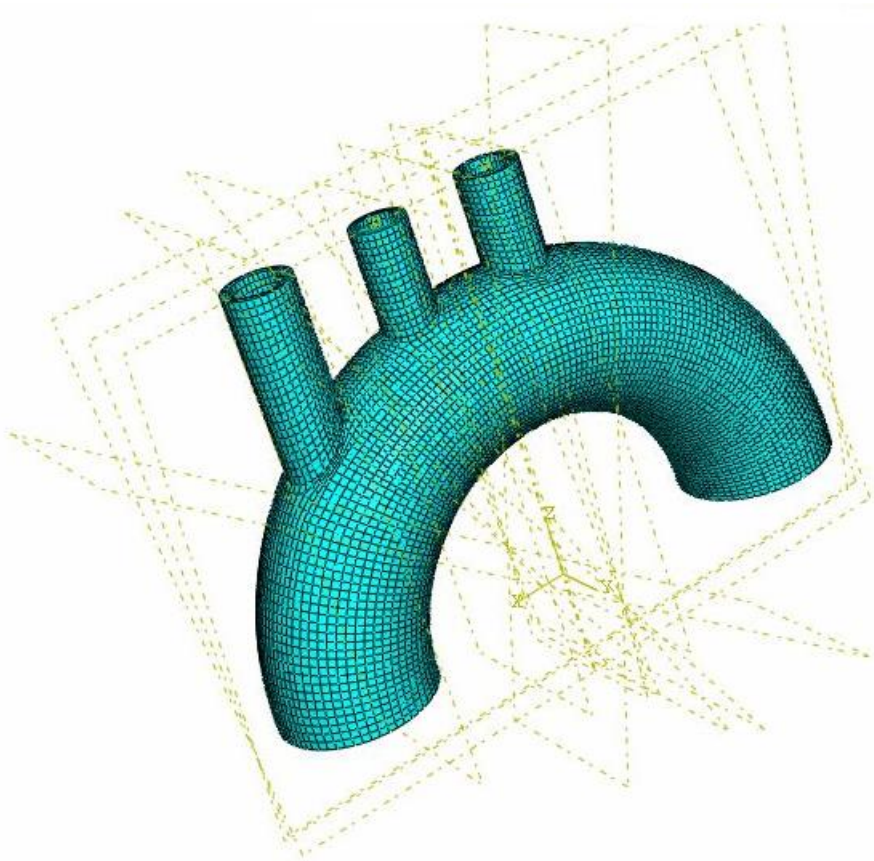

Figure 6.16: Final mesh of the solid domain

When the mesh is created in ABAQUS and an input file (`.inp`) of the model is ready, Star CD is able to import the solid mesh through this file; the figure 6.17 shows the result of this operation. Note that the inner (orange colored) has a polyhedral mesh while the wall has a hexahedral mesh coming from ABAQUS (green colored).

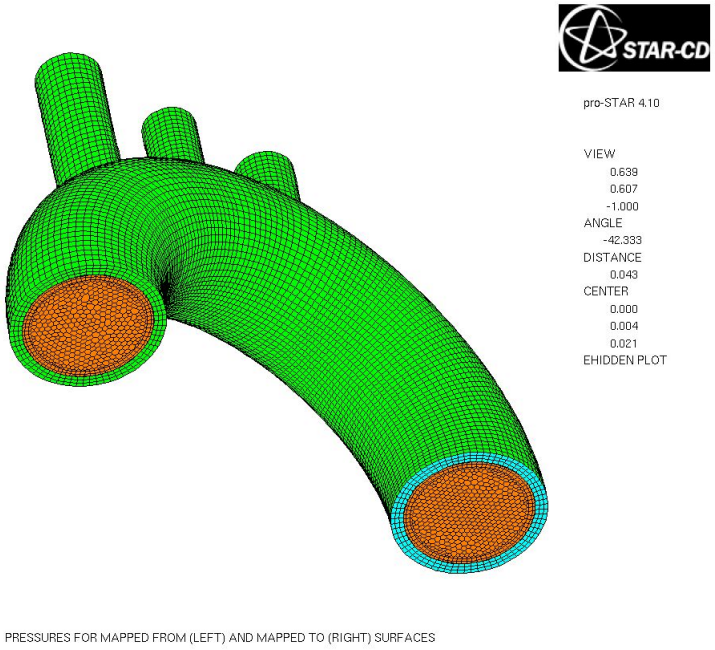

Figure 6.17: The solid mesh imported by ABAQUS in Star CD

Furthermore Star CD is able to map the pressure resulting from the simulations discussed in the section 6.1 on the solid mesh already imported. In figure 6.18 it is possible to see an example of this operation. This is done by creating a `.mapd` file (see appendix F) containing the value of the load applied on the element of the coupling surface.

We decided to map the pressure results for both the physiological model and the BAV model every four time steps (0.04 s) starting from the beginning of the third cardiac cycle of the previous fluid dynamic simulations.

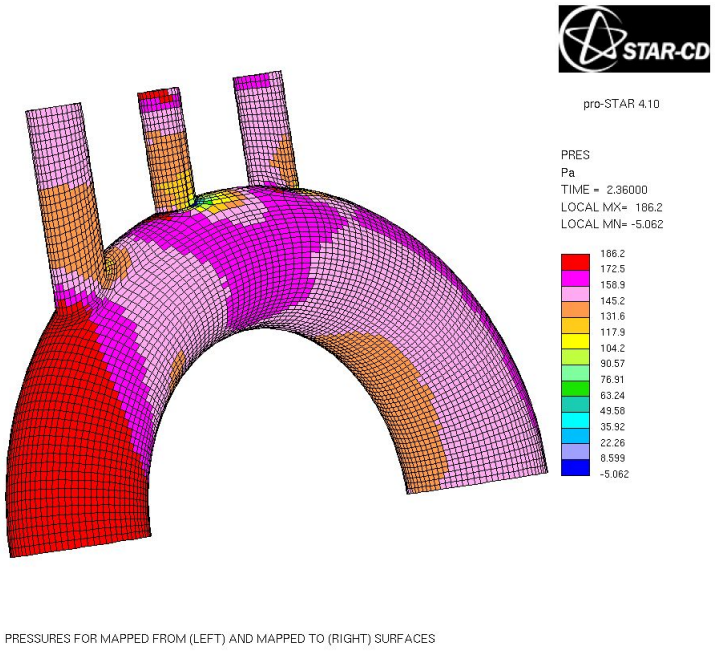

Figure 6.18: Field of pressure mapped on the surface's elements of the arterial wall model

6.2.1 The solid model

From the early days after applying FEM in researches and investigations, in order to achieve the best model of the arterial system, the issue of the best boundary conditions arise and until today is being discussed in researches and articles [18] [32] [7] . Specifically for the inlet section of our model different conditions have been developed, considering this is the nearest to the hearth.

Some authors suggest to impose a periodic rotation to the plane of the inlet section and an axial displacement too. In our case (many steps, loads changing step by step) we decided to apply a simple encastre to this section in order to minimize the computational costs and to ensure convergence of the numerical simulation.This allows us to still be able to compare the results of the two models in a completely satisfactory way. For the other sections (the outlet sections of the descending aorta, the brachial-cephalic, the left common carotid and the subclavian arteries) an in-plane displacement boundary condition is applied: nodes can move only in X-Y plane. It means that the nodes will remain in their initial

plane during the entire simulation.
This is an option which ABAQUS offers by its distributing force boundary condition, the: distributing coupling [1]. It constrains the motion of the coupling nodes to the rigid body motion of the reference node, which in our case is the central point of boundary sections.

The dimensions of the model are taken from works [19] in which the geometrical informations are given by using angiographic or TAC techniques. These are *in vivo* imaging techniques and for this reason the dimensions are obtained at particular values of pressure, normally the diastolic pressure (at least in the following discussion this will be supposed).
Then the geometry used is referred to a situation in which the internal pressure is 80 mmHg. If we consider that the pressure mapped from the fluid simulations are lacking the diastolic pressure (see the boundary conditions of the model) we have the needs to achieve the equilibrium of the initial geometry with the initial load (the diastolic pressure for this case); so the evaluation of the initial stress field in the model is required.

The importance of the initial stress condition can be appreciate just looking the graph of figure 6.19. If we use a zero-stress initial condition the geometry deforms excessively (ΔD_A). This is because of the low stiffness of the material at low level of load (pressure in this case); the deformation is realistic working at different operating point of the curve; for our work we can imagine that the pressure P_A represent the diastolic pressure while the pressure P_B the systolic one.

In order to take into account the diastolic pressure the values of stresses have been calculated using the small thickness theory applied to the aortic arch and the efferent arteries; moreover these stress field applied should lead to little displacement of the model. This condition is realized introducing an initial first step in which only the initial load (diastolic pressure of 80 mmHg equal to 10665 Pa) is applied balancing the initial conditions of stress field.

Using this method, the circumferential stress of 27.8 kPa has been

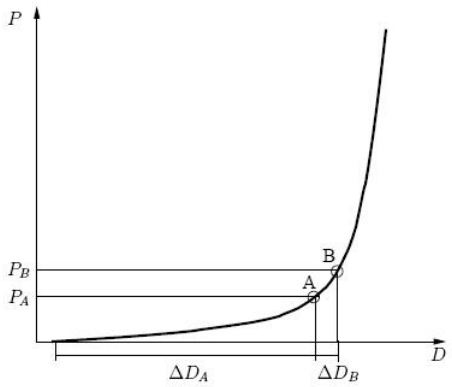

Figure 6.19: schematic representation of the curve diameter-pressure

applied to the aortic arch, and 21.8 kPa, 16.4 kPa, 19.1 kPa respectively to the brachial-cephalic, common carotid, subclavian arteries; also a longitudinal stress, equal to the half of the circumferential one, has been applied for each part.
In the figure 6.20 the results of the balancing step of the simulation is shown. It is possibile to note that the initial displacements obtained are small and the mesh is quite superposed on the original one.

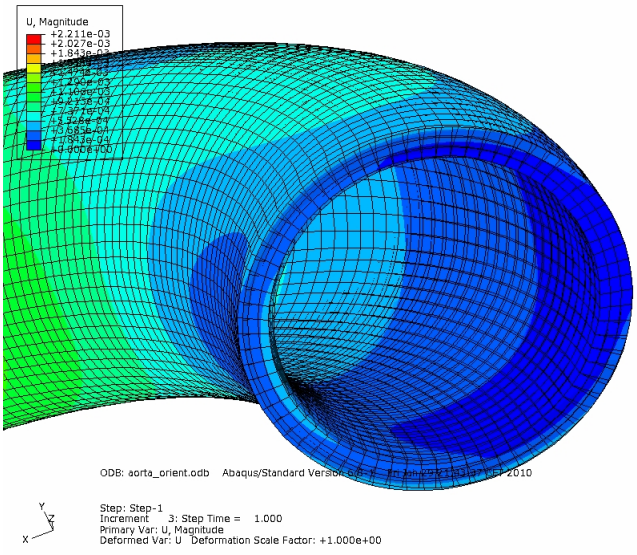

Figure 6.20: Deformed and configuration after the balancing step

It is important underline that it is necessary to define the radial, circumferential and longitudinal directions for every point of the model in

order to introduce the initial stress conditions. For the briachial-cephalic, common carotid and subclavian arteries three different cylindrical reference systems were created in ABAQUS CAE.
For the aortic arch (that have a more complex geometry), the direction cosines of the three axis were defined through the subroutine ORIENT (see appendix A). In figure 6.21 the assigned direction are showed.

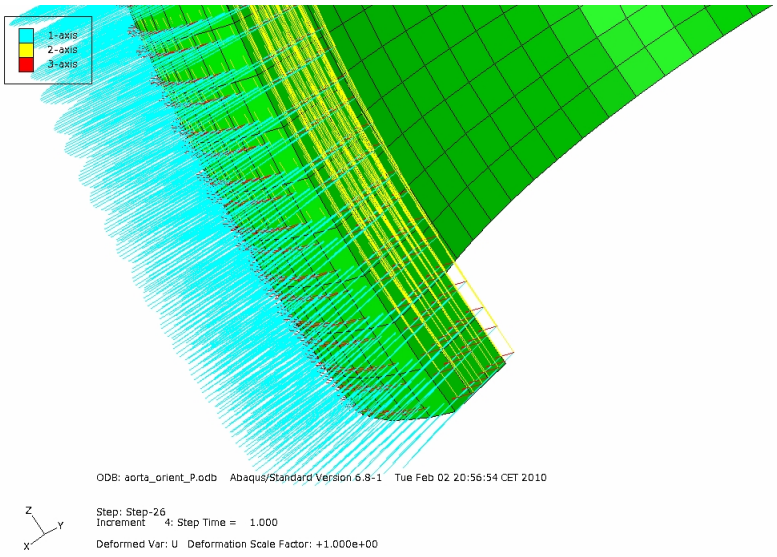

Figure 6.21: Assigned directions of the local reference system for the aortic arch. The axis 1 (blue), 2 (yellow) and 3 (red) are respectively the radial, longitudinal and circumferential directions

The constitutive model of the aortic wall has been implemented as a non linear hyperelastic Demiray material. In chapter 3 the features of this model and its implementation was discussed. The model needs two parameters to be defined (a, and b). The constants used in these simulations comes from the work of Herrera [19], in which in vitro experimental data on aortic samples are fitting using the Demiray material model.
The values used in our simulations will be $a = 54.419$ kPa and $b = 1.936$.

The cardiac cycle for the aortic wall was simulated by charging the internal surface of the model with a pressure load represented by the mapped pressure; practically this is done including a different *.mapd* file for each load step of the simulation. In this way 24 steps are required; every step is solved as a static analysis. This is a limitation of our model

that will be discuss in the chapter dedicate to the conclusions. A dynamic simulation should be a better choice but in this work the use of several static analyses can be a good approximation (see chapter 7).

6.2.2 Results

Time= 1.96 s

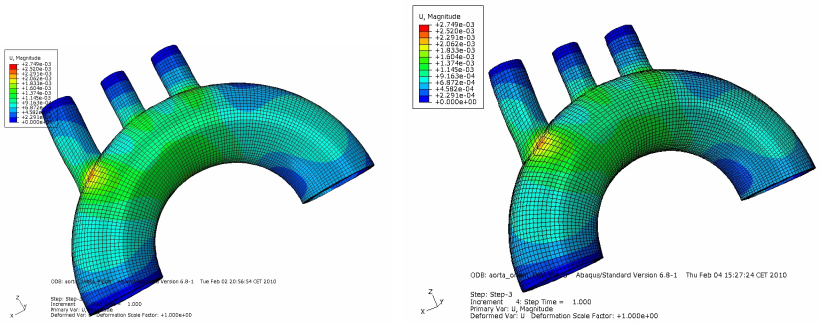

Time= 2 s

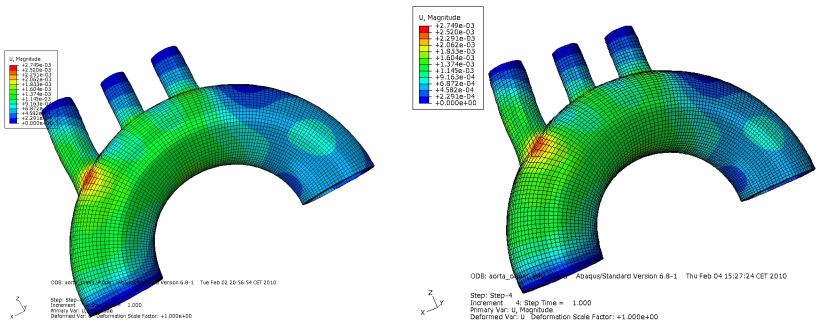

Time= 2.04 s

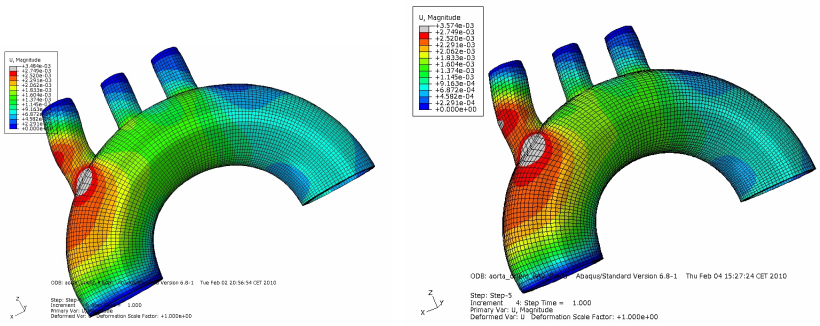

Time= 2.08 s

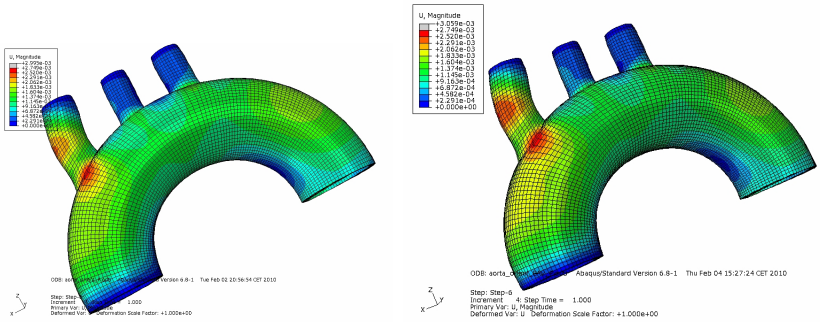

Time= 2.24 s

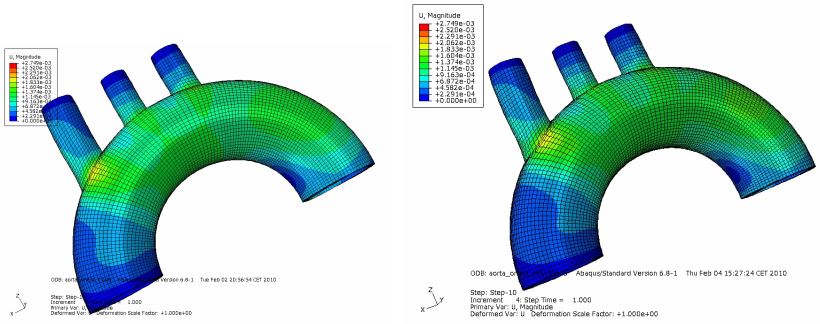

Time= 2.32 s

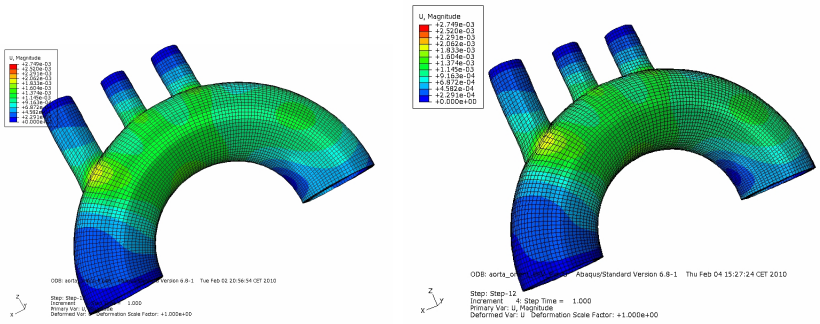

Figure 6.22: On the left column: mapping of displacements for the physiological model. On the right column: mapping of displacements for the BAV model

In the following pages the results of the physiological and BAV model will be compared as we did for the fluid domain results.
The deformation of the model, the circumferential and longitudinal stresses will be showed for the same time instants analyzed in the previous section.

In the figure 6.22 the map of the displacements is showed at different time instants, for the physiological model (right column) and for the BAV model (left column).

Time= 1.96 s

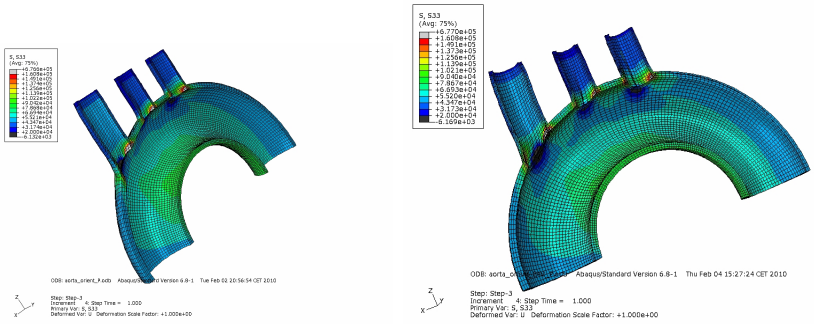

Time= 2 s

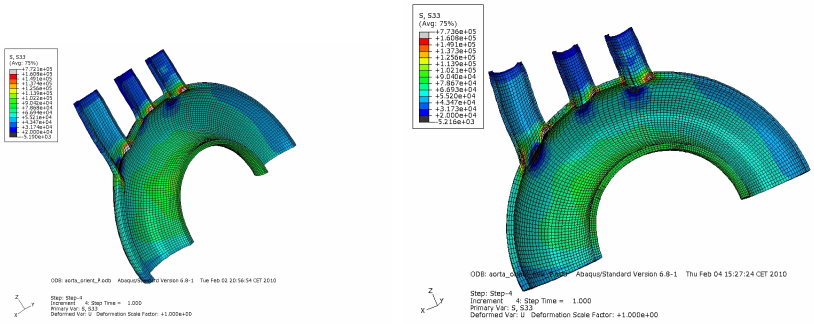

Time= 2.04 s

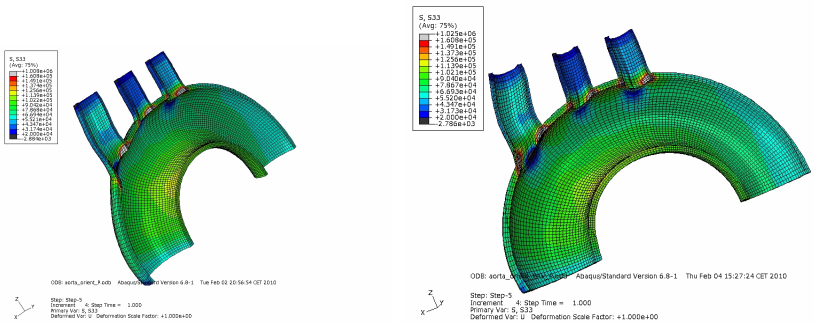

Time= 2.08 s

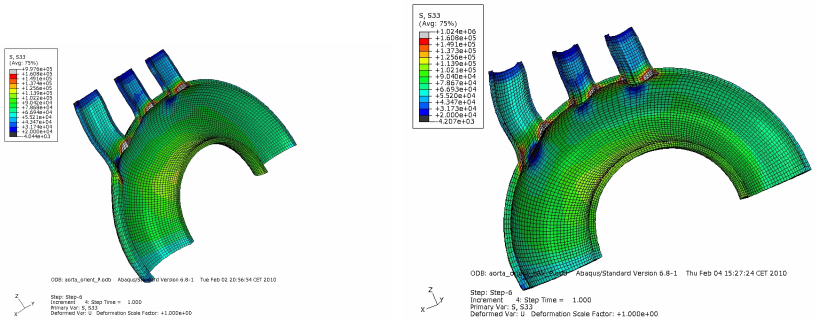

Time= 2.24 s

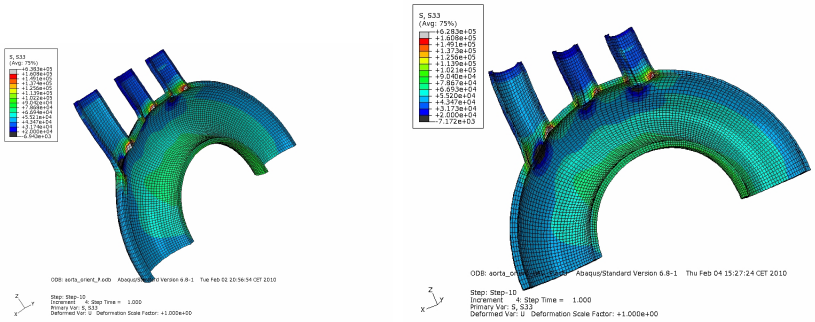

Time= 2.32 s

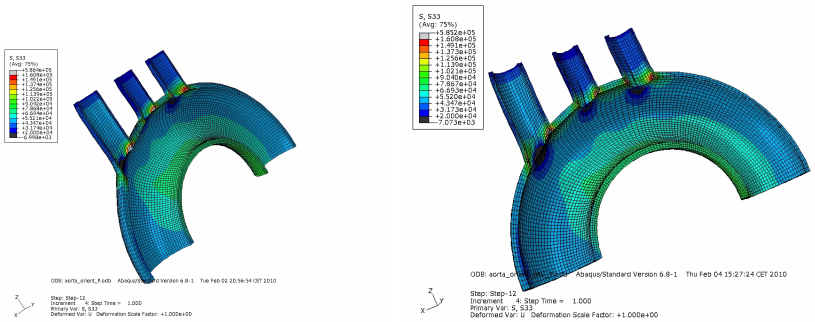

Figure 6.23: Circumferential stresses for the physiological (right) and the BAV model (left)

The maximum displacement is obviously observed during the systolic peak in the extrados region of the ascending aorta and it is about 2.7 mm according with the literature and with no significant differences between the two models.

In figure 6.23 the circumferential stress is shown. Also in this case the maximum stress is localized in the ascending aorta during the systolic peak and it is about $\sigma_\theta = 102.2$ kPa.

Time= 1.96 s

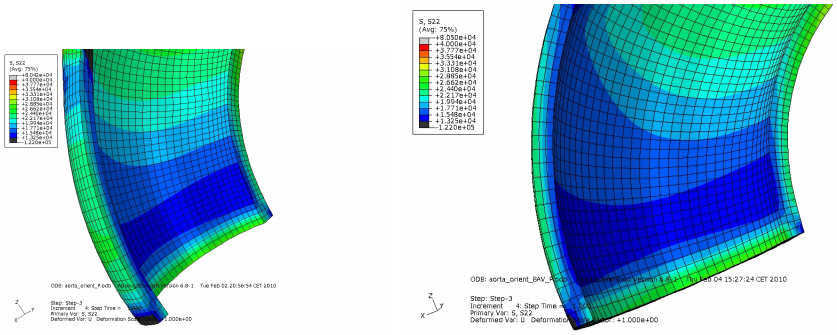

Time= 2 s

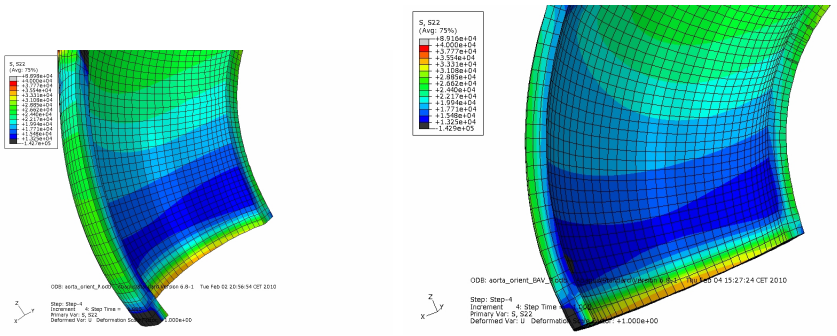

Time= 2.04 s

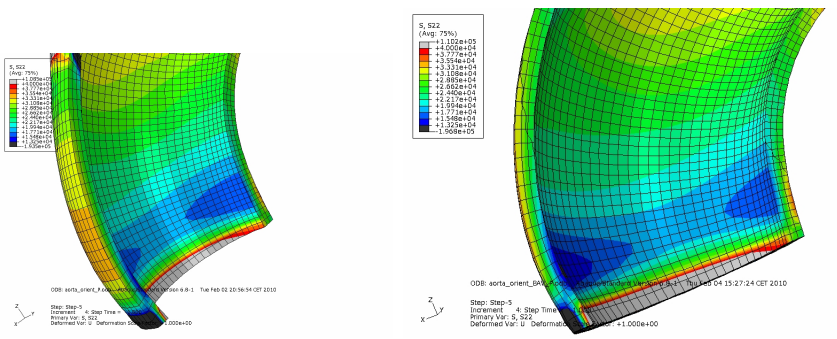

Time= 2.08 s

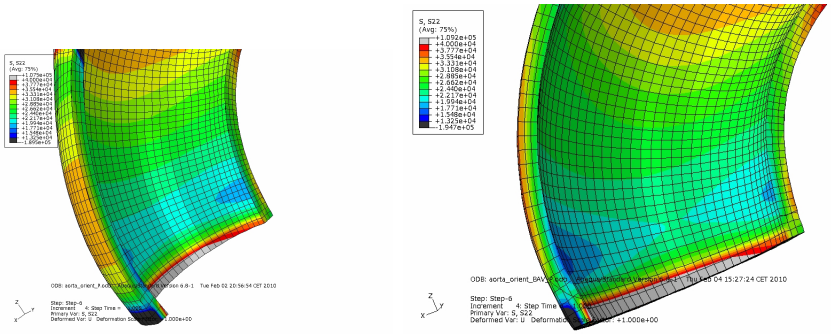

Time= 2.24 s

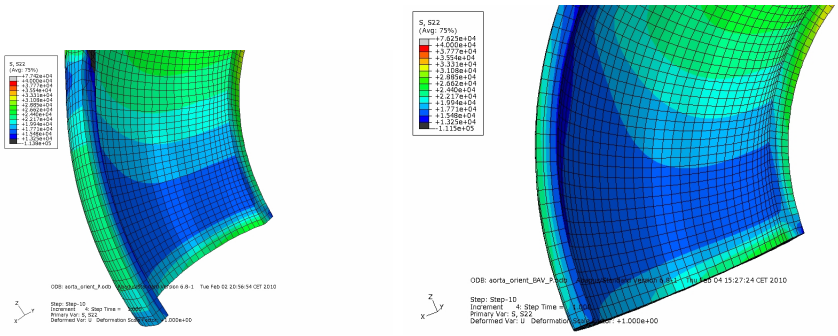

Time= 2.32 s

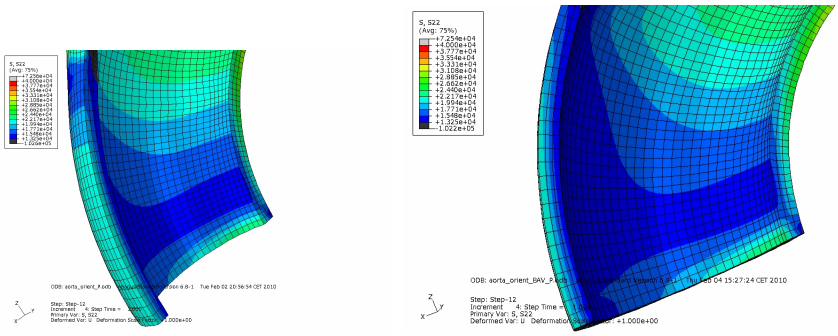

Figure 6.24: Longitudinal stresses for the physiological (right) and the BAV model (left)

In figure 6.24 the longitudinal stress is shown for both models. The results are showed for our section of interest, downstream of the aortic root. The value are one magnitude lower than the circumferential stress with a maximum of about 28.8 kPa.

In order to understand the influence of the pathology on the perceived stresses from the ascending aorta, the results have been compared along particular paths showed in the figure 6.25.

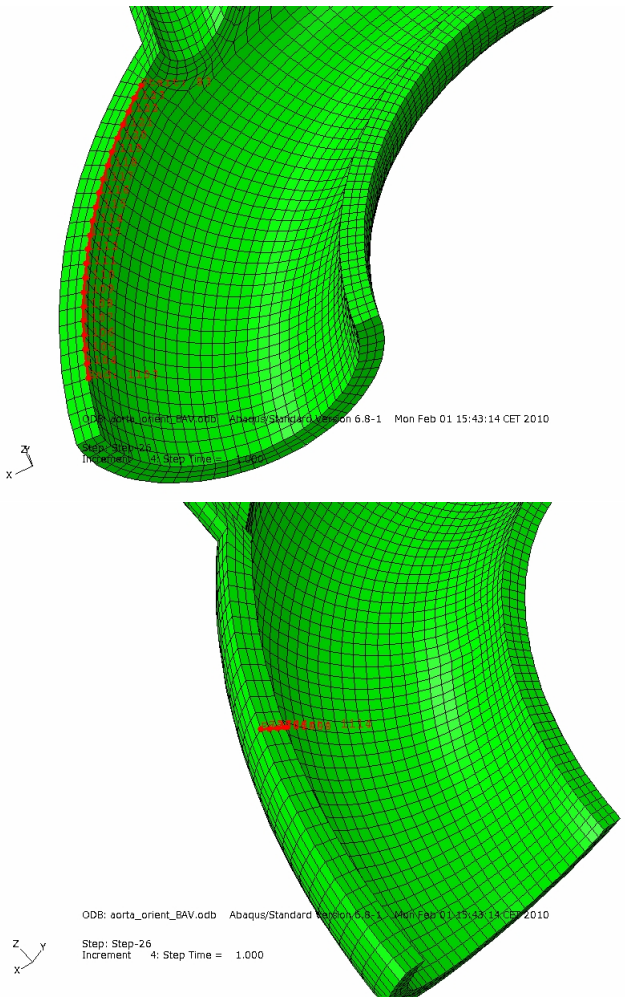

Figure 6.25: Axial (top) and radial (bottom) paths (red lines) for comparing the computed stresses

This particular axial path was chosen considering the wall shear stress distribution of figure 6.13; during the cardiac cycle the maximum difference between the two models appears along this path. Particularly during the peak of systole the maximum values of WSS are along the perimeter

of the section shown in 6.9, and for this reason the radial path of figure 6.25 was chosen to compare the values of stress of the two models.
In figures 6.26 and 6.27 it is possible to see that there are not significant differences of stress between the BAV and the physiological model.

(a) longitudinal stress

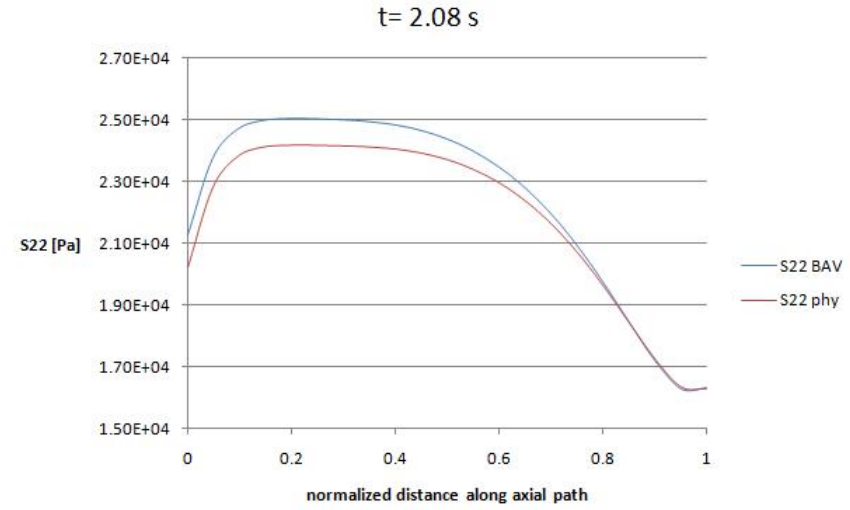

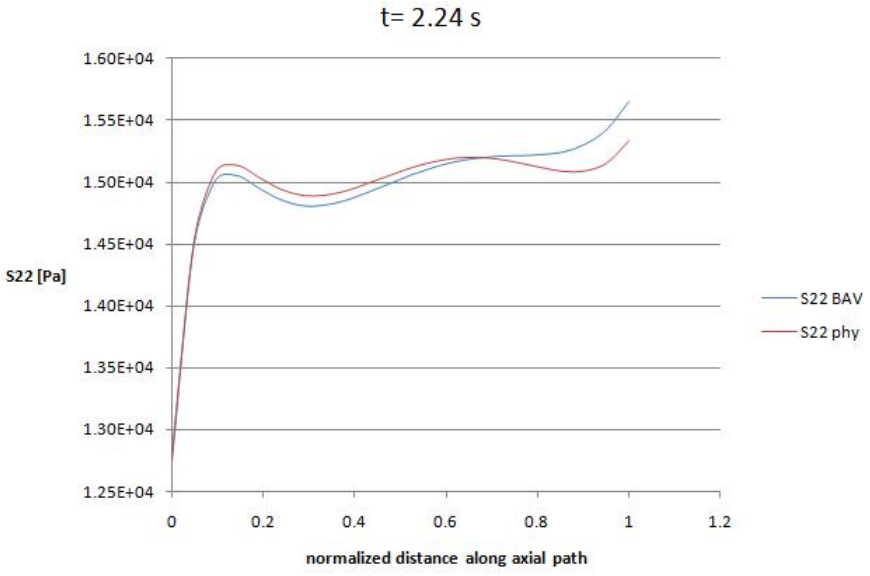

(b) circumferential stress

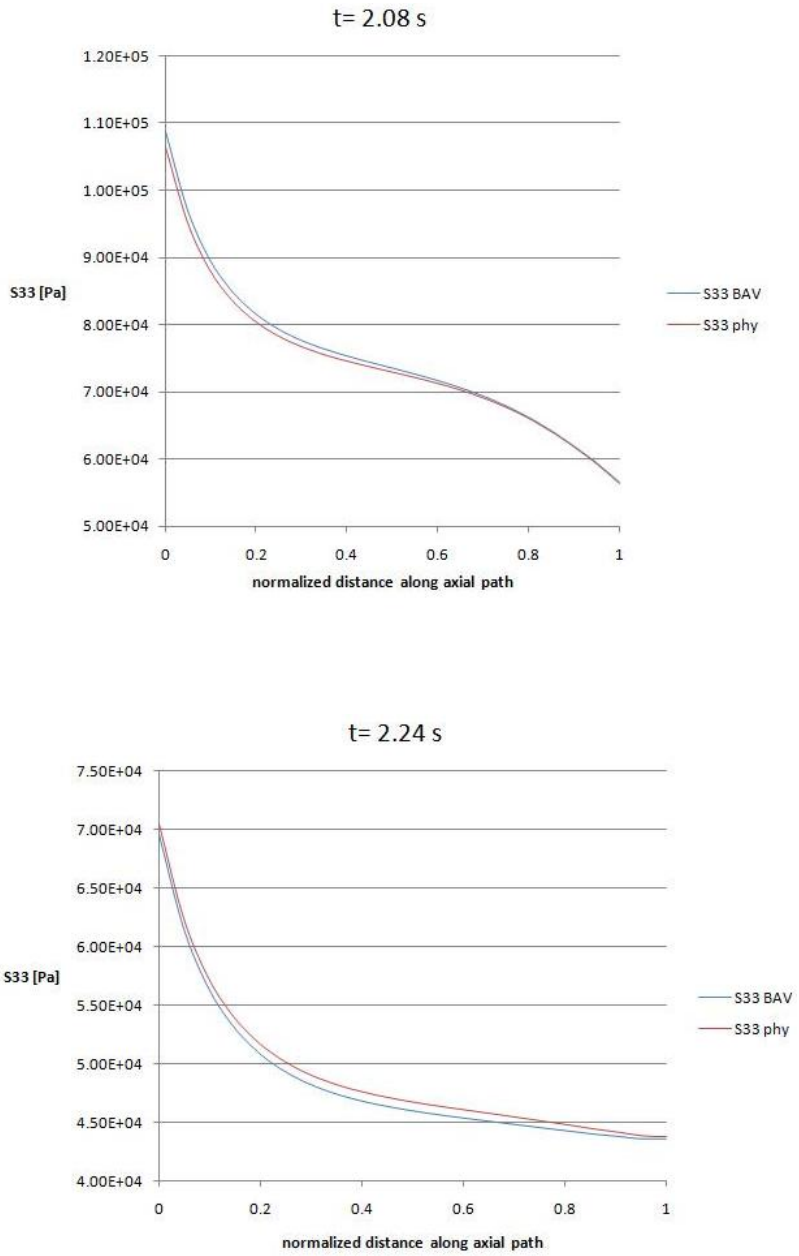

Figure 6.26: The longitudinal (a) and the circumferential (b) stress along the axial path (figure 6.25) at the time instants 2.08 s and 2.24 s

(a) longitudinal stress

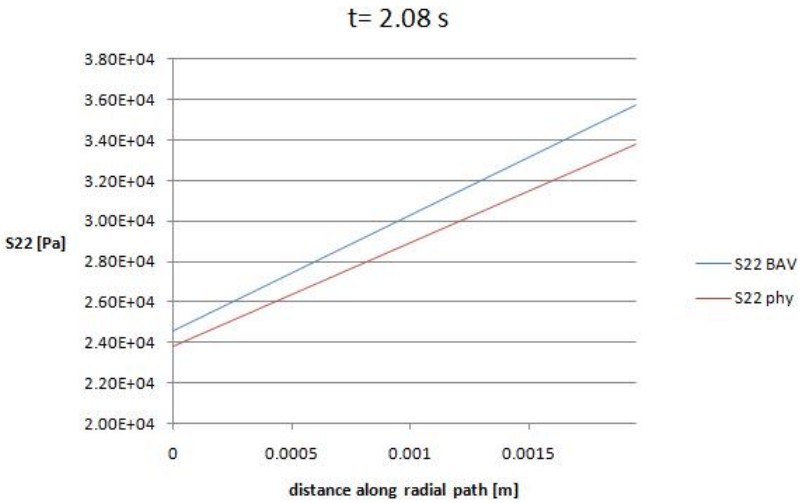

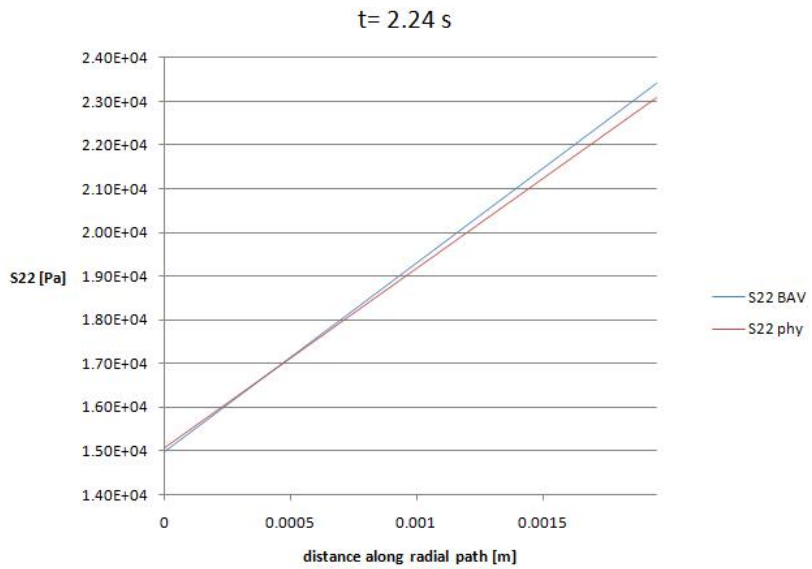

(b) circumferential stress

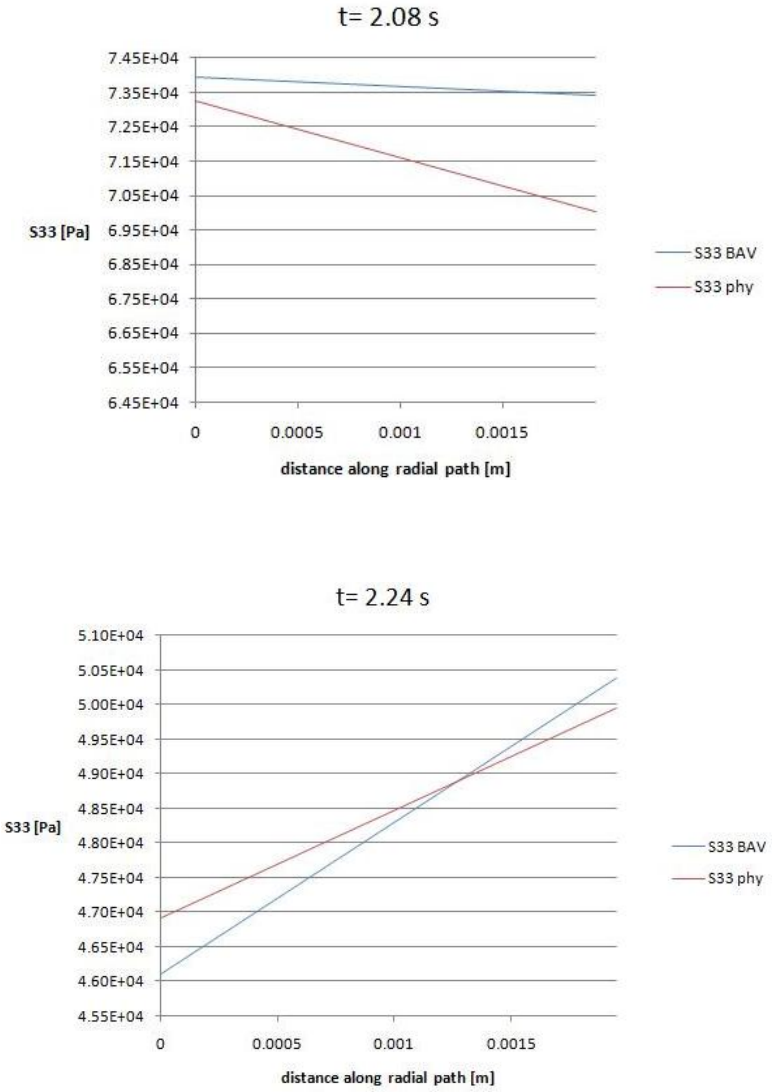

Figure 6.27: The longitudinal (a) and the circumferential (b) stress along the radial path (figure 6.25) path at the time instants 2.08 s and 2.24 s

Chapter 7

Conclusions

In this work the applied methodology and the results obtained with two models of the aortic arch have been described. One model represents the physiological cardiac cycle for an aortic arch including its main efferents arteries. The physiological conditions assume a three leaflets valve upstream of our geometry model; for these simulations a parabolic velocity profile at the inlet section (downstream of the aortic valve) was used.

The second model represents a cardiac cycle for an aortic arch downstream of a bicuspid aortic valve (BAV); in this case a particular asymmetric velocity profile at the inlet section was used in order to consider the abnormal opening way of the pathologic valve.

Both models don't include the aortic valve and the sinus. The models take into account the downstream effect of the valve for the physiological and pathological case. In the models the different valve morphology results in different velocity distribution at the inlet section.
The adequacy of the selected profiles will be further discussed.

With the proposed methods, the differences between the two clinical conditions have been analyzed.
Particularly the differences regarding the wall shear stress distribution have been investigate together with the pressure distributions and the corresponding stresses on the aortic wall during the cardiac cycle.
This has been done focusing especially on the region of the aortic arch called ascending aorta.

Many of the results discussed don't show relevant differences in the two models both for the fluid domain (blood flow) and the solid domain (aortic wall). Only comparing the wall shear stress results we can find significant differences, that are higher than 70 % in the region of the ascending aorta.
This is a very interesting result considering the clinical and biologic researches described in the chapter 2.

The increasing WSS caused by the BAV pathology seems to support the so called "hemodynamic" theory in the development of aneurysm of the ascending aorta; indeed the stresses "felt" by the aortic wall results quite independent from the blood's rheology features coming from the pathology condition. Then the WSS can actually play the main role in the aneurysm's developing through molecular pathway that can lead to the medial degeneration and consequent dilatation of the ascending aorta.

7.1 Limitations and possible improvements

The models presented in the previous chapters present various simplifications of the clinical reality from several points of view.
In this section we analyze the most critical aspects regarding the models used in this work.

In chapter 3 several constitutive models have been described. The Demiray model has been chosen for its computational simplicity and because of its adequacy to simulate the macroscopic mechanical behavior of the large arteries, as established in several work [10] [4]. Furthermore if the anisotropic behavior of the three layers of the arterial wall (with different collagen orientation) have to be taken in account, other models must to be used, for example the Holzapfel constitutive model. At the same way a time-dependent model could be used in order to consider the viscoelastic effects in the arteries.

In chapter 5 the mathematical aspect of the fluid-structure coupling

have been discussed; the need to implement a strong coupling for our models seems clear.
ABAQUS 6.8 and *Star CD* 4.1 support the co-simulation tool for the coupling but unfortunately this is a weak coupling: the pressure and shear stress information coming from the transient fluid dynamic simulations (Star CD) are exchanged with the solid domain solver (ABAQUS) that return the new position of the nodes match on the coupled surface and the velocity displacement too; in a weak coupling this exchange happens only one time for each time step.
In our model the terms of the equation (5.32) are too much similar (the blood density ρ_f is quite similar to the wall 's arteries density ρ_s) so, coupling the wall and the blood models, the simulations doesn't achieve convergence and are numerically unstable.
For this reason a one-way coupling was implemented with the methods described in chapter 6. The use of this coupling method is the main source of limitations of the model used.
Particularly, the fluid mesh is fixed along the cardiac cycle as if the aortic wall was rigid. In this way we lost the influence of the wall motion on the flow patterns and on the wall shear stress distribution.
Comparing a fixed wall and a moving wall model (made by using MRI data and FEM tools) some authors find that the WSS could be 25% less considering the wall motion [49]. Another approach could be to work with programs that support a monolithic coupling method like ANSYS or ADINA.
Also if our results for each model are affected by this errors, the protocol followed allows us to say that, anyway, the general effectiveness of comparing the BAV and the physiological models remains.

The boundary conditions used to simulate the differences between the two models, were described in chapter 6.
Particularly the velocity distributions on the inlet section are chosen as showed in the figure 6.6 assuming this special influence of the upstream aorta morphology on the downstream velocity profiles; both the profiles (for the physiological and BAV model) have a quite parabolic shape.
This is clearly a simplification in the ascending aorta's region where the flow is not completely developed. The model could be improved by us-

ing velocity distributions coming from MRI imaging data that could be inserted in the model as boundary conditions.

It was declared that the simulations done in ABAQUS are composed by several static instead of dynamic steps. In this way the inertial component of the solution for the aortic wall are neglected. This can be a reasonable approximation if the frequency content of the loads is lower than the first modal frequency of the solid structure.

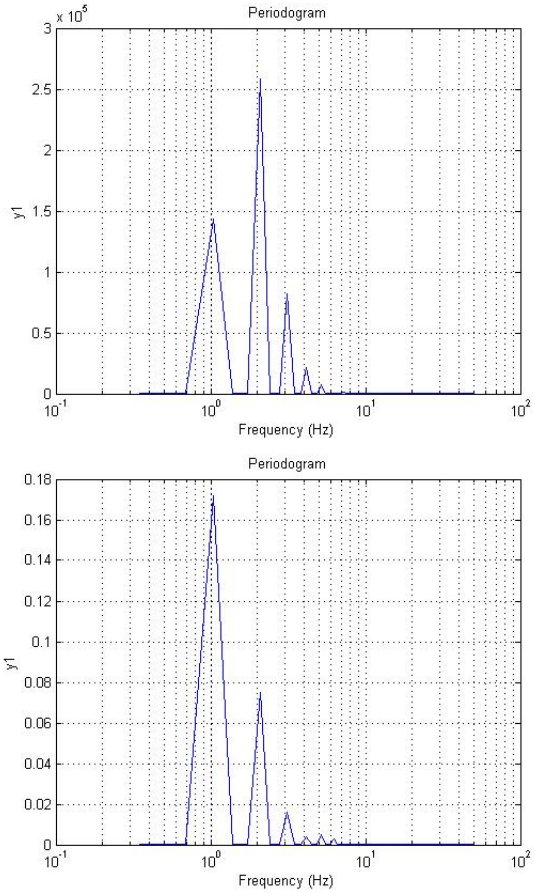

Figure 7.1: Frequency spectrum for the pressure outlet (top) and the velocity inlet (bottom) boundary conditions

In figure 7.1 the frequency spectrum of the boundary conditions used in the fluid domains are shown. The time trend is the same for both the physiological and the BAV model.
Some modal analysis have been done in ABAQUS; the first modal frequency found is 50 Hz that is greater than the frequency content of the

pressure applied.

Appendix A

Subroutines used in Abaqus

This Fortran file is composed by two subroutine. The first is the UHYPER subroutine, used for the definition of the hyperelastic material. The second is ORIENT, used to define the local reference system of the aortic arch.

```
          SUBROUTINE UHYPER(BI1,BI2,AJ,U,UI1,UI2,UI3,TEMP,NOEL,
     1 CMNAME,INCMPFLAG,NUMSTATEV,STATEV,NUMFIELDV,FIELDV,
     2 FIELDVINC,NUMPROPS,PROPS)
C
      INCLUDE 'ABA_PARAM.INC'
C
      CHARACTER*80 CMNAME
      DIMENSION U(2),UI1(3),UI2(6),UI3(6),STATEV(*),FIELDV(*),
     1 FIELDVINC(*),PROPS(*)
C     MATERIAL DE DEMIRAY

      REAL*8 A,B
C
      A=PROPS(1)
      B=PROPS(2)
C
      U(1)=A/B*(EXP(B/2*(BI1-3))-1)
```

```
      UI1(1)=A/2*EXP(B/2*(BI1-3))
      UI1(2)=0.
      UI2(1)=A*B/4*EXP(B/2*(BI1-3))
      UI2(2)=0.
      UI2(4)=0.
C
      RETURN
      END
C
      SUBROUTINE ORIENT(T,NOEL,NPT,LAYER,KSPT,COORDS,BASIS,ORNAME,
     1 NNODES,CNODES,JNNUM)
C
      INCLUDE 'ABA_PARAM.INC'
C
      CHARACTER*80 ORNAME
      DIMENSION T(3,3),COORDS(3),BASIS(3,3),CNODES(3,NNODES)
      DIMENSION JNNUM(NNODES)
C
      R=36.995D-3
C
      XT=SQRT(COORDS(1)**2+COORDS(3)**2)
C
      XR=SQRT(COORDS(1)**2+COORDS(2)**2)
C


      T(1,1)=COORDS(1) - COORDS(1)/XT*R
      T(2,1)=COORDS(2)
      T(3,1)=COORDS(3) - COORDS(3)/XT*R
      T(1,2)=-COORDS(3)
      T(2,2)=0D0
      T(3,2)=COORDS(1)



C
      RETURN
      END
```

Appendix B

Subroutines used in Star Cd for the outlet pressure boundary conditions

```
C*********************************************************
      SUBROUTINE BCDEFP(UB,VB,WB,PR,TE,ED,T,SCALAR,TURINT,RSU)
C     Boundary conditions definition for pressure boundaries
C*********************************************************
C-----------------------------------------*
C     STAR-CD VERSION 4.10.000
C-----------------------------------------*
      INCLUDE 'comdb.inc'
      COMMON/USR001/INTFLG(100)
      DIMENSION SCALAR(*)
      DIMENSION RSU(6)
      DIMENSION A(288)
      LOGICAL TURINT
      INCLUDE 'usrdat.inc'
      DIMENSION SCALC(50)
      EQUIVALENCE( UDAT12(001), ICTID )
      EQUIVALENCE( UDAT02(002), DEN )
      EQUIVALENCE( UDAT04(002), DENC )
      EQUIVALENCE( UDAT04(003), EDC )
      EQUIVALENCE( UDAT04(005), PRC )
```

```
      EQUIVALENCE( UDAT04(009), SCALC(01) )
      EQUIVALENCE( UDAT04(007), TC )
      EQUIVALENCE( UDAT04(008), TEC )
      EQUIVALENCE( UDAT04(059), UC )
      EQUIVALENCE( UDAT04(060), VC )
      EQUIVALENCE( UDAT04(061), WC )
      EQUIVALENCE( UDAT04(064), UCL )
      EQUIVALENCE( UDAT04(065), VCL )
      EQUIVALENCE( UDAT04(066), WCL )
      EQUIVALENCE( UDAT02(070), X )
      EQUIVALENCE( UDAT02(071), Y )
      EQUIVALENCE( UDAT02(072), Z )
C-------------------------------------------
C
C This subroutine enables the user to specify the conditions at
C  PRESSURE boundaries for UB,VB,WB,PR,TE,ED,T,SCALAR.
C
C ** Parameters to be returned to STAR-CD: UB,VB,WB,PR,
C      TE,ED,T,SCALAR,TURINT
C
C-------------------------------------------



      Rmax = 0.010195
      Xo = 0.036995
      Rlocal = ((X-Xo)**2.0+Y**2.0)**0.5
      i = 1



      data A/0,
     &       18.75,
     &       37.5,
     &       56.25,
     &       75,
     &       93.75,
```

```
&       112.5,
&       131.25,
&       150,
&       501.4917983,
&       749.8858657,
&       1002.450097,
&       1249.812385,
&       1482.600626,
&       1691.442712,
&       1866.966539,
&       1999.8,
&       2082.912549,
&       2118.639874,
&       2111.659223,
&       2066.647845,
&       1988.282985,
&       1881.241893,
&       1750.201815,
&       1599.84,
&       1434.971717,
&       1260.964325,
&       1083.323205,
&       907.5537366,
&       739.1613013,
&       583.6512797,
&       446.5290523,
&       333.3,
&       247.8778089,
&       187.8093874,
&       149.0499495,
&       127.554709,
&       119.2788798,
&       120.177676,
&       126.2063114,
&       133.32,
&       138.4167816,
```

```
&       142.1660001,
&       146.1798255,
&       152.0704275,
&       161.4499761,
&       175.9306412,
&       197.1245925,
&       226.644,
&       265.3796116,
&       311.336487,
&       361.7982642,
&       414.0485809,
&       465.371075,
&       513.0493843,
&       554.3671467,
&       586.608,
&       607.72253,
&       618.3291143,
&       619.7130788,
&       613.1597489,
&       599.9544504,
&       581.382509,
&       558.7292503,
&       533.28,
&       506.1704092,
&       477.9374306,
&       448.9683427,
&       419.6504235,
&       390.3709514,
&       361.5172046,
&       333.4764614,
&       306.636,
&       281.2888099,
&       257.3507256,
&       234.6432928,
&       212.9880571,
&       192.2065643,
```

```
&       172.12036,
&       152.55099,
&       133.32,
&       114.3070621,
&       95.62435439,
&       77.44218152,
&       59.93084806,
&       43.26065859,
&       27.6019177,
&       13.12492997,
&       0,
&       0,
&       0,
&       0,
&       0,
&       0,
&       0,
&       0,
&       0,
&       18.75,
&       37.5,
&       56.25,
&       75,
&       93.75,
&       112.5,
&       131.25,
&       150,
&       501.4917983,
&       749.8858657,
&       1002.450097,
&       1249.812385,
&       1482.600626,
&       1691.442712,
&       1866.966539,
&       1999.8,
&       2082.912549,
```

```
&       2118.639874,
&       2111.659223,
&       2066.647845,
&       1988.282985,
&       1881.241893,
&       1750.201815,
&       1599.84,
&       1434.971717,
&       1260.964325,
&       1083.323205,
&       907.5537366,
&       739.1613013,
&       583.6512797,
&       446.5290523,
&       333.3,
&       247.8778089,
&       187.8093874,
&       149.0499495,
&       127.554709,
&       119.2788798,
&       120.177676,
&       126.2063114,
&       133.32,
&       138.4167816,
&       142.1660001,
&       146.1798255,
&       152.0704275,
&       161.4499761,
&       175.9306412,
&       197.1245925,
&       226.644,
&       265.3796116,
&       311.336487,
&       361.7982642,
&       414.0485809,
&       465.371075,
```

```
&       513.0493843,
&       554.3671467,
&       586.608,
&       607.72253,
&       618.3291143,
&       619.7130788,
&       613.1597489,
&       599.9544504,
&       581.382509,
&       558.7292503,
&       533.28,
&       506.1704092,
&       477.9374306,
&       448.9683427,
&       419.6504235,
&       390.3709514,
&       361.5172046,
&       333.4764614,
&       306.636,
&       281.2888099,
&       257.3507256,
&       234.6432928,
&       212.9880571,
&       192.2065643,
&       172.12036,
&       152.55099,
&       133.32,
&       114.3070621,
&       95.62435439,
&       77.44218152,
&       59.93084806,
&       43.26065859,
&       27.6019177,
&       13.12492997,
&       0,
&       0,
```

```
&       0,
&       0,
&       0,
&       0,
&       0,
&       0,
&       0,
&       18.75,
&       37.5,
&       56.25,
&       75,
&       93.75,
&       112.5,
&       131.25,
&       150,
&       501.4917983,
&       749.8858657,
&       1002.450097,
&       1249.812385,
&       1482.600626,
&       1691.442712,
&       1866.966539,
&       1999.8,
&       2082.912549,
&       2118.639874,
&       2111.659223,
&       2066.647845,
&       1988.282985,
&       1881.241893,
&       1750.201815,
&       1599.84,
&       1434.971717,
&       1260.964325,
&       1083.323205,
&       907.5537366,
&       739.1613013,
```

```
&       583.6512797,
&       446.5290523,
&       333.3,
&       247.8778089,
&       187.8093874,
&       149.0499495,
&       127.554709,
&       119.2788798,
&       120.177676,
&       126.2063114,
&       133.32,
&       138.4167816,
&       142.1660001,
&       146.1798255,
&       152.0704275,
&       161.4499761,
&       175.9306412,
&       197.1245925,
&       226.644,
&       265.3796116,
&       311.336487,
&       361.7982642,
&       414.0485809,
&       465.371075,
&       513.0493843,
&       554.3671467,
&       586.608,
&       607.72253,
&       618.3291143,
&       619.7130788,
&       613.1597489,
&       599.9544504,
&       581.382509,
&       558.7292503,
&       533.28,
&       506.1704092,
```

```
&       477.9374306,
&       448.9683427,
&       419.6504235,
&       390.3709514,
&       361.5172046,
&       333.4764614,
&       306.636,
&       281.2888099,
&       257.3507256,
&       234.6432928,
&       212.9880571,
&       192.2065643,
&       172.12036,
&       152.55099,
&       133.32,
&       114.3070621,
&       95.62435439,
&       77.44218152,
&       59.93084806,
&       43.26065859,
&       27.6019177,
&       13.12492997,
&       0,
&       0,
&       0,
&       0,
&       0,
&       0,
&       0,
&       0/

 if (TIME.LE.2.88) then
   i=100*TIME
   PR=A(i)
 endif
```

```
      RETURN
      END
C
```

Appendix C

Subroutines used in Star CD for the physiologic inlet coundary condition

```
C*****************************************
SUBROUTINE BCDEFI(SCALAR,U,V,W,TE,ED,T,DEN,TURINT,RSU,V2P,F2P)
C Boundary conditions at inlets
C*****************************************
C----------------------------------------------*
C STAR-CD VERSION 4.06.000
C----------------------------------------------*
INCLUDE 'comdb.inc'
COMMON/USR001/INTFLG(100)
DIMENSION SCALAR(*)
DIMENSION RSU(6)
DIMENSION A(288)
LOGICAL TURINT

INCLUDE 'usrdat.inc'
DIMENSION SCALC(50)
EQUIVALENCE( UDAT12(001), ICTID )
EQUIVALENCE( UDAT04(002), DENC )
EQUIVALENCE( UDAT04(003), EDC )
EQUIVALENCE( UDAT02(005), PR )
EQUIVALENCE( UDAT04(005), PRC )
```

```
EQUIVALENCE( UDAT04(009), SCALC(01) )
EQUIVALENCE( UDAT04(007), TC )
EQUIVALENCE( UDAT04(008), TEC )
EQUIVALENCE( UDAT04(059), UC )
EQUIVALENCE( UDAT04(060), VC )
EQUIVALENCE( UDAT04(061), WC )
EQUIVALENCE( UDAT04(064), UCL )
EQUIVALENCE( UDAT04(065), VCL )
EQUIVALENCE( UDAT04(066), WCL )
EQUIVALENCE( UDAT02(070), X )
EQUIVALENCE( UDAT02(071), Y )
EQUIVALENCE( UDAT02(072), Z )
C---------------------------------------- C
C This subroutine enables the user to specify INLET boundary
C conditions for U,V,W,TE,ED,T,(V22,F22 for V2F model) and SCALAR.
C
C
C ** Parameters to be returned to STAR: U,V,W,TE,ED,T, C SCALAR,
C    DEN, TURINT
C
C NB U,V and W are in the local coordinate-system of the
C inlet boundary.
C
C-------------------------------------C
C---- This subroutine gives the inlet fluid a parabolic profile.
C It will be required to update this subroutine with different
C geometries, flow conditions, and coordinate systems.




      Rmax = 0.01025
      Xo = 0
      Rlocal = ((X-Xo)**2.0+Y**2.0)**0.5
      i = 0
      data A/0,
```

```
&       0.015,
&       0.03031256,
&       0.060625121,
&       0.090937681,
&       0.121250242,
&       0.181875362,
&       0.35125683,
&       0.533042729,
&       0.717525777,
&       0.894998693,
&       1.055754193,
&       1.190084995,
&       1.288283817,
&       1.343453989,
&       1.359941297,
&       1.34490214,
&       1.305492915,
&       1.24887002,
&       1.182189855,
&       1.112085515,
&       1.043096886,
&       0.97924055,
&       0.924533092,
&       0.881670074,
&       0.84806298,
&       0.819802273,
&       0.792978419,
&       0.763681881,
&       0.728003123,
&       0.682032609,
&       0.623064256,
&       0.553205794,
&       0.47576841,
&       0.394063285,
&       0.311333121,
&       0.23054668,
```

```
     &       0.154604241,
     &       0.086406082,
     &       0.028852482,
     &       0,
     &       0,
     &       0,
     &       0,
     &       0,
     &       0,
     &       0,
     &       0,
     &       0,
     &       0,
     &       0,
     &       0,
     &       0,
     &       0,
     &       0,
     &       0,
     &       0,
     &       0,
     &       0,
     &       0,
     &       0,
     &       0,
     &       0,
     &       0,
     &       0,
     &       0,
     &       0,
     &       0,
     &       0,
     &       0,
     &       0,
     &       0,
     &       0,
```

```
&       0,
&       0,
&       0,
&       0,
&       0,
&       0,
&       0,
&       0,
&       0,
&       0,
&       0,
&       0,
&       0,
&       0,
&       0,
&       0,
&       0,
&       0,
&       0,
&       0,
&       0,
&       0,
&       0,
&       0,
&       0,
&       0,
&       0.015,
&       0.03031256,
&       0.060625121,
&       0.090937681,
&       0.121250242,
&       0.181875362,
&       0.35125683,
&       0.533042729,
&       0.717525777,
&       0.894998693,
&       1.055754193,
&       1.190084995,
```

```
&       1.288283817,
&       1.343453989,
&       1.359941297,
&       1.34490214,
&       1.305492915,
&       1.24887002,
&       1.182189855,
&       1.112085515,
&       1.043096886,
&       0.97924055,
&       0.924533092,
&       0.881670074,
&       0.84806298,
&       0.819802273,
&       0.792978419,
&       0.763681881,
&       0.728003123,
&       0.682032609,
&       0.623064256,
&       0.553205794,
&       0.47576841,
&       0.394063285,
&       0.311333121,
&       0.23054668,
&       0.154604241,
&       0.086406082,
&       0.028852482,
&       0,
&       0,
&       0,
&       0,
&       0,
&       0,
&       0,
&       0,
&       0,
```

```
     &          0,
     &          0,
     &          0,
     &          0,
     &          0,
     &          0,
     &          0,
     &          0,
     &          0,
     &          0,
     &          0,
     &          0,
     &          0,
     &          0,
     &          0,
     &          0,
     &          0,
     &          0,
     &          0,
     &          0,
     &          0,
     &          0,
     &          0,
     &          0,
     &          0,
     &          0,
     &          0,
     &          0,
     &          0,
     &          0,
     &          0,
     &          0,
     &          0,
     &          0,
     &          0,
     &          0,
```

```
&       0,
&       0,
&       0,
&       0,
&       0,
&       0,
&       0,
&       0,
&       0,
&       0,
&       0,
&       0,
&       0.015,
&       0.03031256,
&       0.060625121,
&       0.090937681,
&       0.121250242,
&       0.181875362,
&       0.35125683,
&       0.533042729,
&       0.717525777,
&       0.894998693,
&       1.055754193,
&       1.190084995,
&       1.288283817,
&       1.343453989,
&       1.359941297,
&       1.34490214,
&       1.305492915,
&       1.24887002,
&       1.182189855,
&       1.112085515,
&       1.043096886,
&       0.97924055,
&       0.924533092,
&       0.881670074,
```

```
&       0.84806298,
&       0.819802273,
&       0.792978419,
&       0.763681881,
&       0.728003123,
&       0.682032609,
&       0.623064256,
&       0.553205794,
&       0.47576841,
&       0.394063285,
&       0.311333121,
&       0.23054668,
&       0.154604241,
&       0.086406082,
&       0.028852482,
&       0,
&       0,
&       0,
&       0,
&       0,
&       0,
&       0,
&       0,
&       0,
&       0,
&       0,
&       0,
&       0,
&       0,
&       0,
&       0,
&       0,
&       0,
&       0,
&       0,
&       0,
&       0,
&       0,
```

```
     &       0,
     &       0,
     &       0,
     &       0,
     &       0,
     &       0,
     &       0,
     &       0,
     &       0,
     &       0,
     &       0,
     &       0,
     &       0,
     &       0,
     &       0,
     &       0,
     &       0,
     &       0,
     &       0,
     &       0,
     &       0,
     &       0,
     &       0,
     &       0,
     &       0,
     &       0,
     &       0,
     &       0,
     &       0,
     &       0,
     &       0,
     &       0,
     &       0,
     &       0,
     &       0,
     &       0,
     &       0,
     &       0,
     &       0,
     &       0,
     &       0,
     &       0,
     &       0/
```

```
if (TIME.LE.2.88) then
  i=100*TIME
  W = 2*A(i)*(1.0-(Rlocal/Rmax)**2)
endif

      RETURN
      END
```

Appendix D

Subroutines used in Star CD for the inlet velocity in the BAV computational model

```
C*************************************************************
SUBROUTINE BCDEFI(SCALAR,U,V,W,TE,ED,T,DEN,TURINT,RSU,V2P,F2P)
C Boundary conditions at inlets
C*************************************************************
C----------- STAR-CD VERSION 4.06.000 ---------C
INCLUDE 'comdb.inc'
COMMON/USR001/INTFLG(100)
DIMENSION SCALAR(*)
DIMENSION RSU(6)
DIMENSION A(288)
LOGICAL TURINT

INCLUDE 'usrdat.inc'
DIMENSION SCALC(50)
EQUIVALENCE( UDAT12(001), ICTID )
EQUIVALENCE( UDAT04(002), DENC )
EQUIVALENCE( UDAT04(003), EDC )
EQUIVALENCE( UDAT02(005), PR )
EQUIVALENCE( UDAT04(005), PRC )
EQUIVALENCE( UDAT04(009), SCALC(01) )
```

```
EQUIVALENCE( UDAT04(007), TC )
EQUIVALENCE( UDAT04(008), TEC )
EQUIVALENCE( UDAT04(059), UC )
EQUIVALENCE( UDAT04(060), VC )
EQUIVALENCE( UDAT04(061), WC )
EQUIVALENCE( UDAT04(064), UCL )
EQUIVALENCE( UDAT04(065), VCL )
EQUIVALENCE( UDAT04(066), WCL )
EQUIVALENCE( UDAT02(070), X )
EQUIVALENCE( UDAT02(071), Y )
EQUIVALENCE( UDAT02(072), Z )
C------------------------------------------------ C
C This subroutine enables the user to specify INLET boundary
C conditions for U,V,W,TE,ED,T,(V22,F22 for V2F model) and SCALAR.
C
C
C ** Parameters to be returned to STAR: U,V,W,TE,ED,T,
C SCALAR, DEN, TURINT C C NB U,V and W are in the local
Ccoordinate-system of the  inlet boundary.
C
C------------------------------------------------ C




      R = 0.01025
      X0=0.036995
      a0=1
      b0=1
      a=1.7
      b=1
      c=1
      d=1
      i=1
      data A/0,
     &       0.015,
```

```
&       0.03031256,
&       0.060625121,
&       0.090937681,
&       0.121250242,
&       0.181875362,
&       0.35125683,
&       0.533042729,
&       0.717525777,
&       0.894998693,
&       1.055754193,
&       1.190084995,
&       1.288283817,
&       1.343453989,
&       1.359941297,
&       1.34490214,
&       1.305492915,
&       1.24887002,
&       1.182189855,
&       1.112085515,
&       1.043096886,
&       0.97924055,
&       0.924533092,
&       0.881670074,
&       0.84806298,
&       0.819802273,
&       0.792978419,
&       0.763681881,
&       0.728003123,
&       0.682032609,
&       0.623064256,
&       0.553205794,
&       0.47576841,
&       0.394063285,
&       0.311333121,
&       0.23054668,
&       0.154604241,
```

```
     &        0.086406082,
     &        0.028852482,
     &        0,
     &        0,
     &        0,
     &        0,
     &        0,
     &        0,
     &        0,
     &        0,
     &        0,
     &        0,
     &        0,
     &        0,
     &        0,
     &        0,
     &        0,
     &        0,
     &        0,
     &        0,
     &        0,
     &        0,
     &        0,
     &        0,
     &        0,
     &        0,
     &        0,
     &        0,
     &        0,
     &        0,
     &        0,
     &        0,
     &        0,
     &        0,
     &        0,
     &        0,
```

```
&       0,
&       0,
&       0,
&       0,
&       0,
&       0,
&       0,
&       0,
&       0,
&       0,
&       0,
&       0,
&       0,
&       0,
&       0,
&       0,
&       0,
&       0,
&       0,
&       0,
&       0,
&       0,
&       0,
&       0,
&       0,
&       0.015,
&       0.03031256,
&       0.060625121,
&       0.090937681,
&       0.121250242,
&       0.181875362,
&       0.35125683,
&       0.533042729,
&       0.717525777,
&       0.894998693,
&       1.055754193,
&       1.190084995,
&       1.288283817,
```

```
&       1.343453989,
&       1.359941297,
&       1.34490214,
&       1.305492915,
&       1.24887002,
&       1.182189855,
&       1.112085515,
&       1.043096886,
&       0.97924055,
&       0.924533092,
&       0.881670074,
&       0.84806298,
&       0.819802273,
&       0.792978419,
&       0.763681881,
&       0.728003123,
&       0.682032609,
&       0.623064256,
&       0.553205794,
&       0.47576841,
&       0.394063285,
&       0.311333121,
&       0.23054668,
&       0.154604241,
&       0.086406082,
&       0.028852482,
&       0,
&       0,
&       0,
&       0,
&       0,
&       0,
&       0,
&       0,
&       0,
&       0,
```

```
&       0,
&       0,
&       0,
&       0,
&       0,
&       0,
&       0,
&       0,
&       0,
&       0,
&       0,
&       0,
&       0,
&       0,
&       0,
&       0,
&       0,
&       0,
&       0,
&       0,
&       0,
&       0,
&       0,
&       0,
&       0,
&       0,
&       0,
&       0,
&       0,
&       0,
&       0,
&       0,
&       0,
&       0,
&       0,
&       0,
&       0,
&       0,
&       0,
&       0,
&       0,
&       0,
&       0,
```

```
&       0,
&       0,
&       0,
&       0,
&       0,
&       0,
&       0,
&       0,
&       0,
&       0,
&       0,
&       0.015,
&       0.03031256,
&       0.060625121,
&       0.090937681,
&       0.121250242,
&       0.181875362,
&       0.35125683,
&       0.533042729,
&       0.717525777,
&       0.894998693,
&       1.055754193,
&       1.190084995,
&       1.288283817,
&       1.343453989,
&       1.359941297,
&       1.34490214,
&       1.305492915,
&       1.24887002,
&       1.182189855,
&       1.112085515,
&       1.043096886,
&       0.97924055,
&       0.924533092,
&       0.881670074,
&       0.84806298,
```

```
&       0.819802273,
&       0.792978419,
&       0.763681881,
&       0.728003123,
&       0.682032609,
&       0.623064256,
&       0.553205794,
&       0.47576841,
&       0.394063285,
&       0.311333121,
&       0.23054668,
&       0.154604241,
&       0.086406082,
&       0.028852482,
&       0,
&       0,
&       0,
&       0,
&       0,
&       0,
&       0,
&       0,
&       0,
&       0,
&       0,
&       0,
&       0,
&       0,
&       0,
&       0,
&       0,
&       0,
&       0,
&       0,
&       0,
&       0,
&       0,
```

```
     &       0,
     &       0,
     &       0,
     &       0,
     &       0,
     &       0,
     &       0,
     &       0,
     &       0,
     &       0,
     &       0,
     &       0,
     &       0,
     &       0,
     &       0,
     &       0,
     &       0,
     &       0,
     &       0,
     &       0,
     &       0,
     &       0,
     &       0,
     &       0,
     &       0,
     &       0,
     &       0,
     &       0,
     &       0,
     &       0,
     &       0,
     &       0,
     &       0,
     &       0,
     &       0,
     &       0,
     &       0,
     &       0/

      if (TIME.LE.0.2) then
```

```
  i=100*TIME
  a0=a0-6*i
  W=2*A(i)*((X-X0)**2+Y**2-R**2)*(exp(-c*(X-X0)**2-d*Y**2
 .-a0*(X-X0)-b0*Y));

endif

 if (TIME.GT.0.2.AND.TIME.LE.0.96) then
  i=100*TIME
  a0=a0-120+6*i
  W=2*A(i)*((X-X0)**2+Y**2-R**2)*(exp(-c*(X-X0)**2-d*Y**2
 .-a0*(X-X0)-b0*Y));
endif

if (TIME.GT.0.96.AND.TIME.LE.1.16) then
  i=100*TIME
  a0=a0-6*(i-96)
  W=2*A(i)*((X-X0)**2+Y**2-R**2)*(exp(-c*(X-X0)**2-d*Y**2
 .-a0*(X-X0)-b0*Y));
endif

if (TIME.GT.1.16.AND.TIME.LE.1.92) then
  i=100*TIME
  a0=a0-120+6*(i-116)
  W=2*A(i)*((X-X0)**2+Y**2-R**2)*(exp(-c*(X-X0)**2-d*Y**2
 .-a0*(X-X0)-b0*Y));
endif

if (TIME.GT.1.92.AND.TIME.LE.2.12) then
  i=100*TIME
  a0=a0-6*(i-192)
  W=2*A(i)*((X-X0)**2+Y**2-R**2)*(exp(-c*(X-X0)**2-d*Y**2
 .-a0*(X-X0)-b0*Y));
endif

if (TIME.GT.2.12) then
```

```
  i=100*TIME
  a0=a0-120+6*(i-212)
  W=2*A(i)*((X-X0)**2+Y**2-R**2)*(exp(-c*(X-X0)**2-d*Y**2
 .-a0*(X-X0)-b0*Y));
endif


RETURN
END
```

Appendix E

Macro used in Star CD

E.1 Plot pressure and velocity magnitude in a transient analysis

```
!
! Macro 12-1: Animate transient results.
!
!-User to define:
*SET,TIME,1.91,0.01
!-End of user defined values
TRLOAD,,
POPT,CONT
PLTY,EHID
CSET,NEWS,FLUID
TRINTERPOLATE,ON,CAVER,CSET
*SET,FRM,1097,1
*DEFI,NOEX
STOR,TIME,TIME
GETC,VMAG,P
SCDU,GIF,FRM
CPLOT
SCDU,OFF
*END
*LOOP,1.0,97,1.0
```

E.2 Plot wall shear stress magnitude in a transient analysis

```
!
! Macro 12-2: Animate transient results.
!
!-User to define:
*SET,TIME,1.91,0.01
!-End of user defined values
TRLOAD,,
POPT,CONT
PLTY,EHID
CSET,NEWS,FLUID
TRINTERPOLATE,ON,CAVER,CSET
*SET,FRM,1195,1
*DEFI,NOEX
STOR,TIME,TIME
oper,getw,sfxyz,6
oper,getw,area,5
oper,divid,6,5,4
oper,plload
cave,all
SCDU,GIF,FRM
popt,cont
wplot $replot
SCDU,OFF
*END
*LOOP,1.0,97,1.0
```

E.3 Plot the vectorial representation of the wall shear stress in a transient analysis

```
!
! Macro 12-3: Animate transient results.
!
```

```
!-User to define:
*SET,TIME,1.91,0.01
!-End of user defined values
TRLOAD,,
POPT,CONT
PLTY,EHID
CSET,NEWS,FLUID
TRINTERPOLATE,ON,CAVER,CSET
*SET,FRM,1629,1
*DEFI,NOEX
STOR,TIME,TIME
oper,getw,sfx,1
oper,getw,sfy,2
oper,getw,sfz,3
oper,getw,area,5
oper,divid,1,5,1
oper,smult,-1,1,1
oper,divid,2,5,2
oper,smult,-1,2,2
oper,divid,3,5,3
oper,smult,-1,3,3
oper,plload
cave,all
SCDU,GIF,FRM
popt,vect
wplot $replot
SCDU,OFF
*END
*LOOP,1.0,97,1.0
```

E.4 Plot the WSS percentage difference between the BAV and the physiological model

First the wss is aquired from the result file of the simulation regarding the physiological model:

```
oper,clear,1
oper,clear,2
oper,clear,3
oper,clear,4
oper,clear,5
oper,clear,6
oper,getw,sfxyz,6
oper,getw,area,5
oper,divid,6,5,6
oper,plload
popt,cont
wplot $replot
```

Later the wss is acquired from the result file of the BAV simulation (opening the result file and executing the following macro)

```
oper,getw,sfxyz,4
oper,getw,area,5
oper,divid,4,5,4
oper,plload
popt,cont
wplot $replot
```

Last the following macro is executed

```
oper,subtract,6,4,4
oper,divid,4,6,4
oper,smult,100,4,4
oper,plload
cave,all
popt,cont
wplot $replot
```

Appendix F

.mapd files

This is a part of a *.mapd* file genereted by Star CD. In this case the pressure at the time instant 2.36 resulting from the fluid dynamics simulation of the BAV model is mapped on the coupling surface of the ABAQUS model.

```
*DLOAD, op=NEW
AORTA_SOLID.106,P5,   101.06851
AORTA_SOLID.107,P5,   105.84074
AORTA_SOLID.116,P5,   104.39200
AORTA_SOLID.232,P5,   101.06851
AORTA_SOLID.233,P5,   105.84074
AORTA_SOLID.242,P5,   80.271000
AORTA_SOLID.358,P5,   69.539634
AORTA_SOLID.359,P5,   86.216580
AORTA_SOLID.368,P5,   39.613300
AORTA_SOLID.415,P5,   147.36860
AORTA_SOLID.416,P5,   147.14630
AORTA_SOLID.417,P5,   157.65300
AORTA_SOLID.418,P5,   148.03200
AORTA_SOLID.419,P5,   147.51360
AORTA_SOLID.420,P5,   148.06762
AORTA_SOLID.421,P5,   147.79020
AORTA_SOLID.422,P5,   147.76150
AORTA_SOLID.423,P5,   146.10040
AORTA_SOLID.424,P5,   148.61882
```

```
AORTA_SOLID.425,P5,   150.54351
AORTA_SOLID.426,P5,   152.28160
AORTA_SOLID.427,P5,   154.23790
AORTA_SOLID.428,P5,   155.43670
AORTA_SOLID.429,P5,   156.49240
AORTA_SOLID.430,P5,   156.31022
AORTA_SOLID.431,P5,   162.42904
AORTA_SOLID.432,P5,   166.42650
AORTA_SOLID.469,P5,   147.50460
AORTA_SOLID.470,P5,   147.50460
AORTA_SOLID.471,P5,   155.77770
AORTA_SOLID.472,P5,   147.67970
AORTA_SOLID.473,P5,   147.46820
AORTA_SOLID.474,P5,   147.57521
AORTA_SOLID.475,P5,   147.74730
AORTA_SOLID.476,P5,   148.84610
AORTA_SOLID.477,P5,   146.10040
AORTA_SOLID.478,P5,   148.61882
AORTA_SOLID.479,P5,   150.68611
AORTA_SOLID.480,P5,   152.12730
AORTA_SOLID.481,P5,   153.50524
AORTA_SOLID.482,P5,   155.43670
AORTA_SOLID.483,P5,   156.72610
AORTA_SOLID.484,P5,   155.53920
AORTA_SOLID.485,P5,   164.33911
AORTA_SOLID.486,P5,   166.42650
AORTA_SOLID.523,P5,   150.60823
AORTA_SOLID.524,P5,   147.78170
AORTA_SOLID.525,P5,   158.47610
AORTA_SOLID.526,P5,   147.74640
AORTA_SOLID.527,P5,   146.66040
AORTA_SOLID.528,P5,   147.38710
AORTA_SOLID.529,P5,   147.68070
AORTA_SOLID.530,P5,   147.43190
AORTA_SOLID.531,P5,   147.24270
AORTA_SOLID.532,P5,   148.91320
```

```
AORTA_SOLID.533,P5,   150.68611
AORTA_SOLID.534,P5,   152.12730
AORTA_SOLID.535,P5,   154.08100
AORTA_SOLID.536,P5,   154.72900
AORTA_SOLID.537,P5,   156.72610
AORTA_SOLID.538,P5,   157.18070
AORTA_SOLID.539,P5,   164.56350
AORTA_SOLID.540,P5,   166.79680
AORTA_SOLID.577,P5,   149.70472
AORTA_SOLID.578,P5,   146.76112
AORTA_SOLID.579,P5,   158.47610
AORTA_SOLID.580,P5,   146.75050
AORTA_SOLID.581,P5,   145.97540
AORTA_SOLID.582,P5,   146.44110
AORTA_SOLID.583,P5,   146.61192
AORTA_SOLID.584,P5,   147.43190
AORTA_SOLID.585,P5,   146.51611
AORTA_SOLID.586,P5,   148.91320
AORTA_SOLID.587,P5,   149.82681
AORTA_SOLID.588,P5,   151.58830
AORTA_SOLID.589,P5,   152.56920
AORTA_SOLID.590,P5,   154.72900
AORTA_SOLID.591,P5,   156.20840
AORTA_SOLID.592,P5,   156.86694
AORTA_SOLID.593,P5,   164.37600
AORTA_SOLID.594,P5,   167.21594
AORTA_SOLID.631,P5,   148.71170
AORTA_SOLID.632,P5,   146.51643
AORTA_SOLID.633,P5,   148.71170
AORTA_SOLID.634,P5,   146.45490
AORTA_SOLID.635,P5,   144.72343
AORTA_SOLID.636,P5,   145.45080
AORTA_SOLID.637,P5,   146.60280
AORTA_SOLID.638,P5,   146.33860
AORTA_SOLID.639,P5,   146.30943
AORTA_SOLID.640,P5,   148.07710
```

```
AORTA_SOLID.641,P5,   149.99850
AORTA_SOLID.642,P5,   151.03300
AORTA_SOLID.643,P5,   152.43840
AORTA_SOLID.644,P5,   155.11530
AORTA_SOLID.645,P5,   155.42320
AORTA_SOLID.646,P5,   156.96550
AORTA_SOLID.647,P5,   164.37600
AORTA_SOLID.648,P5,   165.88050
AORTA_SOLID.685,P5,   144.30644
AORTA_SOLID.686,P5,   144.92600
AORTA_SOLID.687,P5,   144.30644
AORTA_SOLID.688,P5,   144.37303
AORTA_SOLID.689,P5,   143.60430
AORTA_SOLID.690,P5,   144.24980
AORTA_SOLID.691,P5,   144.51370
AORTA_SOLID.692,P5,   145.42810
AORTA_SOLID.693,P5,   145.94210
AORTA_SOLID.694,P5,   146.96081
AORTA_SOLID.695,P5,   149.38700
AORTA_SOLID.696,P5,   150.14854
AORTA_SOLID.697,P5,   152.30073
AORTA_SOLID.698,P5,   152.16183
AORTA_SOLID.699,P5,   156.37710
AORTA_SOLID.700,P5,   157.74440
AORTA_SOLID.701,P5,   162.51133
AORTA_SOLID.702,P5,   165.88050
AORTA_SOLID.739,P5,   139.56114
AORTA_SOLID.740,P5,   139.58290
```

Bibliography

[1] *Abaqus Users' Manual V6.8. SIMULIA.*

[2] *Methodology: STAR-CD Version 4.06. In CD-adapco: 2009.*

[3] *Star-CD version 4.10 Documentation; CD- adapco.*

[4] J. Moore y J. Meister A. Delfino, N. Stergiopulos. Residual strain effects on the stress field in a thick wall fnite element model of the human carotid bifurcation. *Journal of Biomechanics*, 30:777–786, 1997.

[5] Best and Taylor. *Taylor's Physiological Basis Of Medical Practice.* Hardcover, 1993.

[6] Ward C. Clinical significance of the bicuspid aortic valve. *Heart 2000*, 5:1:81, 1983.

[7] H. Y. H. Chen and T. W. H. Sheu. Finite-element simulation of incompressible uid ow in an elastic vessel. *Int. Journal for Numerical Methods in Fluids.*, 42:131–146, 2003.

[8] P. G. Ciarlet. *Mathematical elasticity, Volume 1: Three dimensional elasticity.* North-Holland., 1988.

[9] P. A. Dashner. Elastic shadow flow and its theoretical implication for inelastic solids. *In ternational Journal of solids and structures*, 2000.

[10] H. Demiray. On the elasticity of soft biological tissues. *Journal of Biomechanics*, 5:309–311, 1972.

[11] J. Donea and Huerta. *Finite element methods for flow problems.* Wiley., 2003.

[12] G. Dubini. *Appunti di biofluidodinamica*. Politecnico di Milano.

[13] Fung. *Biomechanics. Mechanical properties of living tissues.* Springer, 1993.

[14] J. F. Gerbeau and M. Vidrascu. A quasi-newtonian algorithm based on a reduced model for fluid-structure interaction problems in blood flow. In *Proceedings of the second MIT Conference on Computational Fluid and Solid Mechanics.*, 2003.

[15] J. F. Gerbeau and M. Vidrascu. A quasi-newtonian algorithm based on a reduced model for fluid-structure interaction problems in blood flow. In *Rapport de Recherche, INRIA, Paris.*, 2003.

[16] O. Gonzalez and A. M. Stuart. Introduction to continuum mechanics. In *Lecture notes. Standford University*, 1995.

[17] Harrison. *Principi di medicina interna*. McGraw-Hill Professional, 2004.

[18] J. D. Hart. *F uid structure interaction in the aortic heart valve.* PhD thesis, Technische Universiteit Eindhoven., 2002.

[19] Claudio Garcia Herrera. *Comportamiento mecanico de la aorta ascendente: caracterizacion experimental y simulacion numerica*. PhD thesis, Universidad Politecnica de Madrid, Escuela Tecnica Superior de Ingenieros de caminos, canales y puertos, 2008.

[20] G. Holzapfel. *Non linear solid mechanics.* Wiley., 2000.

[21] G. A. Holzapfel and T. C. Gasser. A new constitutive framework for arterial wall mechanics and a comparative study of material models. *Journal of Elasticity*, 61:1–48, 2000.

[22] Kenneth E. Jansen Charles A. Taylor Irene E. Vignon-Clementel, C. Alberto Figueroa. Outflow boundary conditions for three-dimensional finite element modeling of blood flow and pressure in arteries. *Comput. Methods Appl. Mech. Engrg.*, 195:3776–3796, 2006.

[23] Fasolli-Stella J. Donea and S. Giuliani. Lagrangian and eulerian finite element techniques for transient fluid-structure interaction

problems. In *Transactions of the 4th SMIRT Conference, San Francisco*, 1977.

[24] W. K. Liu J. R. Hughes and T. K. Zimmermann. Lagrangian-eulerian finite element formulation for incompressible viscous flow. *Coump. Methods Appl. Mech. Eng.*, 29:329–349, 1981.

[25] J. M. Goicolea y F. Gabaldon J. Rodriguez. A volumetric model for growth of arterial walls with arbitrary geometry and loads. *Journal of Biomechanics*, 40:961–971, 2007.

[26] Plappert T Pochettino A Bavaria JE Sutton MG. Keane MG, Wiegers SE. Bicuspid aortic valves are associated with aortic dilatation out of proportion to coexistent valvular lesions. *Circulation*, 102:III35–III39., 2000.

[27] Stanley E. Rittgers. Krishnan B. Chandran, Alit P. Yoganathan. *Biofluid Mechanics: The Human Circulation*. Hardcover.

[28] L. Lewin M. Souli, A.Ouahsine. Ale formulation for fluid-structure interaction problems. *Comput. Methods Appl. Mech. Engrg.*, 190:659–675, 2000.

[29] L. Malvern. *Introduction to the Mechanics of a Continuous.* Prentice-Hall., 1969.

[30] H. G. Matthies and J. Steindfor. Partitioned but strong coupled iteration schemes for non-linear fluid-structure interaction. *Computers and Structures.*, 80:1991–1999, 2002.

[31] H. G. Matthies and J. Steindfor. Partitioned strong coupling algorithms for fluid-structure interaction. *Computers and Structures.*, 81:805–812, 2003.

[32] M. S. Moayeri and G. R. Zendehboudi. Eects of elastic property of the wall on ow characteristic through arterial stenoses. *Journal of Biomechanics*, 36:525–535, 2003.

[33] M. Mooney. A theory of large elastic deformation. *Journal of Applied Physics*, 11:582–592., 1940.

[34] H. Morand and R. Ohayon. *Interaction fluides-structures.* Volume 23 of Reserches en Mathematiques Appliquees., 1992.

[35] West J Summers K Walker P Nagata M et al. Nataatmadja M, West M. Abnormal extracellular matrix protein transport associated with increased apoptosis of vascular smooth muscle cells in marfan syndrome and bicuspid aortic valve thoracic aortic aneurysm. *Circulation*, 108 suppl.1:II329–34, 2003.

[36] Marin M et al. Nistri S, Sorbo MD. Aortic root dilatation in young men with normally functioning bicuspid aortic valves. *Heart*, 82:19–22, 1999.

[37] R. W. Ogden. Large deformation isotropic elasticity on the correlation of theory and experiment for incompressible rubberlike solids. *Proc. R. Soc. Lond*, 362:565–584., 1972.

[38] R. W. Ogden. Non-linear elasticity with applications to material modelling. In *AMAS Lectures note 6, IPPT Warsaw.*, 2003.

[39] Kouchoukos NT Moon MR Sundt TM Okamoto RJ, Xu H. The influence of mechanical properties on wall stress and distensibility of the dilated ascending aorta. *J Thorac Cardiovasc Surg*, 126:842–50, 2003.

[40] K. Perktold. Computational model of arterial flow and mass transport. In *Lecture notes. CISM, Italy*, 2002.

[41] A. K. Pietal. Blood as a complex fluid, flow and suspensions. In *Lecture notes. IPPT, Poland.*, 2005.

[42] K. Pister y G. Goudreau R. Taylor. Thermomechanical analysis of viscoelastic solid. *International journal for numerical methods in engineering*, 2:45–59, 1970.

[43] G. Saccomandi y I. Sgura R. W. Ogden. Fitting hyperelastic models to experimental data. *Computational Mechanics*, 34:484–502, 2004.

[44] R. Rivlin. Large elastic deformations of isotropic materials. *Philos. Trans. Roy. Soc. London*, 241:368–397, 1940.

[45] Cook JW Fowler B Robicsek F, Thubrikar MJ. he congenital bicuspid aortic valve: how does it function? why does it fail? *Ann Thorac Surg*, 77:177–185, 2004.

[46] J. Rodriguez. *Modelos Numericos para mecanica cardiovascular de las paredes arteriales y sus procesos de adaptacion.* PhD thesis, Politecnica de Madrid, 2003.

[47] Segueria. Analysis and simulation of non-newtonian models in blood circulation. In *Lecture notes, Lausanne*, 2003.

[48] A. Spencer. Continuum theory of the mechanics of fibre-reinforced composites. *CISM*, 282:1–32, 1984.

[49] J. Suo. *Investigation of blood flow patterns and hemodynamics in the human ascending aorta and major trunks of right and left coronary arteries usind magnetic resonance imaging and computational fluid dynamics.* PhD thesis, Georgia Institute of Technology, 2005.

[50] R. Ogden y G. Holzapfel T. C. Gasser. Hyperelastic modelling of arterial layers with distributed collagen fibre orientations. *Journal of the Royal Society*, 3:15–35, 2006.

[51] L. R. Treloar. The mechanics of rubber elasticity. *J. Polymer Sci.: Polymer Symposium*, 48:107–123, 1974.

[52] C. Truesdell. *A first course in rational continuum mechanics: volume 1, general concepts.* Academic Press., 1977.

[53] C. Truesdell and W. Noll [1965]. *The non-linear Field Theories of Mechanics.* Springer-Verlag s. Zugge ed, 1965.